



HAL
open science

Biomass reactions on heterogeneous catalysts : computational studies on surface determination and reactivity

Qingyi Gu

► **To cite this version:**

Qingyi Gu. Biomass reactions on heterogeneous catalysts : computational studies on surface determination and reactivity. Theoretical and/or physical chemistry. Université de Lyon, 2019. English. NNT : 2019LYSEN011 . tel-03266620

HAL Id: tel-03266620

<https://theses.hal.science/tel-03266620>

Submitted on 22 Jun 2021

HAL is a multi-disciplinary open access archive for the deposit and dissemination of scientific research documents, whether they are published or not. The documents may come from teaching and research institutions in France or abroad, or from public or private research centers.

L'archive ouverte pluridisciplinaire **HAL**, est destinée au dépôt et à la diffusion de documents scientifiques de niveau recherche, publiés ou non, émanant des établissements d'enseignement et de recherche français ou étrangers, des laboratoires publics ou privés.



Numéro National de Thèse : 2019LYSEN011

THESE de DOCTORAT DE L'UNIVERSITE DE LYON
opérée par
l'Ecole Normale Supérieure de Lyon

Ecole Doctorale N° 206
Ecole doctorale de chimie (Chimie, Procédés, Environnement)

Spécialité de doctorat : Chimie Théorique
Discipline : Chimie

Soutenue publiquement le 21/06/2019, par :
Qingyi GU

**Biomass reactions on heterogeneous catalysts :
computational studies on surface determination
and reactivity**

Modélisation de l'état de surface et de la réactivité de catalyseurs
hétérogènes pour l'information de la biomasse

Devant le jury composé de :

Peijun HU	Professeur Queen's University, Belfast	Rapporteur
Haijun JIAO	Professeur LIKAT, University of Rostock	Rapporteur
Dominique COSTA	Directrice de Recherche CNRS Institut de Recherche de Chimie Paris	Examinatrice
Céline CHIZALLET	Ingénieure de Recherche IFP Energies Nouvelles	Examinatrice
Carine MICHEL	Chargée de Recherche CNRS Laboratoire de Chimie, ENS de Lyon	Directrice de thèse
Anthony BOCAHUT	Ingénieur de Recherche PM2D, Solvay	Membre Invité

Acknowledgement

I wish to express my sincere appreciation to those who have contributed to this thesis and supported me during my three-year PhD journey. This thesis cannot be done without the accompany and support from these cute people.

First, I am extremely grateful to my PhD supervisor Carine Michel, who taught me a lot and guided me during the one-year Master study and three-year PhD research. She always gave me useful suggestions and helped me to solve problems when I was stuck with my work. She is so kind and cares not only about her student's research but also their daily life, their mental health and their future career. As a foreign student in France, she would care about how was everything going from time to time and asked me to go around to release pressure if I seemed to be in a low mode. She also provided me a lot of help for my future carrier, such as some suggestions of taking part in some conferences according to my willing in choosing my future career, such as gave me some advice of being teaching assistant and gave me more chances to meet different people in our field.

I would like to express my sincere gratitude to my PhD committee members Prof. Peijun Hu, Prof. Haijun Jiao, Dr. Dominique Costa, Dr. Céline Chizallet and Dr. Anthony Bocahut for their contributions and witness of my professional development during my graduate education.

I would also like to thank Philippe for giving me the chance to study in ENS Lyon; Stephan for the useful discussion and technical help in dealing with the basic system and the electrochemistry; Jean-François for his beautiful LaPO_4 wood model and introduction to his work; David for his warmhearted help in the two Gold conferences; Romain for helping me in building their spectrum figure and the ZPE calculation in detail; Benjamin

for his technical help in scripts; Kamila, Chen-hui and Antton for their accompany as the same year PhD students; Enza, Ayad and Daniel for the accompany as my office roommates; Sarah, Paul, Pauline, Adrian, Akif and Ruben for their help both in my daily life and research; Tao and Christian for solving computer problems; Damien, Edwige and Marie-Francoise for the administrative affairs of the lab; and all the members in our group.

My sincere thanks also go to our partners, thanks Raphael for introducing me into the world of theoretical chemistry; Marc, Wenjuan and Yang for their work and discussion in the gold-copper project; Jean-marc and Maxime for their work and discussion in the LaPO_4 project; Stéphane and Jean-François Paul for their work and discussion in the CaHPO_4 project; Pascal for his useful discussion in the alcohol oxidation. Also, I would also like to acknowledge grants from the China Scholarship Council for the financial support for me to complete my PhD research.

我还要感谢我的阿公，阿婆，爸爸和妈妈，谢谢他们对我的关爱以及在我读博期间没有催我找对象没有给我压力让我以比较轻松的姿态度过了三年博士生活；谢谢在里昂一起吃饭生活学习的小伙伴们，张玲、文月、路欣楠、徐浩学姐，王涛师兄和嫂子，大卫、郑正、吴楠楠学长，京云，汪佩，蔡蔡，海秀，大小婷婷，露露，乔崇智，巩俊卿，贾云龙，绍莹等等可爱的小伙伴们，还有一直给我鼓励的李公仆，杨老师，钱老师，小韩，嬷嬷，皇上，阿哥，奶奶，周梅荒，小金瑶，潘敏xi 以及工五的大家，以及伴随了我很久的家鸽，老吴，灿灿，妮妮以及虽然没多久但是依然很爱的拢龙，还有很多这三年间遇到的各位小伙伴们，尽管身在天涯，但愿后会有期。

Merci pour tout.

Contents

Chapter 1	Introduction.....	9
Chapter 2	Methodology.....	15
2.1	Density functional theory in periodic conditions.....	15
2.1.1	GGA-PBE functional.....	16
2.1.2	The dDsC dispersion correction.....	17
2.1.3	Periodic system computation.....	18
2.2	Molecules in solution.....	20
2.2.1	Gibbs free energy of molecules in solution.....	20
2.2.2	Micro-solvation method with molecules in solution.....	22
2.2.3	Modeling adsorption and desorption processes.....	27
2.3	Modeling of basic environment.....	31
2.3.1	The modeling of basic environment.....	31
2.4	Ab-initio thermodynamics.....	36
Chapter 3	Alcohol oxidation on Au in neutral and basic environment.....	38
3.2	Unravelling the role of base and catalyst polarization in alcohol oxidation on Au and Pt in water.....	45
3.2.1	introduction.....	45
3.2.2	Computational details.....	46
3.2.3	Choice of the model for basic environment and catalytic interface.....	48
3.2.4	Comparison of ethanol oxidation on Pt and Au in neutral and basic environment.....	49
3.2.5	Discussion.....	56
Appendix 3.2	58
3.3	AuCu/CeO ₂ bimetallic catalysts for the selective oxidation of fatty alcohol (in	

collaborate with our experimental co-operator Marc Pera-Titus in Solvay China)	71
3.3.1 Introduction.....	71
3.3.2 Computational details	73
3.3.3 Experimental results.....	73
3.3.4 DFT Results	75
3.3.5 Conclusion.....	84
Appendix 3.3.....	85
Chapter 4 Modeling dehydration reactions on metal phosphate catalysts.....	90
4.2 Dehydration reaction of Lactic acid to acrylic acid on Calcium phosphates (in cooperation with Stéphane Loridant and Jean-Francois Paul).....	101
4.2.1 Introduction.....	101
4.2.2 Computational details	103
4.2.3 The construction of the surfaces	104
4.2.4 TPD study on NH ₃ and CO ₂ adsorption on the catalytic surface.....	110
4.2.5 IR spectrum study on NH ₃ adsorption on a dehydrated surface	114
4.2.6 IR spectrum study on NH ₃ adsorption on a dehydrated surface in water environment	116
4.2.7 Conclusion	120
Appendix 4.2.....	122
4.3 Dehydration reaction of 2,3-butanediol on Lanthanum phosphate (in cooperation with Jean Marc Millet in IRCELYON).....	129
4.3.1 Introduction.....	129
4.3.2 Computational details	130
4.3.3 Experimental results.....	131
4.3.3 Modelling details	134
4.3.4 IR spectrum comparison between experiments and simulation.....	141
4.3.6 Conclusion	147
Appendix 4.3.....	148
Chapter 5 Conclusion.....	151
Bibliography	155

Abstract

In the context of biomass valorization by heterogeneous catalysis, computational chemistry is key to provide guidance to establish the nature of the active sites in combination with experimental characterizations. Then, the reaction mechanism can be studied to determine the rate determining transition state and intermediate and further design *in silico* better catalysts. We implemented this approach in several reactions involving alcohols that are key in the shift from a petroleum chemical feedstock to a biomass-based feedstock. Firstly, we focused on liquid phase alcohol oxidation by oxygen, a reaction that generally requires an alkaline environment, which is detrimental to the atom economy of the process since it generates the carboxylate salt instead of the carboxylic acid. We proposed a model of metal/basic water interface that includes the adsorption of hydroxide anion. It charges the metallic surface and modifies its catalytic activity. This model was first validated comparing the predicted activity of Au and Pt in presence and in absence of a base, and then used oxidation of alcohol ethoxylates by bimetals. Then, we switched to gas phase dehydration of C3 and C4 alcohols using phosphate-based catalysts. The modeling of the surfaces was based on experimental characterizations. The molecular coverage of water on the surface in function of the pressure and temperature was established using *ab initio* thermodynamic. The simulations of infrared spectra of CO, NH₃ and C₂H₂ adsorption allowed us to identify the acido-basic sites which play an important role in the reaction mechanism investigation that followed.



Résumé

Dans le contexte de la valorisation de la biomasse par catalyse hétérogène, la chimie théorique est essentielle pour guider la détermination de la nature des sites actifs en combinaison avec des caractérisations expérimentales. Ensuite, le mécanisme de réaction peut être étudié pour déterminer l'état de transition et intermédiaire déterminant la vitesse et ensuite concevoir de meilleurs catalyseurs *in silico*. Nous avons mis en œuvre cette approche dans plusieurs réactions impliquant des alcools qui jouent un rôle clé dans le passage du pétrole à la biomasse comme source de matière première pour les produits chimiques de commodités ou spécialités. Tout d'abord, nous nous sommes concentrés sur l'oxydation des alcools en phase liquide par l'oxygène, une réaction qui nécessite généralement un environnement alcalin, ce qui nuit à l'économie d'atomes du processus car il génère le sel carboxylate au lieu de l'acide carboxylique. Nous avons proposé un modèle d'interface métal / eau basique incluant l'adsorption d'anion hydroxyde. Cet anion charge la surface métallique et modifie son activité catalytique. Ce modèle a tout d'abord été validé en comparant l'activité prédite de Au et de Pt en présence et en l'absence de base, puis a été utilisé pour étudier l'oxydation d'éthoxylates d'alcool par des bimétalliques. Ensuite, nous sommes passés à la déshydratation en phase gazeuse d'alcools en C3 et C4 en utilisant des catalyseurs à base de phosphate. La modélisation des surfaces s'est basée sur des caractérisations expérimentales. La couverture moléculaire de l'eau à la surface en fonction de la pression et de la température a été établie à l'aide de la thermodynamique *ab initio*. Les simulations de spectres infrarouges d'adsorption de CO, NH₃ et C₂H₂ nous ont permis d'identifier les sites acido-basiques qui jouent un rôle important dans l'investigation du mécanisme de réaction qui a suivi.



Abbreviation

HMF	5-(hydroxymethyl)furfural
DFT	Density Functional Theory
LDA	Local Density Approximation
GGA	Generalized Gradient Approximation
B3LYP	Becke-three-parameter-Lee-Yang-Parr
vdW	van der Waals force
PAW	Projector Augmented wave method
RRHO	rigid rotor harmonic oscillator
PB	Poisson-Boltzmann
PCM	polarized continuum model
AEO	alcohol ethoxylates
AECA	alcohol ether carboxylic acids
EG	ethylene glycol
tBuOOH	tert-butyl hydroperoxide
VASP	Vienna ab initio simulation package
PBE	Perdew–Burke–Ernzerhof
dDsC	density-dependent dispersion correction
NEB	nudged elastic band
QN	quasi-Newton
TDTS	TOF-determining transition state
TDI	TOF-determining intermediate
PVP	polyvinylpyrrolidone
TOF	turn over frequency
LNP	Lanthanide phosphates
MMP	mixed metal phosphates
MTiP-1	mesoporous titanium phosphates
DMA	dimethylacetamide
TEM	Transmission electron microscope
XRD	X-ray diffraction
XPS	X-ray photoelectron spectroscopy
NMR	Nuclear Magnetic Resonance spectroscopy
IR	infrared spectra
DMP	2,6-dimethylpyridine
LA	Lewis acid
BA	Bronsted acid

HA	hydroxyapatite
MD	molecular dynamic
AA	Acrylic Acid
LAA	Lactic Acid
23BDO	2,3-butanediol
MEK	methyl ethyl ketone
3B2OL	3-buten-2-ol
MPA	2-methylpropanal

Chapter 1 Introduction

Biomass

Rapid consumption of petroleum during the past few decades has led to a severe resource starvation for the whole humanity. Thus, the importance of using renewable resources gets more attention and gains general acceptance all over the world. The concept of green chemistry has been put forward in the mid-1990s, using renewable material feedstocks and energy sources as one of the most important principles¹. As a quite promising feedstock, biomass and its derivatives are more and more studied to ease the energy crisis and fundamentally resolve this problem.

Biomass is organic materials from plants and animals including wood and its processing wastes, agricultural crops and waste materials, food and food waste and the animal manure and human sewage, basically such renewable energy is from solar energy². The biomass feedstock mostly studied in industry is the waste of wood and agricultural crops such as sugarcane bagasse, which mainly consists about 50% cellulose, 25% hemicellulose and 25% lignin³. The following products from these feedstocks can be sorbitol, HMF, xylose and its derivatives as shown in **Figure 1.1**. Another important branch of the biomass feedstock is the oils and fats from plants and animals which contains mainly the triglycerides. As the most common stock of the industrial production of biodiesel, an environmental fuel which contains no sulfides and produces less pollution compared to the fossil fuels, triglycerides can produce biodiesel through transesterification with methanol and NaOH and KOH as the homogeneous catalysts⁴. Another useful chemical from triglycerides is glycerol, which can be transferred into

abundant products using many kinds of methods such as dehydration (to acrolein), oxidation (to corresponding aldehyde and acids) and so on as is shown **Figure 1.1**.

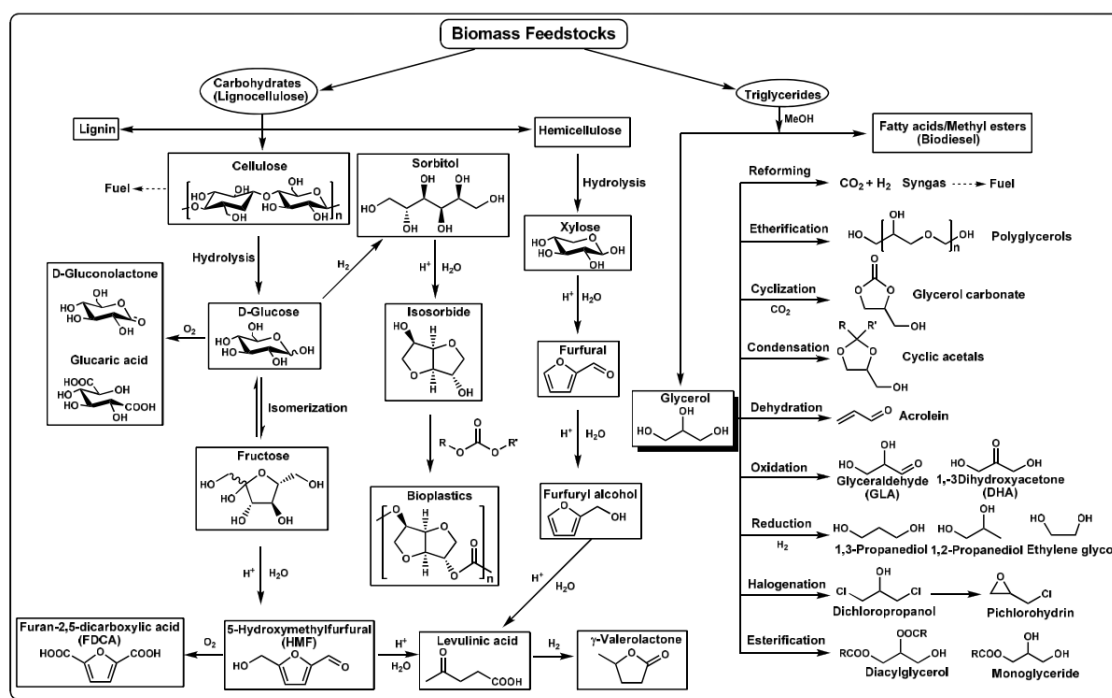


Figure 1.1 Representative valorization process for biomass conversion to chemicals and fuel reproduced from

Li's work⁵

The bio-based platform molecules, which are already functionalized compounds compared to the alkanes from fossil feedstocks as we mentioned in **Figure 1.1**, include sugars (glucose, xylose), polyols (sorbitol, xylitol, glycerol), furans (furfural, 5-hydroxymethylfurfural) and acids (succinic, levulinic, lactic acids), which has been put forward by the US Department of Energy (DOE)⁶ and revised by Bozell and Petersen⁷ according to the availability of commercial technologies for its production and their potential to be simultaneously transformed into fuels and chemicals in facilities called biorefineries⁸. The treatments of biomass feedstocks, such as bagasse, wheat straw and shavings, into its corresponding platform molecules are complicated, the procedural steps involved in the production of various industrially important products normally start from the following treatments such as fermentation and enzymatic hydrolysis (in producing ethanol, xylitol, Organic acids and some other value-added products like aroma and bio-

hydrogen), chemical catalysis and pyrolysis (in producing furans)⁹. In our study, we are mainly interested in the chemical using of the platform molecules, and our target is to seek a more environmental way to transfer them into more valued chemicals.

Heterogeneous catalysis in biomass reactions

Among all the principles of green chemistry, using catalytic reactions instead of using stoichiometric reactions is strongly recommended. Compared to stoichiometric reactions, using catalysts in chemical reactions not only accelerates the reactions but also decreases a lot the energy input during the process, what's more, the elimination of most of the possible toxic byproducts also embodies principles of green chemistry. For heterogenous catalysts, the property of easy to be recycled and separated from the products is also a bonus point. A typical example is the oxidation of primary alcohol using strong oxidant such as potassium dichromate ($K_2Cr_2O_7$) and chromium trioxide (CrO_3), of which the Cr^{6+} inside is highly carcinogenic and corrosive, along with the strong acid H_2SO_4 in water solution. But now, more and more heterogeneous catalysts, such as Pt¹⁰⁻¹⁴, Au^{13,15-26}, and many alloys, like AuPd^{16,27-33}, AuPt^{16,28,34-36}, AuCu³⁷⁻⁴⁰ and PtCu^{41,42} are found to be active in the alcohol oxidation to acid which can avoid the using of strong oxidant. The green way of oxidizing alcohol to its corresponding acid using green oxidant such as molecular oxygen and hydroperoxide and produces water as byproduct will be detailed introduced in Chapter 3.

The heterogeneous catalysts are generally consisted by the following components: (i) main catalysts, which play the role of the active species; (ii) support, at most time it provides high surface area and stabilizes the main catalyst; (iii) promotor, it improves some properties of the main catalysts such as the particle size, structure and electronic property to improve the activity. A complete chemical reaction on heterogeneous catalysts includes the following three steps: (i) the adsorption from the outside phase, either liquid or gas phase, to the catalytic surface; (ii) the reaction on the catalytic surface; (iii) desorption, which is the inverse process of adsorption.

The drawbacks of using heterogeneous catalysts in reaction mainly lies in the situation triggered from the “heterogeneous” condition and from the catalyst itself: (i) diffusion resistance, especially the adsorption and desorption process during the reaction, the diffusion becomes more severe in the pilot plant⁴³; (ii) the inactivity of the catalysts such as poisoning and leaching⁴⁴.

Modeling biomass related reactions catalyzed by heterogeneous catalysts

With the development of the computational resources and techniques, modeling heterogeneous reactions is becoming more and more important in the study of biomass-based reactions by understanding the mechanism and finally shorten the time for catalytic designing. Normally, catalytic modeling plays a role in the three stages of the development ladder: modeling surface properties obtained from characterization, understanding the reaction mechanism and predicting the reactivity of a larger range of other catalysts. The main goal of theoretical mechanism study is to unravel the relation between structure and the three key parameters in a reaction: activity, selectivity, and stability⁴⁵. The main strategy of modeling heterogeneous catalysis is shown in Figure 1.2.

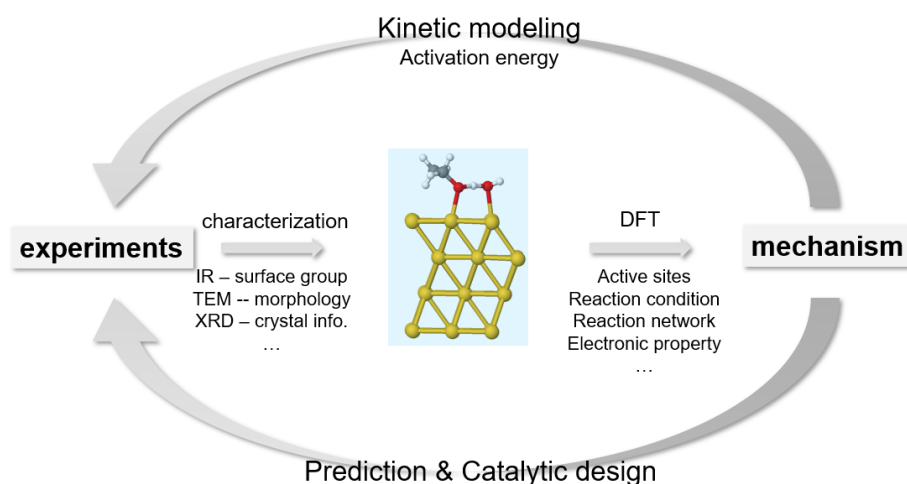


Figure 1.2 Modeling procedure in a heterogeneous catalysis reaction

To start the modeling of a reaction on surface, it is necessary to well build the surface

morphology before the reactivity study. Metals⁴⁶, metal oxides^{47,48} and metal phosphates⁴⁹⁻⁵¹ are normally used as main catalysts in biomass-based reactions. The surface structure of metallic catalysts is usually easy to be reproduced, if we only consider the metallic part for simplification, which differs from different Miller indexes and particle size¹⁵. The metal oxides and metal phosphates are more complicated, not only because of its complex structures as it can be amorphous or crystalline⁵², it can have different porous structures⁵³, but also comes from the changeability of the morphology which affected a lot due to the environment⁵⁴. From a thermodynamic point of view, the surface structure can be determined using the ab initio thermochemistry in the crystalline catalysts⁵⁵. But the modeling of an amorphous surface still remains a challenge. Here we mainly talk about the modeling of main catalysts and no support effect is considered for its complexity. But when the modeling of metallic catalysts including the support, the difficulty increases as we also need to consider the support effect into account. Although the support mainly plays the role of influencing the active phase dispersion and mass transfer phenomena, it also affects the reactivity of active centers and their coordination environments⁵⁶. Also, except the active carbon, most of the supports are metal oxides such as TiO_2 ^{27,29,32,35,39,57-59}, Al_2O_3 ^{58,60,61} and CeO_2 ^{17,34,62}, which come back to the difficulty we mentioned before.

In the previous petro-based industrial process, the production of the chemicals is performed in gas phase with high temperature and high pressure. Nevertheless, more and more reactions change the condition into the green solvent such as water for the sake of green chemistry. Then the difficulty raises up in modeling the reaction when dealing with the interface between the two or more phases, such as the adsorption and desorption process, especially in the solution reactions, where the interface between solution and solid catalyst is difficult to be well described, and lacking the benchmark from experimental results, the details will be discussed in detail in Chapter 2. Although many biomass-based reactions are solution reactions under mild reaction conditions, in some special reaction type such as dehydration⁴⁹⁻⁵¹, the using of higher temperature (higher

than 100°C) in gas phase is still unavoidable.

Modifying a catalyst and makes it become 100% selective for a given chemical reaction and some target products is a task for the modern industry⁶³. Modeling the reaction at the atomic scale is the most reliable and efficient way in understanding the reaction mechanism especially the selectivity issue. The selectivity issue is brought to the attention especially on metal salt catalysts, where the selectivity is very relevant to its acido-basic properties on the surface. Hence, the determination of the acido-basic sites becomes a priority from characterization and by the theoretical research^{64,65}.

In our study, we mainly focused on two parts: (i) the alcohol oxidation to corresponding acid catalyzed by metal catalysts (Chapter 3), where we modeled the basic environment and compared the different presentations on the ethanol oxidation catalyzed by Au and Pt to unravel the role of basic environment(Chapter 3.2), and the AEO oxidation to AECA catalyzed by Au, Cu and AuCu alloy to figure out the particularity of the bimetallic catalyst(Chapter 3.3); (ii) the determination of the metal phosphate catalysts for the dehydration reactions (Chapter 4), where we modeled the Calcium phosphates according the IR spectroscopy characterization for the following lactic acid (LA) dehydration reaction(Chapter 4.2), and the Lanthanide phosphates for the 2,3-butanediol (2,3-BDO) dehydration reaction, where the procedure of the determination of the surface structure was also detailedly described (Chapter 4.3).

Chapter 2 Methodology

2.1 Density functional theory in periodic conditions

Density Functional Theory (DFT) can root to the Thomas–Fermi model in 1927⁶⁶ which first put forward the using of electron density when presenting the wave functions. The foundation of the density functional theory was set by Hohenberg and Kohn in 1964 in which it was considered that the system consisting of electrons moved under the influence of an external potential⁶⁷. In 1965, the simplification of the n-electron system into the n one-electron Schrödinger-like equations was proposed by Kohn and Sham in 1965 and was used up till now⁶⁸. The main idea of the theory is to use the electron density as the fundamental variable rather than the complicated wave function, which decreases the variables from $4N$ (N is the number of the electrons, every electron includes 3 position variables and 1 spin variable) to 3 (3 position variables of the electron density). The equation of the energy of the system with the total electron density is written in eq 2.1.1:

$$E_{total}[\rho] = T_e[\rho] + E_{ne}[\rho] + E_{ee}[\rho] \quad \text{eq 2.1.1}$$

Born-Oppenheimer Approximation is considered here, where we suppose the nuclei are fixed as the electrons move much more rapidly than the nuclei. The first part of the equation T_e is the kinetic energy of the electrons, the second part E_{ne} is the external potential energy of the electrons, which is the potential energy of the electrons under the external potential field generated by nuclei, these two parts have been studied well and can be calculated accurately. The third part is the interaction between the electrons, which is the most complicated part to calculate properly. To figure out the value of this part, Hohenberg and Kohn separated the equation into the form of eq 2.1.2:

$$E_{ee}[\rho] = \frac{1}{2} \iint \frac{1}{r_{12}} \rho(r_1) \rho(r_2) d\vec{r}_1 d\vec{r}_2 + E_{XC}[\rho] \quad \text{eq 2.1.2}$$

The integral part of the equation is the interaction potential energy caused by Coulomb interaction of the electron 1 and electron 2, and we consider electron 1 and electron 2 are independent with each other. But in reality, electrons are impossible to be independent, so people introduced another kind of energy, E_{XC} , named the exchange and correlation energy, which represents the interaction between the electrons. It indeed has two parts in E_{XC} , the exchange energy of the electrons with the same spin caused by the Pauli repulsion, we also call the exchange Fermi-correlation. The correlation energy is caused by the electrostatic effects which prevent electrons to come too close to each other, we also call it Coulomb correlation. The main problem of DFT is to calculate the exchange-correlation energy correctly, to have more proper results that are close to the reality, different functionals are used to estimate the value of it.

2.1.1 GGA-PBE functional

At the very beginning, Local Density Approximation (LDA) is proposed⁶⁸. As electrons slowly changes in the space, although the whole system is heterogeneous, we can still consider it is locally homogeneous, the expression of the exchange-correlation energy under this approximation can be written in eq 2.1.3:

$$E_{XC}^{LDA}[\rho] = \int \rho(\vec{r}) \varepsilon_{XC}(\rho(\vec{r})) d\vec{r} \quad \text{eq 2.1.3}$$

In the equation, $\rho(\vec{r})$ represents the electron density, ε_{XC} is the exchange-correlation energy of per particle of a homogeneous electron gas of charge density ρ . The most successful approximation model used in LDA is the uniform electron gas model.

LDA works quite well in many cases when the system consists of a quite homogeneous electron density. However, the results become unsatisfactory when it comes across those systems with quite heterogeneous electron density, such as atoms and molecules, so to make the approximation more suitable for those systems, the gradient is introduced to represent the heterogeneous case, which it is called Generalized Gradient

Approximation (GGA)⁶⁹. The description of GGA is written in eq 2.1.4:

$$E_{XC}^{GGA}[\rho] = \int \rho(\vec{r}) \varepsilon_{XC}(\rho(\vec{r})) d\vec{r} + \int F_{XC}[\rho(\vec{r}), \nabla\rho(\vec{r})] d\vec{r} \quad \text{eq 2.1.4}$$

The first part of the equation is the local density approximation, which is well established in LDA, the gradient information is included in the second part of the equation. From Nørskov's study on the chemisorption of O, CO and NO on different surfaces compared to the experimental data, GGA shows a much better accuracy compared to LDA⁷⁰. There are several different GGA functionals here including the most famous and popular PBE⁶⁹, which has some improvements over PW91⁷¹ including an accurate description of the linear response of the uniform electron gas, correct behavior under uniform scaling, and a smoother potential⁶⁹.

Nowadays, many hybrid descriptions of functionals are more and more used especially in some small systems, such as Becke-three-parameter-Lee-Yang-Parr (B3LYP)⁷², the most popular method for treating exchange and correlation. In this method, a Hartree–Fock calculation is performed to derive the exact exchange energy, which is mixed with the DFT-based exchange energy⁷⁰. However, the inclusion of some Hartree–Fock exchange makes the computations quite time consuming. Thus, in periodic system, especially metal, where the Hartree–Fock exchange does not work well, the GGA functional is still the most popular functional when dealing with periodic systems specially in surface science. And as we mentioned before, GGA-PBE works already quite well in most of the surface chemistry, hence in our heterogeneous catalysis study, the GGA-PBE functional is also used to have a compromise in accuracy and time cost.

2.1.2 The dDsC dispersion correction

Most of the GGA functionals do not take the van der Waals (vdW) force into consideration, which can cause nonnegligible errors especially in some large and non-polar molecules. One method is introducing the vdW correction into the functional, such as optPBE⁷³ and revPBE⁷⁴. Another more popular way is adding a dispersion correction

term such as D2⁷⁵, D3⁷⁶ and the adopted correction dDsC⁷⁷ in the following computation. The relationship between correction energy by dispersion energy and the DFT energy (without correction) is written in eq 2.1.5:

$$E_{\text{GGA-dispersion}} = E_{\text{GGA}} + E_{\text{dispersion}} \quad \text{eq 2.1.5}$$

In the equation, $E_{\text{GGA-dispersion}}$ is the total energy after correction, E_{GGA} is the energy calculated without dispersion, $E_{\text{dispersion}}$ represents the dispersion energy.

The D2 correction is fast but it does not take the environment into account when calculating the dispersion which limits the accuracy of the method. The D3 correction considers the environment but it cost a bit more than the D2 correction. Then we come to the dDsC correction which is based on the D2 dispersion, while it is able to take into account variations in the vdW contributions of atoms due to their local chemical environment.

A detailed comparison of different functionals of molecular adsorption on Pt(111) surface has shown that PBE-dDsC provide a good match with experiments, such as in the adsorption of benzene on Pt, the signed percentage deviation is only +2% compared to the large error of -35% if not including dispersion correction⁷⁸. Considering the excellent description of Pt by dDsC dispersion, in our following computation when come across the Pt system, dDsC is used. The dDsC dispersion is also used on Au in the long chain alkanethiol adsorption⁷⁹, which reproduces well the molecular structure and interaction between the Au atoms compared to the STM results⁸⁰.

2.1.3 Periodic system computation

To expand the wave function in DFT into algebraic equations suitable for efficient implementation on a computer, suitable basis sets are necessary to be introduced to solve them. In VASP, a plane wave basis set based on the Bloch's Theorem is used in the periodic system as shown in eq 2.1.6:

$$\psi_i(r) = \sum_G c_{i,k+G} e^{i(k+G).r} \quad \text{eq 2.1.6}$$

Where ψ is the wave function, c is a coefficient, r is the distance between the electron and the nuclei, G is the reciprocal lattice vector, k is a symmetric label in the first Brillouin zone.

To describe the electron-ion interaction, the Projector Augmented wave method (PAW)⁸¹ is used. It is an efficient method which extends and combines the traditions of augmented wave methods and the pseudopotential approach. PAW method uses the concept of the pseudopotential to simplify the calculation. The whole electronic region is divided into two parts using r as the boundary, (i) the atomic region, in which the kinetic energy of the electrons is quite large and results in rapid oscillations of the wave function; (ii) the bond region with valence electrons, in which the kinetic energy of the electrons is small so the wave function is smooth. And because of the main bonding part with other atoms is the bond region, so the wave function of the atomic part is not so important, as a result, we consider them together with the nuclei as rigid non-polarizable ion core so that we can deal with it with a quite smooth wavefunction. The 'frozen' atomic part is defined by the cut off radius, and outside is the bonding region.

2.2 Molecules in solution

2.2.1 Gibbs free energy of molecules in solution

Gibbs free energy of one molecule in solution:

$$\begin{aligned}
 G_{\text{aq}} &= H_{\text{aq}} - TS_{\text{aq}} \\
 &= U_{\text{aq}} + (PV)_{\text{aq}} - TS_{\text{aq}} \\
 &= U_{\text{aq}} + k_{\text{B}}T - TS_{\text{aq}} \\
 &\approx (E_{\text{ele}})_{\text{aq}} + \text{ZPE} - TS_{\text{aq}}
 \end{aligned}
 \tag{eq 2.2.1}$$

where:

H_{aq} is the enthalpy in solution;

S_{aq} is the entropy in solution;

ZPE is the zero-point energy;

U_{aq} is the internal energy in solution;

V the volume, P is the pressure, k_{B} is the Boltzmann constant, T is the temperature;

E_{ele} is the electronic energy.

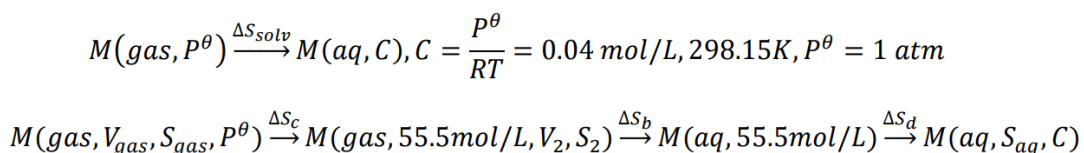
The entropy of molecules in gas phase comes from four contributions: translational entropy, rotational entropy, vibrational entropy and electronic entropy. As the molecule or system always stays in the ground state and has little possibility to jump to the excited state, so the electronic entropy can be safely neglected. The contributions from translation, rotation and vibration can be determined by corresponding partition functions under the rigid rotor, harmonic oscillator (RRHO) approximation, where the molecule are treated as essentially rigid, so that its internal motions include only vibrations of small amplitude, then the energy contributions-both kinetic and potential-of its translational, rotational, and vibrational motions can be approximated to be as uncoupled from each other^{82,83}:

$$S_t = R \left(\ln(q_t e) + \frac{3}{2} \right) \tag{eq 2.2.2}$$

$$S_r = R(\ln q_r + 1) \tag{eq 2.2.3}$$

$$S_v = R \sum_K \left(\ln(q_v) + T \left(\frac{\partial(\ln q)}{\partial T} \right)_v \right) \quad \text{eq 2.2.4}$$

Where S_t , S_r and S_v are translational, rotational and vibrational entropies respectively, q_t , q_r and q_v are translational, rotational and vibrational partition functions respectively, R is the gas constant, T is the temperature. The entropies in gas phase can be easily obtained from literature or calculation. Although the entropy in gas phase are easily obtained, it is difficult for the entropy in solution, because the decrease of rotational and translational entropy is difficult to quantify accurately. Here we took the entropy value in solution introduced by Wertz⁸⁴. Wertz concluded the transformation of molecules in gas phase to solution is shown in **Scheme 2.1**⁸⁵:



Scheme 2.1 Molecular transformation from gas phase to aqueous phase

Where M represents the molecule, P^θ represents standard pressure, R is gas constant, T is temperature, C is the concentration of molecule under standard pressure, V is volume, S is entropy, ΔS_{solv} represents the total solvation energy from gas phase to aqueous phase, ΔS_c represents the entropy change of the compression process, ΔS_b represents the entropy change of the transformation process, ΔS_d represents the entropy change of dilution process.

According to **Scheme 2.1**, Wertz obtained the following relation between entropy in gas phase and solution is proposed to be:

$$\Delta S_{\text{solv}} = -0.46(S_{\text{gas}} - 14.3)$$

$$S_{\text{aq}} = S_{\text{sol}} + S_{\text{gas}} = 0.54 \times S_{\text{gas}} + 2.86 \times 10^{-4} (\text{eV} \cdot \text{K}^{-1}) \quad \text{eq 2.2.5}$$

So, the free energy in solution can be written as:

$$G_{\text{aq}} = (E_{\text{ele}})_{\text{aq}} - T \times (0.54 \times S_{\text{gas}} + 2.86 \times 10^{-4} (\text{eV} \cdot \text{K}^{-1})) + \text{ZPE} \quad \text{eq 2.2.6}$$

The term $2.86 \times 10^{-4} (\text{eV} \cdot \text{K}^{-1}) \times T$ is $\Delta S_c \times T$, comes from the energy loss of first step where the molecule is treated as an ideal gas and compressed from 1 atm to 55.5 mol/L.

Here ZPE as we mentioned before is the zero-point energy, $E+ZPE$ is called the ground state energy of the system, which is the expectation value of the system energy at absolute zero. The zero-point energy can be represented as the energy of a harmonic oscillator at ground state:

$$\text{ZPE} = \frac{1}{2} \hbar \sum \omega \quad \text{eq 2.2.7}$$

Where \hbar is the plank constant, ω is the frequency. For linear molecules, there are in total $3N-5$ normal modes, and for non-linear molecules the numbers of normal modes are in total $3N-6$, where N represents the numbers of atoms in the molecule. Steinmann et al. have proposed to limit the evaluation of Z_{vib} to large enough wavenumbers (using a cut-off of 50 cm^{-1})⁸⁶.

However, the entropy in eq 2.2.7 cannot be taken as the entropy of a water molecule in liquid water. As water itself not only works as a solute but also a solvent, and equation eq 2.2.8 provides the entropy of a solute solubilized in water, not the one of the solvents. So in the following calculation, we took experimental data $69.95 \text{ J}/(\text{mol} \cdot \text{K})$ ⁸⁷ as the entropy of liquid water. Thus, the free energy of H_2O can be calculated as

$$G_{\text{aq}}(\text{H}_2\text{O}) = (E_{\text{cle}})_{\text{aq}} - T \times (69.95 \text{ J}/(\text{mol} \cdot \text{K})) + \text{ZPE} \quad \text{eq 2.2.8}$$

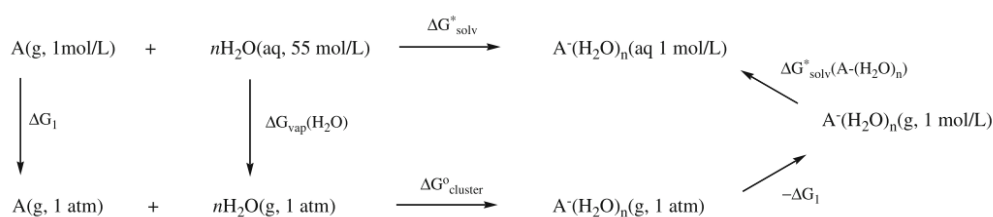
2.2.2 Micro-solvation method with molecules in solution

In most of previous studies in alcohol oxidation, little attention was paid to obtain a proper adsorption and desorption energy at the liquid/solid interface. Currently, in the most advanced studies, both the molecules in solution and adsorbates on surface are calculated using an implicit solvent model^{21,88,89}. However, the implicit solvent model can only extract the long-distance interaction by solution well, it neglects the short distance interaction especially when hydrogen bond can be generated between the solute and the solvent, which indicates the importance of using explicit solvent method, i.e. the

micro-solvation method

Micro-solvation method is widely used in the pKa calculation^{90,91}. Different models of pKa calculation, including the direct method ($\text{HA} + (n+1)\text{H}_2\text{O} \rightarrow \text{H}_3\text{O}^+ + \text{A}^-(\text{H}_2\text{O})_n$), the proton exchange method ($\text{HA} + \text{Ref} \rightarrow \text{HRef} + \text{A}^-$), the hybrid cluster–continuum ($\text{HA} + \text{OH}^-(\text{H}_2\text{O})_m \rightarrow \text{A}^-(\text{H}_2\text{O})_n + (m+1-n)\text{H}_2\text{O}$) and implicit–explicit model ($\text{HA} + n\text{H}_2\text{O} \rightarrow \text{A}^-(\text{H}_2\text{O})_n + \text{H}^+$), have been tested by Ho on 55 neutral organic and inorganic acids using different solvent models. In Ho’s research, the direct method is largely dependent on the solvent models while the methods including the hybrid cluster–continuum can potentially give reasonably accurate values⁹⁰.

The micro-solvation method is also necessary in obtaining proper solvation free energy^{92–95}. It plays a more critical role especially in the ionic species which has been revealed by Riveros⁹⁶, where the average error of solvation free energy is only 2.9 kcal/mol while up to 8.7 kcal/mol when only using the PCM model. However, the choosing of the number of water molecules around solutes is still in debate. Normally, the number of water molecules to include in the ion cluster is determined using “variational principle” where the lowest value of solvation free energy (ΔG^*_{solv}) occurs when using the cycle in **Scheme 2.2** **Scheme 2.1** ($\Delta G^*_{\text{sol}} = \Delta G^{\circ}_{\text{cluster}} + \Delta G^*_{\text{solv}}(\text{A}^-(\text{H}_2\text{O})_n) + \Delta G^{\circ}_{\text{vap}}(\text{H}_2\text{O})$). And the water molecules are added to positions where they can directly make hydrogen bonds with the atom bearing the charge in the anion^{90,96}.



Scheme 2.2 Thermodynamic cycle for calculation of cluster–continuum solvation free energy, reproduced

from Ho’s paper⁹⁰

To better describe the molecules in solution and obtain a more reasonable adsorption and desorption energy, molecules in solution are treated with a micro-solvation approach

combined with an implicit solvent model in our study. Molecules that are involved in the adsorption and desorption processes in ethanol oxidation are $\text{CH}_3\text{CH}_2\text{OH}$, CH_3COO^- , CH_3COOH and OH^- . Unlike the vibrational principle we mentioned before, considering the molecules in our study have been already studied a lot by other researchers, so the choice of the number of water molecules explicitly included is confirmed mainly through experimental data or other computational structure. For $\text{CH}_3\text{CH}_2\text{OH}$, Thapa⁹¹ computed the pKa and obtained the value with an error of -0.06 compared to experimental data; for CH_3COO^- and CH_3COOH , Fedotova⁹⁷ studied the hydration of the acetic acid and acetate ion in water using 1D-RISM theory, and an average numbers of water around the $-\text{COOH}$ and $-\text{COO}^-$ are 2.5 and 6 respectively; for OH^- , Shang²¹ computed the solvation energy of OH^- in water and obtained a proper value of -4.53 eV (the reported experimental value is -4.6eV) when using 4 water cluster around OH^- , we took the number of the water here as it is considered the complete first solvation shell for OH^- ⁹⁸. According to the study before, we chose the proper numbers of water when doing the micro-solvation of the molecules in solution. According to the number and position of waters around the molecules, similar micro-solvation treatments are done in the AEO (alcohol ethoxylates) oxidation into AECA (Alcohol ether carboxylic acids) which is illustrated in Chapter 3.3, [Figure A 3.3.1](#). In the methodology part, only molecules related to ethanol oxidation are mentioned here.

To mimic the water solution properly, we choose the configuration with waters around following two standards: the first is to construct as many hydrogen bonds as possible between water and the solute molecule, so that we can describe the solvation effect of molecule close to the reality at maximum extend, the second is to avoid water-water hydrogen bond, since water-water hydrogen bond will lead to an over-stabilization for the whole system, while we only focused on the stabilization caused by water solution to molecules. Taking all the above into account, we obtained the micro-solvated structures shown in [Figure 2.1](#)[Figure 2.1](#).

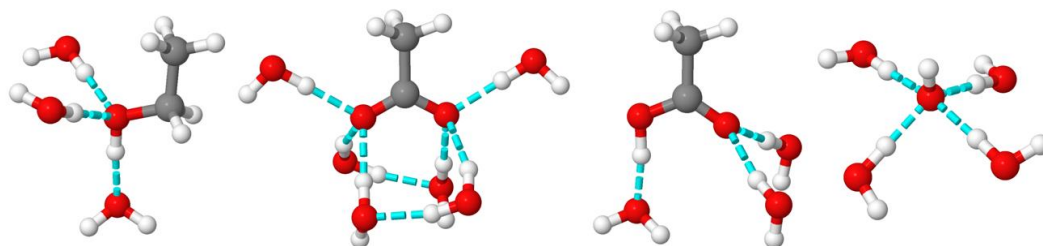


Figure 2.1 Structures of molecules described by micro-solvation method, with blue lines as H bonds

To validate the correctness of the micro-solvation method in our modelling, the free energy of the reaction



is calculated and compared to the experimental data ($\Delta G = -0.64$ eV at room temperature) derived from the pKa of CH_3COOH (pKa1 = 4.76) and H_2O (pKa2 = 15.74).

The reaction energy of equation eq 2.2.9 using different treatments are shown in Table 2.1.

Table 2.1 Effect of micro-solvation on CH_3COOH neutralization reaction

$\Delta G/\text{eV}$	$\text{CH}_3\text{COOH} + \text{OH}^- \rightarrow \text{CH}_3\text{COO}^- + \text{H}_2\text{O}$
With micro-solvation	-0.45
Without micro-solvation	-1.02
Using entropy obtained from eq 2.2.5	-0.95
Experimental data	-0.64

The standard state of liquid water is 55.5mol/L in our calculation. If reaction eq 2.2.9 is described only by implicit solvation model, the computed reaction Gibbs free energy is -1.02 eV, while when we take both the implicit and explicit solvation effect into account, the computational reaction free energy is -0.45eV, which shows a better consistency with the experimental data -0.64eV compared to the non-micro-solvation case. Also, as we mentioned before, an experimental entropy of 69.95 J/(mol•K) of H_2O is used in the equation, while if we directly take equation eq 2.2.5 as the entropy of water in solution, it gives a Gibbs free energy of -0.95 eV, the big difference between the two

treatments of the entropy of water lies in the fact that the water is not a solute but a solvent, so it is more reasonable to take the entropy of liquid water.

Another benchmark, the solvation free energy is also computed both with and without micro-solvation method. The similar trend is obtained with the pKa calculation, that the results with micro-solvation shows a better trend. So, in the following calculation, the micro-solvation models above are also used to obtain a proper adsorption and desorption energy.

Table 2.2 Effect of micro-solvation on solvation energy

$\Delta G_{\text{sol}}/\text{eV}$	OH ⁻	CH ₃ COO ⁻
With micro-solvation	-3.26	-2.56
Without micro-solvation	-2.56	-2.14
Experimental data	-4.48 ⁹⁹	-3.04 ¹⁰⁰

Although we obtained a proper reaction energy of the neutralization reaction of acetic acid, the proper treatment of ZPE still remains some doubts here. As we said before, the water here is not only the reactant but also the solution, shall we take the ZPE of the single water or is an average ZPE from the water cluster more convenient? A test of the free energy of water when using different ZPE values from water cluster is shown in **Table 2.3**.

Table 2.3 Free energy of water of different water clusters

Water cluster	E per water/eV	TS _{aq_exp} /eV	ZPE per water/eV	G per water/eV
H ₂ O	-14.57		0.58	-14.21
(H ₂ O) ₄	-14.75	0.22	0.64	-14.33
(H ₂ O) ₆	-14.76		0.64	-14.34
(H ₂ O) ₈	-14.81		0.66	-14.37

As is shown in **Table 2.3**, the main difference between the free energy of different water clusters lies in the electronic energy, the ZPE value does not vary lot. But the difference becomes larger when more additional water molecules are produced in the

reaction. It is found in the pKa calculation using cluster-continuum model⁹⁰, the free energy of water is dealt with still as a single water in the standard state of 55.5 mol/L, which represents in our case is using the experimental entropy considering the main energy loss during the compression is the entropy loss. So, according to their treatment of water molecules, we also use the ZPE and the energy of a single water, but the experimental entropy of liquid water is used when computing the free energy.

2.2.3 Modeling adsorption and desorption processes

Molecular adsorption on solid surface in gas phase has been investigated maturely and tremendously no matter in metallic catalysts⁷⁸ or other catalysts such as metal oxides¹⁰¹, metal phosphates¹⁰² and so on, where the adsorption energy comes from the difference between an adsorbate system and the energy of a bare surface and the molecule in gas phase. The adsorption energy can also be obtained through TPD using the Temkin model¹⁰³, which can be a good benchmark of the calculated adsorption energy.

However, it turns into a challenge when the adsorption occurs in solution. In the biomass-based reactions, aqueous reactions take up a large part. To deal with the solvent effect, there are in total two main treatments: (i) Only considering the implicit solvent, which is the most used method in dealing with the adsorption process as we mentioned before. (ii) Treating the adsorbates on surface in aqueous environment in the molecular dynamic level followed by further optimization with DFT^{104,105}. (iii) Building ice-like explicit water molecules¹⁰⁶.

Method (i) did not take the direct interaction between solvents and molecules into consideration, especially on the part that bonded with the surface before and after the adsorption, where the solvents around the part in solution while go away after adsorbed on the surface. Method (ii) and (iii) describes well the molecules (the gas feedstock in the reaction such as O₂, CO and so on) from gas phase to aqueous phase, while for the reactants which exist always in liquid state, it is not a proper description for the solute adsorption process.

In our study, molecules in solution were treated with micro-solvation combined with a PCM as we discussed above. This is key to describe oxygenated anionic species in water that create strong H-bond with water. But once those molecules are adsorbed on a metallic surface, the charge is transferred to the metal and diluted. In addition, the oxygen atoms are much less available to create efficient H-bonds with water. Thus, those species lose most of their solvation shell upon adsorption as it is strongly disrupted by the interaction of the functional groups with the surface and is mainly suppressed by the interaction between the functional groups of the reactants or products and the metal surface. In addition, it was shown in the past that the main effect of water in alcohol oxidation in water does not lie in the possible H-bonding with a chemisorbed water molecule that would micro-solvate the adsorbate. The main effect is the possibility to help the O₂ activation through the generation of surface hydroxyl OH*^{107,108}.

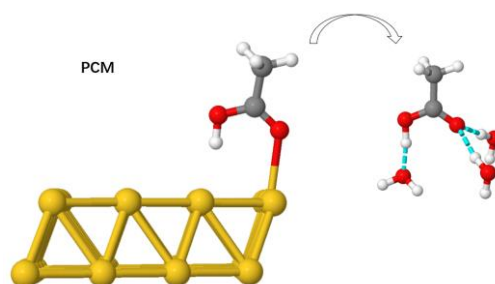
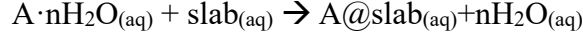


Figure 2.2 Desorption of acetic acid

As an example, **Figure 2.2** shows the acetic acid desorption from Au surface into water solution. The right part of the figure shows acetic acid in water solution and the left part is the adsorbed acetic acid. Both of them are computed in PCM. The main difference in the exposure to the solvent before and after adsorption lies in the oxygen groups, while the environment of other parts of the molecules remains almost unchanged. Thus, for a good description of adsorption at the metal/water interface, it is appropriate not to take into account the micro-solvation of those oxygen atoms on the surface while it is included in bulk solution. According to the previous description of adsorption and desorption, the adsorption Gibbs free energy can be calculated by



$$\Delta G_{ads} = G_{aq}(A@slab) + nG_{aq}(H_2O) - G_{aq}(A \cdot nH_2O) - nG_{aq}(slab) \quad \text{eq 2.2.10}$$

The Gibbs free energies involving the slab are given by:

$$G_{aq}(slab) \approx E_{aq}(slab) = E_{PCM}(slab) \quad \text{eq 2.2.11}$$

$$\begin{aligned} G_{aq}(A@slab) &\approx E_{aq}(A@slab) + ZPE(A) + TS_{aq(vib)}(A) \\ &= E_{PCM}(A@slab) + ZPE(A) + TS_{aq(vib)}(A) \end{aligned} \quad \text{eq 2.2.12}$$

Considering the configuration of slab does not change much before and after the adsorption, the main difference of ZPE and entropy lies in the molecules becoming adsorbates. Thus, only the ZPE and entropy of the adsorbates on the surface are computed, that is to say the slab is frozen in the frequency calculation. It is worth noting that the entropy term of adsorbates can be directly written as the vibrational entropy here considering the total loosing of translational and rotational entropy term on the surface. The vibrational entropy term in gas phase resulting from the vibrational partition function is:

$$S_{gas(vib)} = \sum_K \left(\frac{\Theta_{v,K}/T}{e^{\Theta_{v,K}/T} - 1} - \ln(1 - e^{-\Theta_{v,K}/T}) \right) \quad \text{Eq 2.2.13}$$

Where $\Theta_{v,K} = hv_K/k_B$, with k_B as the Boltzmann constant, v_K is the frequency of the vibration mode K, h is the plank constant. To obtain the vibrational entropy in solution, a correction of vibrational entropy from gas to solution is necessary. The entropy correction for molecules in solution can be expressed as:

$$S_{aq(vib)} \approx 0.54 \times S_{gas(vib)} \quad \text{Eq 2.2.14}$$

The description of the entropy of adsorbates in solution is based on the entropy of molecules in solution where almost half of the entropy is lost. It is worth noting that the entropy loss of the compression (the term of $2.86 \times 10^{-4} \text{ (eV} \cdot \text{K}^{-1})$) as we mentioned before) has not been considered here, there are in total two consideration of such measure: (1)

Normally the vibrational entropy is much smaller than the translational entropy and rotational entropy, thus during compression, the decrease of the vibrational entropy should also be the smallest; (2) Taking the property of compression process into consideration, it mainly reflects in the decrease of volume which also affects the vibration least.

2.3 Modeling of basic environment

2.3.1 The modeling of basic environment

The modelling of the base effect lies in two aspects: the coverage of OH species and the charge from the OH⁻. In the previous studies, many researchers modelled the pH by changing the coverage of OH on the surface^{109–111}. Such modelling of basic environment is reasonable but they neglect the effect of charge from OH⁻ in basic solution. Later, the charge effect is taken into consideration by Liu et al., they consider OH⁻ adsorbed on the surface and charged the nanoparticles. It is found that the charged surface is able to activate O₂ to OH and finally withdraws charge on the surface and becomes OH⁻²¹. The establish of the charged nanoparticle to mimic the basic environment by Liu implies the rationality of the modelling of basic environment by introducing electrons into the surface. A charged surface modelling in demonstrating the key role of anionic doping in the H₂ production from formic acid was also built by Wang⁸⁵ on Pd(111) surface, the anionic doping here plays the role of charging the surface and generates an electric field which strongly facilitates the direct formate/carboxyl dehydrogenation. Thus, in our study, we mainly focused on the importance of the charge from OH⁻.

To neutralize the negative charge from OH⁻, the counter charge is described through the Debye-Hückel theory using the linearized Poisson-Boltzmann (PB) equation in a polarized continuum model (PCM). A 5-layer mirror symmetric model was used to model the metal surface to obtain a slab showing two identical surfaces, without net dipole, which is necessary when electrons are introducing into the surface. To confirm the validity of this approach, we carefully checked the properties of the basic electrolyte NaOH and KOH adsorbed on the 4×4 Au(111) surface. In both cases, the anion is strongly adsorbed (Au-O bond of 2.36 Å) while the cation is farther at more than 3 Å from the metallic surface (Figure 2.3). The overall stability of this system is not very sensitive to its position in the plane parallel to the surface (as shown in Table 2.4, variation of 0.03 eV at most). All in all, this confirms that the cation is not chemisorbed, its position

is ill defined and should be averaged and thus a linear Poisson Boltzmann distribution of the counter charge is a reasonable model of the cation. This is consistent with our previous results⁸⁵.

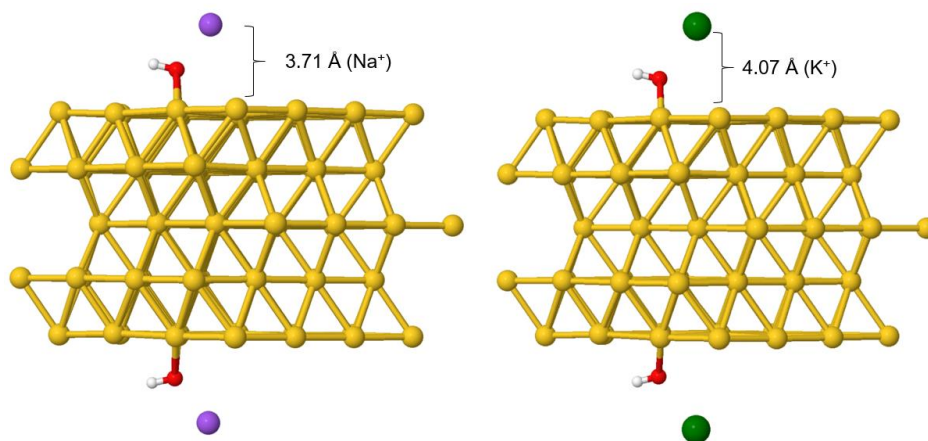


Figure 2.3 Structures of NaOH (left) and KOH (right) adsorbed on the surface

Table 2.4 Adsorption energy in function of the distance of Na⁺ and K⁺ to the surface plane

$d(X^+)/\text{\AA}$	$E_{\text{ads}}(\text{NaOH})/\text{eV}$	$E_{\text{ads}}(\text{KOH})/\text{eV}$
Most stable distance	-1.18	-1.23
5	-1.16	-1.21
5.5	-1.16	-1.21
6	-1.15	-1.20

Where $d(X^+)$ represents the distance of the ions to the surface.

To simplify the basic environment at to the great extent, it is finally modeled by a charged surface and a PB counter charge distribution. To verify the rationality of the model, a comparison of the counter charge density of different systems, the charged surface (slab_e), the surface with adsorbed OH⁻ (slab_OH_e), the surface with adsorbed NaOH (slab_NaOH) and the surface with adsorbed KOH (slab_KOH) are presented in **Figure 2.4**.

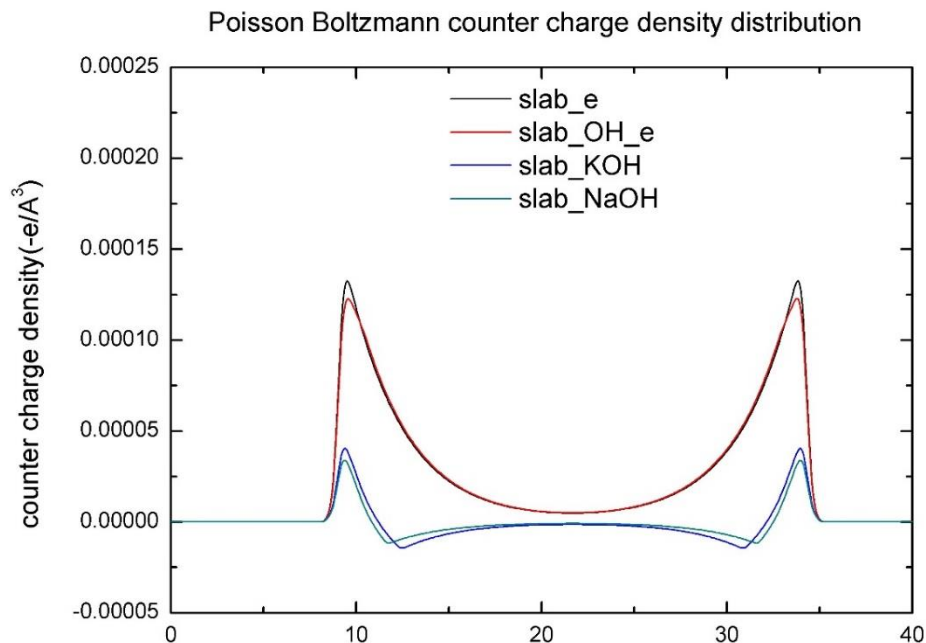
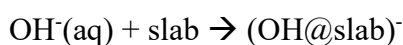


Figure 2.4 Counter charge density distribution comparison among charge base surface (black), surface with OH⁻ adsorbate (red), surface with KOH adsorbate (blue) and surface with adsorbate (green)

As shown in **Figure 2.4**, little difference is shown in the counter charge density between slab_KOH and slab_NaOH, also between slab_e and the surface with slab_OH_e. The fewer smaller counter charge density of slab_KOH and slab_NaOH compared to slab_e and slab_OH_e mainly come from the positive charge of K⁺ and Na⁺. The integration of the counter charge of slab_e and slab_OH_e in the symmetric cell is 2 positive charge while it should be 0 charge in slab_KOH and slab_NaOH.

The adsorption of OH⁻ can be described as



The adsorption free energy of OH⁻ in water solution at room temperature on a 4×4 Au(111) surface is 0.01 eV (-0.98 eV without micro-solvation), and -0.89 eV (-1.88 eV without micro-solvation) on a 4×4 Pt(111) surface. The adsorption of OH⁻ in solution into the surface is a key step to introduce an electron into the surface, it occurs with no difficulty on Pt surface while an adsorption cost of +0.01 eV makes it not so easy on Au. As we mentioned before, the micro-solvation method can help us to obtain a proper

thermodynamic benchmark for the overall reaction, to keep consistency, during the adsorption and desorption process, reactants or products with surrounded waters are also needed to be used. However, it is impossible to find an accurate benchmark for the adsorption energy in solution. The large difference between the adsorption energy with and without micro-solvation, mainly comes from the stabilization by the waters around the molecules in solution. And consider there is no micro-solvation on the surface to have shorter computational time and less complexity, it is rational to believe there exists an over stabilization of molecules in solution compared with the adsorbates.

The adsorption is found to be more favorable when decreasing the density of the charge on the surface, which is represented by adsorbing the OH^- into a larger slab size here. The relationship between adsorption energy of OH^- on Au surface is shown in **Figure 2.5**.

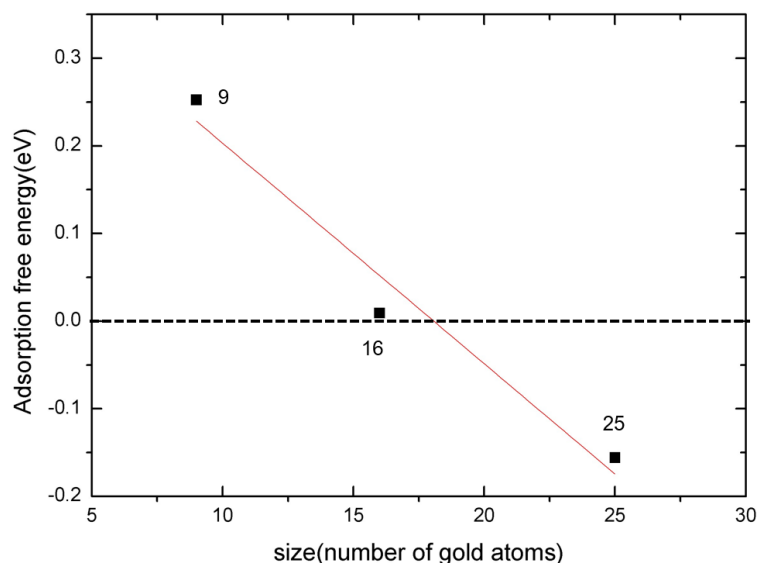


Figure 2.5 Adsorption free energy of OH^- on different sizes of Au(111) surfaces

A clear linear trend is shown in **Figure 2.5** on Au. It is notable that the adsorption becomes favorable when the surface size is larger than 4×4 . From which we can conclude that the adsorption of OH^- is favorable when the slab is large enough.

To clear knows the distribution of the electrons from OH^- , Hirshfeld charge distribution on Au and Pt before and after the adsorption of OH^- is shown in **Figure 2.6**.

From the Hirshfeld charge distribution point of view, upon adsorption of OH^- on Au and Pt, more than half of the charge is transferred from the OH adsorbate to the surface, in total, the two charges from the OH^- have been well kept on the symmetric surface, and no counter charges are shown which may reduce the surface charge. More electrons are transferred into the surface on Pt, showing the stronger adsorption of OH^- on the Pt surface compared to Au.

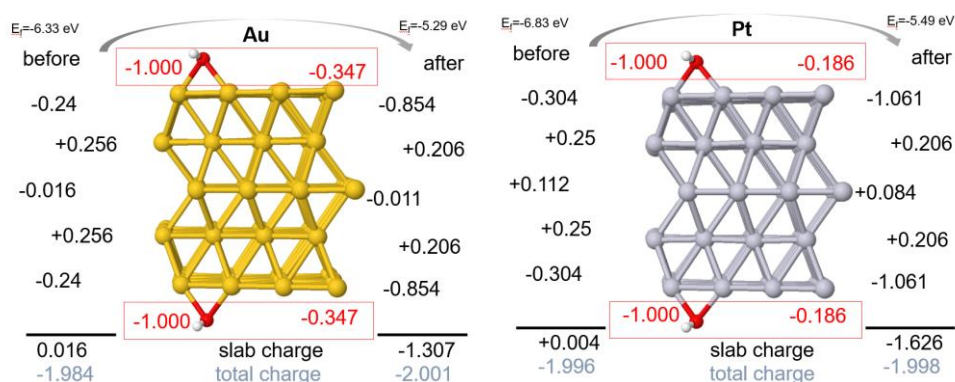


Figure 2.6 Hirshfeld charges distribution per 16 atom of Au (left) and Pt (right) before and after the adsorption of OH^- , E_f represents the Fermi energy, red numbers show the charge on OH adsorbate, total charge represents the charge of the symmetric slab including the adsorbate, slab charge represents the charge on the surface.

In summary, an electron per surface exposed was injected into a $p(4 \times 4)$ surface to build a negatively charged surface to mimic the basic system, so in the symmetric slab we in total introduced 2 electrons, and in the symmetric slab we have a 2×16 surface atoms with 2 electrons in total, following the method we used and validated previously to capture the promotional effect of anions in formic acid dehydrogenation catalysed by palladium⁸⁵. In the following, the metallic slab without charge is called “neutral system” and the metallic slab with an extra electron per 16 surface atoms will be called “basic system”.

2.4 Ab-initio thermodynamics

As a fundamental issue in the heterogeneous catalysis, determining the surface morphology of the catalysts under different conditions plays a critical role for the following reactivity study. The transition of the surface becomes more complicated when it is exposed in the environment under reaction intermediates, especially when the surface concentrations of certain reaction intermediates becomes so high that the catalytic surface becomes a new compound material composed of the original catalyst material and the reaction intermediate, which becomes the actual catalysts¹¹².

To determine the surface morphology, surface energies under different environments are needed to be computed. We start from the simple symmetric slab first. To compare the possibility of the surface morphology under different conditions, the surface energy of them should be computed:

$$\gamma_{sym}(T, \{p_i\}) = \frac{1}{2A} \left[G - N_{bulk} G_{bulk} - \sum_i N_i \mu_i(T, p_i) \right] \quad \text{eq 2.4.1}$$

Where γ_{sym} is the surface energy of a symmetric slab, G is the Gibbs free energy of the slab, G_{bulk} is the Gibbs free energy of the bulk of the slab, N_{bulk} is the number of bulks composing the slab, A is the surface area, in the symmetric slab, both the top surface and the bottom surface have the same surface area, so here in total divided by 2, N_i is the number of molecules of the i th species adsorbed on the surface, $\mu_i(T, p_i)$ is the chemical potential of the i th species under temperature T and pressure p_i , $\{p_i\}$ represents the various partial pressures of different species. Considering the importance of some vacancies, the complexity of the different terminations of the slab, the surface energy of an asymmetric surface should also be taken into consideration. The solution is to build a symmetric slab first, then delete the γ_{sym} from the total surface energy of the two asymmetric bottom and top surface:

$$\gamma_{asym}(T, \{p_i\}) = \frac{1}{A} \left[G - N_{bulk} G_{bulk} - \sum_i N_i \mu_i(T, p_i) - \gamma_{sym} \times A \right] \quad \text{eq 2.4.2}$$

Where γ_{asym} represents the surface energy of the exposed surface from an asymmetric slab, γ_{sym} represents the surface energy from the symmetric slab.

Normally $G \approx E$ (electronic energy of the slab), and $G_{bulk} \approx E_{bulk}$ (electronic energy of the slab), to get the surface energy, chemical potentials of adsorbates in gas phase should be computed:

$$\begin{aligned} \mu_i(T, p_i) &= \mu_i(T, p^0) + k_B T \ln \left(\frac{p_i}{p^0} \right) \\ &\approx E_i + ZPE - TS_i + k_B T \ln \left(\frac{p_i}{p^0} \right) \end{aligned} \quad \text{eq 2.4.3}$$

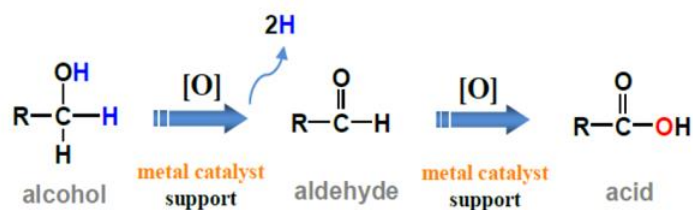
Where E_i is the electronic energy of the i th molecule, $\mu_i(T, p^0)$ is the temperature dependence term including the contributions from vibrations and rotations of the molecule, as well as the ideal gas entropy at standard pressure 1 atm, the term can be found in the JANAF thermochemical tables at 1atm¹¹³, which can also be simplified as the entropy term multiplies with the temperature TS_i , k_B is the Boltzmann constant, p_i is the partial pressure of the i th species, p^0 is the standard pressure 1 atm we mentioned before.

Chapter 3 Alcohol oxidation on Au in neutral and basic environment

As important biomass derivatives, different kinds of alcohols, such as glycerol, sorbitol and so on, are used as the feedstocks of many useful chemicals. One of the critical products from alcohol are the corresponding acids. Acids are widely used in our daily life, such as acetic acid used as flavor in food industry, salicylic acid playing the role of anti-inflammation in medical industry and cosmetology, acrylic acid used as precursors of polymers, and the home personal care products which can be seen everywhere which consists of AECA (alcohol ether carboxylic acids).

Pathways of alcohol oxidation

Nowadays the greenest way for the production of acids is to use O₂ as oxidant and directly oxidize the corresponding alcohol to acid with metal catalysts. The most widely used catalysts for alcohol oxidation are Pt and Pd, which can always give a good selectivity and a relatively good yield^{14,114,115}. Recently gold also shows its potential in many important industrial reactions especially in low-temperature and highly selective oxidative reactions including alcohol oxidation¹¹⁶. To avoid the high cost on the noble metal catalysts, many cheaper metals such as Cu are more and more used especially as the second additional metal in the original noble metal catalytic system^{37,40,117,118}. The general mechanism of the alcohol oxidation to acid is widely accepted by researchers that alcohol oxidation proceeds by dehydrogenation to an aldehyde and finally become the acid^{88,111}, as shown in [Scheme 3.1](#).



Scheme 3.1 General mechanism of alcohol oxidation to acid

It is inferred by some researchers that the role of O_2 lies in the electron and H^* acceptor¹¹⁹. Hayashi found that the selective oxidation of alcohols to aldehydes on Pd/C in acetonitrile can occur without the addition of O_2 into the solution, demonstrating that the oxidative dehydrogenation of alcohols does not require O_2 present, and it merely requires an electron and H^* acceptor such as ethylene¹¹⁹. However, no study shows the alcohol oxidation can proceed to acid in absence of O_2 . Also, no detailed study on the transferring of electrons from surface to O_2 is shown when they declare that O_2 plays the role of electrons acceptor. What's more, it remains a debate on which molecule provides the second O atom in acid, which used to be thought that it may come from the activation of O_2 molecules in solution. However, it is proposed by Zope using isotope labeling that the second O in the produced acid is not from O_2 but from H_2O ¹⁰⁶, which indicates that O_2 does not directly take part in the reaction and the real oxidant may have different forms rather than O_2 , also, the water should take part in the activation. Learning from the CO oxidation, we know that the O_2 activation is the one of the highest priorities, as O_2 does not readily dissociate and water molecules can enhance the CO oxidation in the gold catalysis¹²⁰. And it is indicated by many researchers that O_2 activation is the rate determining step in alcohol oxidation^{108,121,122}.

To reduce the high energy barrier of the O_2 activation, some promotion methods have been studied. The most widely used method is to assist the O_2 activation by the addition of water. It is worth noting that the role of water has already been confirmed in the CO oxidation, where the addition of water environment accelerates the total reaction and the water is considered to play its role in activating oxidant O_2 molecule^{120,123,124}. In the benzyl alcohol oxidation, it is found the alcohol conversion in water is 3 times larger

than in no solvent reaction, the more water the larger the conversion is⁵⁷. The necessity of the participation of H₂O in the O₂ activation is also reflected by the high activation energy of O₂ especially on Au, where the direct O₂ activation barrier on Au is +2.10eV and +0.88eV on Pt¹²⁵. Chang¹²⁶ put forward that the promotion role of water mainly in three aspects: (i) solution like effects, (ii) water mediated H transfer and (iii) OH species from O₂ activation assisted by H₂O. The mechanism of water-assisted O₂ activation on gold has been concluded by Tran¹⁰⁷ as shown in **Figure 3.1**.

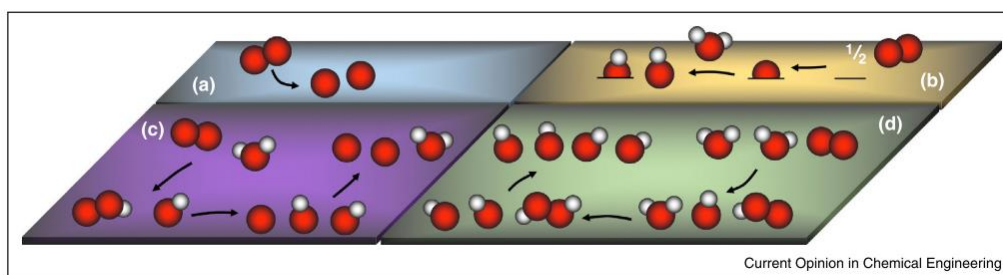


Figure 3.1 Formation of active oxygen intermediates from O₂: (a) O₂ dissociation; (b) hydroxyl formation with a pre-existing O atom (in the common case of metal-oxides, the pre-existing O atom is a lattice oxygen); (c) water-assisted O₂ dissociation; and (d) O₂ activation with excess water reproduced from Tran's work¹⁰⁷

It can be seen from **Figure 3.1** that O-atom-contained oxidant species can exist in the form of O, OH, OOH. Except directly taking part in the O₂ activation, the water solution is also found to facilitate the O₂ activation process mainly by offering electrons flowing to the 2π* orbitals of O₂ induced by hydrogen bonds and stabilizing the transition states¹²⁷.

Except the water-assisted pathway, it is also proposed by Mucoz-santiburcio that the negatively charged AuNP enhances the activation of the O₂ molecule at the perimeter site of the catalyst¹²⁸. Similar properties have also shown by Okumura¹²⁹ that O₂ becomes easier to be activated when adsorbed on an anionic Au atom on the surface of the Au clusters. Considering the importance of the water, some researchers point out that explicit water is necessary especially when it involves polar adsorbates¹³⁰.

As we mentioned before, many O contained species may appear, and it is also pointed out by many researchers that the O^{108,111}, OH^{106,108,111,131} and OOH¹⁰⁸ should be the starting engine of the alcohol reaction, considering the very first step of the alcohol

oxidation, no matter the O-H cleavage or the C-H cleavage, both have a rather high barrier when occurring a direct cleavage without any promotion species around^{106,108}. Luckily, the first step becomes much easier with the help of the promotional O contained species as we mentioned before. Experiments were also shown by Ketchie that appreciable concentrations of peroxide in the product mixture formed during glycerol oxidation over Au/C, whereas only trace amounts of peroxide were detected when Pd/C was used as a catalyst¹³². Thus, they proposed that peroxide formation is a general characteristic of Au-catalyzed oxidation. Nonetheless, the large amount of H₂O₂ in the solution not only indicate the formation of H₂O₂ from the O₂ activation, but also reveal the difficulty in activating H₂O₂ by Au, and it did not exclude other possible pathways of O₂ activation that are easier to be activated compared to H₂O₂. Thus, in our following study, to figure out the most favorable O₂ activation pathway among all the possible ones is still a critical point in confirming the complete pathway from alcohol to acid.

In addition to the complexity of the activation of O₂ molecules, the intermediates among the general mechanism as we show in **Scheme 3.1** also arouse many discussions. For the very first step, Zope found the O-H cleavage is almost a non-barrier step when assisted by OH* no matter on Pt or on Au¹⁰⁶. However, it is believed on Pd, the first step in neutral environment should be the α -C-H cleavage, as the α -C-H cleavage is not so high to overcome even without the help of oxidant¹¹¹. Here they consider the more the OH species covered on the Pd surface the higher the pH is, which is a widely used treatment of mimicking basic environment, but taking no consideration of the charge effect from OH⁻. And it is considered that under high pH, the first step should still be the O-H cleavage with the help of OH around on Pd. From aldehyde to acid is thought to be quite easy, the reaction can even occur smoothly in organic solution¹³³. The facility of the latter half of the alcohol oxidation suggest the rate determining step of the alcohol oxidation should be before the generation of aldehyde. In fact, many researchers have already studied the alcohol oxidation, and proposed that the α -C-H cleavage should be the rate-determining step^{21,134–136}.

Different metals used as catalysts in alcohol oxidation

Platinum is thought to be the most favorable catalysts in alcohol oxidation no matter in thermal catalysis or in electrocatalysis. When catalyzed by Pt, the alcohol can be oxidized to acid even in neutral and acid environment¹³⁷, but become less active and less selective compared to reaction in basic environment as the products become mainly aldehyde and ketone in the absence of base while just a few acids can be observed¹⁰⁶.

Using Pt as the oxidation catalysts, the catalyst itself will also face the severe problem of overoxidation^{44,115,138}, as it is confirmed by experimentalists that the active surface should be the pure Pt surface rather than Pt oxide surface^{44,138}. The overoxidation of the catalysts become more severe with the increasing of the pH, and through a dynamic kinetic calculation, they found the main cause of the overoxidation lies in the adsorption of hydroxyl ions from basic environment¹³⁹. The overoxidation not only reflects in the overoxidation of the catalysts, but also in the overoxidation of products, where the products may be overoxidized to CO₂ or other C-C bond breaking product^{10,13}. Pt catalysts also has the drawback of poisoning by the strong binding of products or byproducts, which also disfavors the desorption of the acid product into solution^{44,140}.

Then gold is found to also work quite well in the alcohol oxidation reactions. Gold was thought to be an inert metal which cannot be used in catalysis until Haruta¹⁴¹ found it is a quite active catalyst in the low-temperature CO oxidation. After that, gold has been a hot topic in catalysis for several decades. It is now used as catalysts for many kinds of reactions, such as alkene hydrogenation^{142,143}, CO oxidation¹⁴⁴ and alcohol oxidation^{106,145}.

In basic environment, high selectivity and conversion from alcohol to acid is detected and no C-C bond breaking during the reaction^{13,106,146}. For example, in the oxidation of ethylene glycol (EG) to glycolate, the selectivity of Au is larger than 90% while only around 70% for Pt¹¹⁴. The turn over frequency is also much better in the ethanol oxidation catalyzed by Au in presence of base rather than Pt¹⁴⁷. The Au catalysts also represent a good stability even after several catalytic cycles¹⁴⁸.

However, when the alcohol oxidation is performed in absence of base, it is found that no alcohol conversion is observed over Au^{13,36,106}. Experiments show that the reaction is stuck in the alcohol to aldehyde step on Au in the absence of base, as the step from aldehyde to acid can occur smoothly in the neutral or even in the organic media as we mentioned before. It is important to perform the reactions in a base-free environment, which not only obeys the law of green chemistry, but also avoids the generation of carboxylates. Then to unravel the role of base become much more critical, and we will disclose the function of basic environment in Chapter 3.2.

According to the previous study respectively on pure Au and pure Pt, it is naturally to think of generating an alloy based on the two metals, which can combine the advantages of both of the metals and avoid the disadvantages of them. This enhancement of the alloy compared to the pure metals is often caused by two alloy effects, the ensemble and the ligand effect. The ligand effect represents the electronic effect of the metal that the chemical potential of the atom changes, consider the ligand effects when the binding atoms are not the same atoms. The ensemble effect represents the geometrical effect that the chemical composition of the ensemble atom changes, which mainly results in the changing of the adsorption sites¹⁴⁹. Activation energy of a reaction is more sensitive to ensemble effects as the transition states normally take up more than two surface atoms, then the distribution of all kinds of atoms affects a lot on the building of transition states. Thus, it is easy to understand that the small molecules or species are affected more by the ligand effect due to its small occupied area¹⁵⁰.

Considering the issue of cost, a much cheaper but still quite stable metal Cu, is designed to substitute Pt in the alloy. As a pure metal, Cu/Al₂O₃ is found to be an outstanding catalysts in the ethanol oxidation to acetic acid with high selectivity (nearly 100%) and relatively high conversion (>80%) at room temperature in neutral environment oxidized by tert-butyl hydroperoxide (tBuOOH)¹⁵¹. As a promising alloy, the AuCu alloy catalysts have recently been tested and found to be useful catalyst in many catalytic alcohol oxidation reactions^{37,40,117,118}. Compared to Au, Cu is more vulnerable

to oxidants, so Cu normally exists in the form of CuO_x or isolated cations in the AuCu alloy catalyst^{37,118}. And the CuO_x patches on Au nanoparticles and on support is considered to play a role of a promoter to provide reactive oxygen. In the glycerol oxidation, as the second metal of the AuCu/ZnO catalyst, the addition of Cu largely increases the conversion of glycerol in glycerol oxidation in basic environment from 50% to 95% with a constant selectivity of glyceric acid of around 60%, and the negatively charged Au center here is quite active for oxygen chemisorption¹¹⁸. Luckily, with the help of second metal Cu, Au can get rid of base in some alcohol oxidation cases such as the glycerol oxidation³⁷, however with a very low conversion. In Chapter 3.3, an AEO oxidation catalyzed by AuCu alloy is studied to especially show the role of the Cu metal in the alloy.

3.2 Unravelling the role of base and catalyst polarization in alcohol oxidation on Au and Pt in water

3.2.1 introduction

Obtaining carboxylic acids from alcohol oxidation is a key process, especially for the upgrading of biomass.¹⁵² To reach the standards of Green Chemistry, using the oxygen from air as a final oxidant is a necessity, but this requires the development of selective and stable heterogeneous catalysts, capable of activating O₂ in aqueous conditions.¹⁴⁷ Pt is one of the most popular catalysts used in alcohol oxidation^{44,153} despite a number of flaws that depend on the experimental conditions: deactivation by catalysts oxidation in basic medium,^{14,44,115} poisoning by products or by-products in acid medium,^{44,140} selectivity issues with unwanted C-C cleavage,^{10,13} or limited oxidation of the substrate in acid conditions.¹⁰⁶ To reach good conversion and better selectivity to the acid, a base has to be added but a hydrolysis step is then required to recover the acid from the carboxylate salt. Another drawback of the use of a basic environment is the possible poisoning of Pt by hydroxide anions.¹³⁹ Thus, avoiding the introduction of a base while keeping a good activity and selectivity toward the acid is still a critical challenge. Prati et al.¹⁴⁵ found that Au catalysts also show a high activity and selectivity in alcohol oxidation even with large nanoparticles of at least 7 nm. Compared to Pt, Au is more selective to the corresponding acid, and more stable over several cycles.¹⁴⁸ However, it is even more demanding regarding the basic environment, with generally no activity observed neutral medium.¹⁴⁶

To improve the catalytic activity and selectivity for alcohol oxidation by O₂ without addition of a base, a deeper understanding is necessary to rationalize why such a basic medium is mandatory. Experimental and computational mechanistic studies^{106,111,140,154} indicate that the reaction goes through the alcohol → aldehyde → acid path. The O₂ activation is thought to be rate-determining,^{108,155} but it should be facilitated by the

presence of water,^{108,127,131} which can directly participate to the oxidation reaction.¹⁰⁶ Last, according to computational studies, the importance of maintaining a basic pH can be related to the coverage of OH on the surface^{21,111} that can assist for instance the O-H and C-H cleavages in the alcohol.¹¹¹ In those studies, the chemisorbed hydroxyl is modelled as a radical and not as an anion, and thus it could as well be generated from water and O₂.¹⁰⁶ Accordingly, the origin of the activation of the catalysts by adding hydroxide anions is still unclear, hampering a rational design of a catalytic system that would circumvent such a basic environment.

In our study, we aim at unraveling the role of the base by a computational mechanistic study in order to propose mitigations solution to limit its usage. We investigate here the contrasted behaviors of Au and Pt in neutral and basic environment (with a polarized interface) for each stage of the catalytic process: O₂ activation, ethanol oxidation into the acid, and desorption of the product, namely the carboxylic acid or the carboxylate anion depending on the environment.

3.2.2 Computational details

Dispersion corrected DFT (DFT-dDsC)⁷⁷ calculations were carried out with the Vienna ab initio simulation package (VASP)^{156–158}. The exchange and correlation terms were obtained by the Perdew–Burke–Ernzerhof form of Generalized Gradient Approximation (GGA-PBE)⁶⁹ functional. The projector-augmented wave (PAW) pseudo potentials⁸¹ are used during the calculation with a cut-off energy of 400eV. A 5-layer mirror symmetric model was used to model Au(111) and Pt(111) surface to do the dipole correction especially when electrons are introduced into the surface, and only the middle layer was set to be fixed while others were allowed to relax. Here we use the most stable Au(111) surface. This choice was done based on the study of Liu et. al²¹ showing that the adsorption is not so sensitive to the sites, but also based on the experimental demonstration that the alcohol oxidation turn over frequency is linearly correlated with the number of external gold atoms¹³⁴. The optimal cell parameter of Au is 4.14 Å and

3.96 Å for Pt, which is quite close to the experimental data (4.08 Å for Au¹⁵⁹ and 3.92 Å for Pt¹⁵⁹). All the computations were performed in a p(4×4) unit cell with K-point mesh of 3×3×1 on Au and 5×5×1 on Pt. Implicit solvent through Poisson-Boltzmann (PB) continuum approximation^{160,161} was used to take solvent effect into account, which was implemented by Hennig group in VASPsol¹⁶². The surface tension was set to zero to obtain a numerical stability, and the debye length was set to 3.0Å to consider the electric-field screening effect in electrolyte solvent. A large total cell height of 40Å is used, which led to a vacuum layer of around 30Å. On the one hand, the vacuum layer could be used to avoid the interaction between two metallic slabs, on the other hand, such a large vacuum layer has to be used to obtain a constant potential to mimic the vacuum situation especially when we introduced electrons into the slab. Geometric optimization in solvent would reach a convergence when a gradient was smaller than 0.02 eV/Å and when the energy was converged to 1×10⁻⁶ eV. Test with spin-polarized calculations for O₂ adsorption indicate a singlet state, and hence all calculations were performed using non spin-polarized calculations.

The procedure of symmetrisation started from the asymmetric slab. We first optimize the adsorbates on the asymmetric surface, then based on the structure, we built the symmetric slab followed by another optimization to obtain the final structure on symmetric slab.

The transition states were determined by nudged elastic band (NEB) approach¹⁶³ followed by a quasi-Newton (QN) optimization to obtain the saddle point. All the transition states were first founded on the asymmetric surface (it is confirmed by the presence of one and only one imaginary frequency), then the structures of the transition states were kept and the symmetrisation was done based on the kept structures, after that another QN optimization would be done, the final transition state was confirmed when there were in total two imaginary frequencies, one symmetric and one asymmetric frequency. In the frequency calculation, only the degrees of freedom of the organic fragment were included.

A $20 \times 20 \times 20 \text{ \AA}^3$ unit cell was used to optimize the structures of molecules, radicals and ions in solvent. It is notable that when calculating the triplet or doublet states, spin polarized calculations were performed, such as O_2 and all the radicals, but when dealing with close-shell molecules and all adsorbates on the metallic surfaces, restricted calculations were performed.

The energetic span model offers a straightforward method to obtain the free energy barrier of catalytic cycles based on its computed energy profile.¹⁶⁴ The method takes both the driving force of the catalytic circle and the TDTS (TOF-determining transition state) and TDI (TOF-determining intermediate) into account. The energetic span δG is defined as:

$$\delta G_{\text{span}} = \begin{cases} G_{\text{TDTS}} - G_{\text{TDI}} & \text{if TDTS appers after TDI} & \text{(a)} \\ G_{\text{TDTS}} - G_{\text{TDI}} + \Delta G_{\text{r}} & \text{if TDTS appears before TDI} & \text{(b)} \end{cases} \quad \text{eq. 3.2.1}$$

$$\delta G_{\text{span}} = G_{\text{TDTS}} - G_{\text{TDI}} + \Delta G_{\text{r}} > G_{\text{TDTS}} - G_{\text{TDI}} \quad \text{eq. 3.2.2}$$

3.2.3 Choice of the model for basic environment and catalytic interface

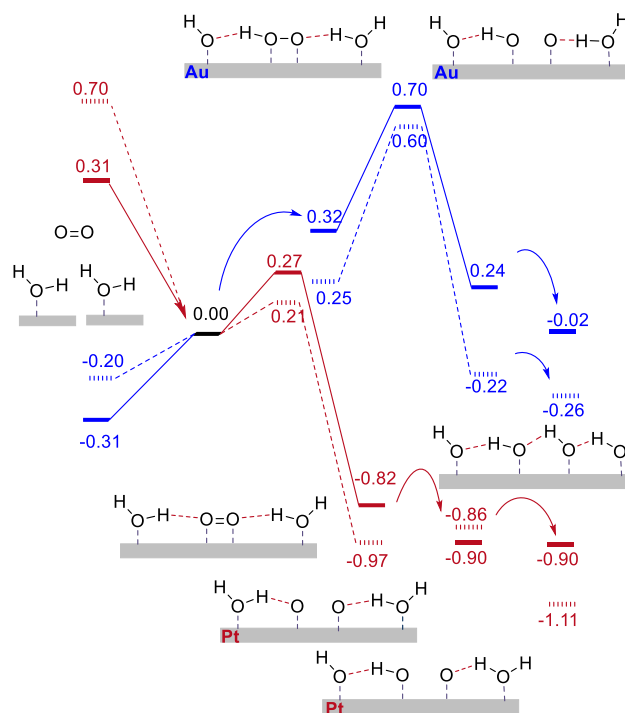
For the first time to our knowledge, anionic OH^- will be explicitly included in a complete catalytic cycle. The anionic species in solution are carefully described combining micro-solvation and a continuum solvent model. The counter charge is described through the Debye-Hückel theory using the linearized Poisson-Boltzmann equation.^{162,165} Since the micro-solvation has been shown to be uninfluential on the alcohol oxidation on $\text{Pt}(111)$ ¹¹ we have chosen to include the water solvent only through a continuum solvent, still supplemented by the linearized Poisson-Boltzmann equation to described the counter-charge at the interface. Typically, the adsorption of a hydroxide anion from the water solution to the Au/water interface is endothermic with adsorption energy of +0.01 eV. This anion easily transfers most of its anionic charge to the metallic slab (see Chapter 2, [Figure 2.6](#)), modifying the surface work function and polarizing the metal/basic water interface. The overall surface charge is controlled by the adsorption of the anionic species and thus their concentration and the ability of the metallic surface to

accept extra charges. A recent study of ours⁸⁵ showed that this effect is well reproduced computationally with the injection of a negative charge per 9 surface atoms. Careful tests in Chapter 2, **Figure 2.5** demonstrated that in our system, a p(4×4) surface is more proper in adsorbing OH⁻ onto the Au surface, so in the following study, a charged p(4×4) surface is used. This negatively charged catalyst should be more active towards O₂ dissociation.¹⁶⁶

3.2.4 Comparison of ethanol oxidation on Pt and Au in neutral and basic environment

3.2.4.1 O₂ activation in presence of water

The oxidation by oxygen necessitates to break the O=O bond. This is one of the major roles of the metallic catalyst. In aqueous environment, this step is facilitated by the presence of water as already shown in the literature, yielding to surface hydroxyls.^{108,127,131} The reactive sequence is complex since three bonds at least need to be broken, (one O=O and two O-H) and two bonds have to be formed (two O-H). These bond ruptures/bond formations can be either sequential or synchronous. We have systematically studied the possible paths to convert O₂ and two water molecules into four hydroxyl species adsorbed on Pt and Au, with and without a basic environment. We show the preferential path on Au and Pt in **Scheme 3.2** and the 6 others can be found in **scheme A 3.2.1**.



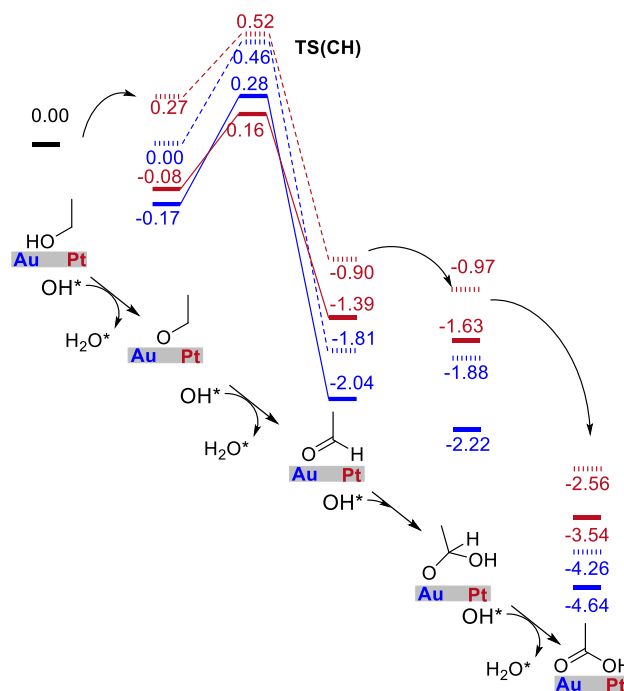
Scheme 3.2 Gibbs energy profiles (in eV) at 25°C are shown on Au(111) (in blue) and on Pt(111) (in red) in absence (straight lines) and in presence (dashed lines) of a basic environment. All proton transfers are “barrier-less” (with the energy of transition states not higher than the reaction energy, or the barrier is lower than 0.05eV) and thus are indicated by a curved arrow. O₂ adsorption is shown with a straight arrow.

On Au in neutral conditions, O₂ adsorption is endothermic by 0.31 eV. The O₂ activation starts with an H transfer from water, generating a first chemisorbed hydroxyl (OH*) and a hydro-peroxide intermediate (OOH*). This barrier-less step is followed by the O-O scission in OOH* yielding an adsorbed atomic oxygen O* and a second OH*. It is the most difficult step with an O-O distance of 1.91 Å in the transition state and an overall barrier of 1.01 eV. Then, the second water molecule transfers easily an H to O*, producing the last two OH*. The overall process is endergonic starting from gas phase O₂ (+0.29 eV). Let’s turn now to the modeling of a basic environment, with one electron per 16 surface atoms added to the gold slab. Importantly, the adsorption becomes easier (+0.20 eV) and so does the overall process (-0.06 eV). The O-OH scission is also facilitated, with an overall barrier of 0.80 eV only and the H-transfers are still barrier-less. On Pt, O₂ activation is much easier, with a barrier of 0.27 eV for the direct scission

of O₂ co-adsorbed with two water molecules. The atomic O is particularly stable but the subsequent H transfers are still easily accessible. In basic conditions, the generation of OH* is even easier and strongly exergonic (-1.81 eV). In a nutshell, in presence of O₂ and neutral water, the Pt surface is covered by chemisorbed radical OH*, that are not related to the presence of a basic environment as it is often proposed, but to the concomitant presence of O₂ and water. This is less likely on Au since the generation of OH* is slightly endergonic. A major effect of the basic environment is to facilitate O₂ adsorption and generation of OH* on Au. On Pt, the very strong exergonicity suggests an easy over-oxidation of the Pt surface typically into a thin overlayer of α -PtO₂.

3.2.4.2 Ethanol oxidation into carboxylic acid by OH*

The occurrence of OH* strongly facilitates the C-H and O-H bond scission in ethanol yielding aldehyde, which has been discussed in the 3.2.3.1 and 3.2.3.2. In other words, OH* acts as a base while the metal act as a Lewis acid. This pair does not require a basic environment to be generated, only the presence of water and molecular oxygen. Yet, this paired site is particularly efficient at performing the alcohol oxidation on both Au and Pt as shown in [Scheme 3.3](#).



Scheme 3.3 Gibbs energy profile (in eV) at 25°C are shown on Au(111) (in blue) and Pt(111) (in red) in absence (straight lines) and in presence (dashed lines) of a basic environment. Most steps are barrier-less except the C-H bond breaking in the ethoxy inter-mediate.

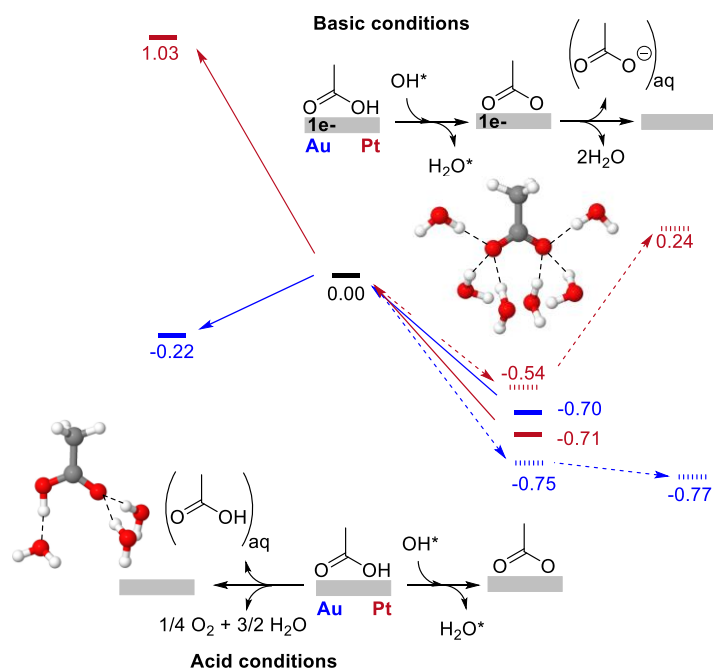
In a basic environment, the polarization of the metal/solvent interface with electron accumulation at the surface and cations in the solution strongly modify the relative stabilities for OH^* and EtO^* . OH^* adsorbs with its dipole moment almost parallel to the surface and is strongly stabilized compared with the non-polarized situation. Conversely, EtO^* is adsorbed in a hollow site, its oxygen being at a very short distance from the metallic surface ($\sim 1.37 \text{ \AA}$). Hence, its dipole is perpendicular to the polarized surface with an orientation that is destabilizing, the negative oxygen being close to the negative surface. Those two effects add up, pushing up in energy the $\text{EtO}^* + \text{H}_2\text{O}^*$ intermediates relatively to $\text{EtOH}^* + \text{OH}^*$ on the polarized interface as shown in **Scheme 3.3**.

The O-H breaking is followed by the C-H one, consuming a second OH^* . The C-H scission is the most difficult step with a barrier of 0.45 eV on Au(111) and 0.24 eV on Pt(111). The resulting acetaldehyde is further oxidized by the addition of a third OH^* yielding to CH_3CHOOH . Last, a C-H bond dissociation assisted by a fourth OH^*

produces the expected acetic acid and water. Not only the basic environment pushes up in energy the EtO* intermediate but also the following C-H scission transition state by 0.18 eV on Au and by 0.36 eV on Pt. This detrimental effect of the base is surprising, however, a direct comparison with the experimental results necessitates considering the full catalytic cycle, as done later. Let's note in passing that OH* originates from O₂ or water and can easily be exchanged with surrounding water solvent molecules through a surface Grotthus mechanism. Thus, the oxygen atom that is incorporated in the produced acid comes very likely from a water molecule, in agreement with the observations by Zope et al. using ¹⁶O₂ and H₂¹⁸O.¹⁰⁶

3.2.4.2 Desorption

Once the acetic acid is formed on the surface, the question of its further oxidation vs. its desorption raises. The corresponding profiles are shown in Scheme 3.4 along with the micro-solvated structures considered in solution to ensure a refined description of its transfer from the metal/water interface to the bulk water.



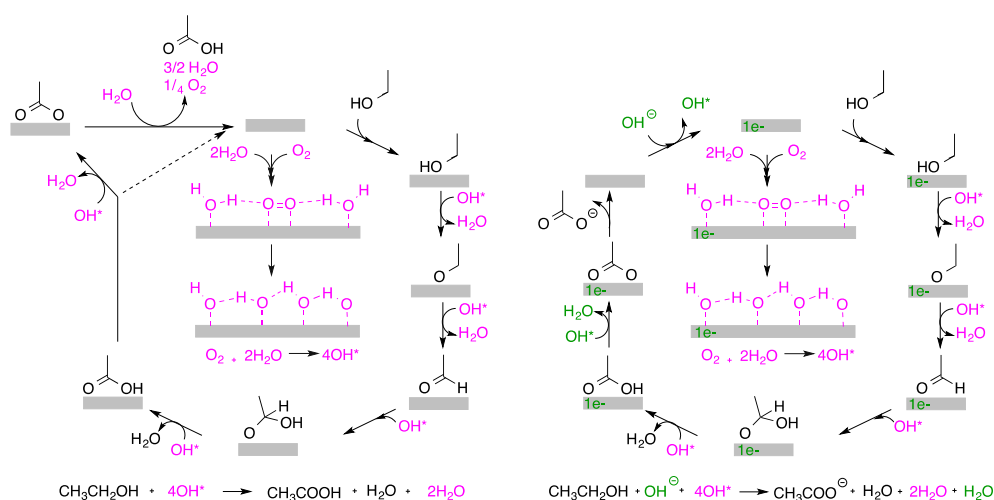
Scheme 3.4 Gibbs energy profile (in eV) at 25°C are shown in absence (straight line) and in presence (dashed line) of basic conditions, using CH₃COO* acid and OH* as a reference.

In presence of a pressure of O₂, as seen earlier, OH* can be generated from O₂ and water. Acetic acid is easily oxidized into acetate in a barrier-less H transfer from the acid function COOH* to the co-adsorbed hydroxyl OH*. This step is strongly exothermic on both Pt (-0.70 eV) and Au (-0.71 eV), generating a very stable neutral CH₃COO* intermediate and a water molecule. This is a thermodynamic sink. Since the C-C scission is particularly difficult,¹³ this acetate intermediate either poisons the surface, or is re-protonated with a H-transfer from this water molecule. Then, CH₃COOH can desorb as acetic acid in acidic conditions. This re-protonation is hence accompanied by the co-generation of OH*. To regenerate the catalytic surface and avoid over-oxidation, this OH* has to be desorbed as ¼(O₂+2H₂O). The cumulated desorption of CH₃COO* and OH* costs 1.74 eV on Pt, which clearly demonstrates that those species poison this metal. On Au, the overall desorption endergonicity is 0.48 eV but it necessitates to go through an intermediate state (CH₃COOH*+OH*) that costs 0.70 eV. In basic conditions, the situation drastically changes. The de-protonation of the chemisorbed acetic acid is performed by OH* on a negatively charged surface. This system represents the chemisorbed hydroxide *anion* and this process is a typical acid-basic reaction. It is less exergonic than in neutral environment by 0.17 eV on Pt and a bit more exergonic by 0.05 eV on Au. As we have already seen previously, OH* is particularly stabilized at the polarized interface. In addition, the carboxylate dipole is perpendicular to the surface, in a destabilizing orientation. However, this situation is less detrimental than in the case of EtO* since oxygen atoms of CH₃COO* are adsorbed on top sites farther from the surface (2.26 Å). Finally, the resulting water and *anionic* acetate desorb directly in the water solution, leaving behind the *neutral* surface. The acetate anion is stabilized in water, which facilitates its desorption compared with the one of acetic acid with a cost of only 0.78 eV on Pt and no desorption barrier on Au. In short, the base clearly prevents the poisoning of Pt by CH₃COO*.

3.2.4.3 The comparison of the whole reaction

For each model reaction condition (acidic and basic), the overall catalytic cycles are

represented in **Scheme 3.5** and the corresponding energetic span,¹⁶⁴ TOF-limiting intermediate and TOF-limiting transition state are collected in **Table 3.1**. The full reaction paths are reported in **Figure A3.2.1** and **Figure A3.2.2**. Our model reproduces nicely the strong promotion of Au and Pt supported catalysts in basic conditions,^{36,106} with a marked decrease in the energetic span from 1.58 eV to 0.97 eV on Au and from 1.74 eV to 0.78 eV on Pt. In neutral environment, the reaction catalyzed by Au is strongly limited by the lack of ability in splitting the O-O bond in O₂, cumulating an endothermic adsorption of molecules, a high activation barrier and a desorption barrier (+0.40 eV, 0.70 eV and 0.49 eV respectively, see **Figure A3.2.1**). On Pt, the reaction is poisoned by the over-oxidation of acetic acid on the surface, leading to a high desorption barrier (1.74 eV), in line with the observed quick deactivation and the higher selectivity towards the carbonyl.⁴⁴ In basic environment, the desorption barrier is lowered both on Au and Pt (barrier-less and 0.78 eV respectively) which mainly contributes to the decrease of the energetic span. On Au, the strong activation not only comes from the easier desorption but also from the easier activation of O₂ activation (from 0.70 eV to 0.60 eV, see **Scheme 3.2**). The study shows the different features of the alcohol oxidation on Au and on Pt, that the difficulty of Au-catalyzed alcohol oxidation lies in the O₂ activation while the poisoning by by-product acetic acid species raise difficulties on Pt.



Scheme 3.5 Overall catalytic circle in (left) neutral and (right) basic environment

Table 3.1 Energetic Span (δG , eV), reaction Gibbs Free energy at 25°C (ΔG , eV) TOF-Determining intermediate (TD-Int) and TOF-Determining Transition State (TD-TS) in different conditions.

Conditions	Metal	δG	ΔG	TD-Int[a]	TD-TS[b]
Neutral	Au	1.58	-4.47	CH ₃ COO*	TS(O-OH)
	Pt	1.74	-4.47	CH ₃ COO*	Desorption
Basic	Au	0.97	-4.92	solution	TS(O-OH)
	Pt	0.78	-4.92	CH ₃ COO*	Desorption

3.2.5 Discussion

From those results, we can foresee several potential ways to improve the oxidation catalysts. Combining Au and Pt in an alloy with a majority of Au is an obvious strategy that enhances the O₂ activation and avoids the strong adsorption of the over-oxidized acetic acid by limiting the number of sites with two adjacent Pt. Indeed, when alloying Au and Pt in a ratio of 6:4, even supported on acid active carbon, benzyl alcohol can still be oxidized to acid in a base-free condition.¹⁶⁷ Other alloys could be also targeted to tune the charge on Au in a similar way than the anionic charging provided by the basic environment. This could be done by alloying Au and other metals which have a low work function, which can easily transfer electron to Au.¹⁶⁸ For instance, making a surface Au-Cu alloy will increase the electronic charge on Au since Au and Cu have a Fermi level at ~ -5.5 eV and ~ -5.0 eV respectively. In addition to alloying, the addition of anionic promoter such as chlorine or polyvinylpyrrolidone (PVP) could be a promising route.¹⁶⁹ Another line of modification of supported metal catalyst is to play with the support. Support effects are multiple: dispersion, stability of the metallic phase, etc. One key effect is the electronic transfer between the support and the metal. Here again, choosing a support with a high enough conduction band would favor the electronic transfer from the support to the metallic particles. Naya et al. have recently evidenced this relation between the conduction band of the oxide support and the catalytic activity of the supported Au catalysts on the cinnamyl alcohol oxidation.¹⁷⁰ The best activity they found was obtained with the support that yields to the most negative Au (as measured by the

XPS binding energy), namely SrTiO₃. They also show that the activity does not relate to the Brønsted acido-basicity properties of the support, in contradiction with the numerous attempts to replace the homogeneous base by a basic support.¹⁷¹ Those observations confirm our conclusions: one of the major roles of the base lies in the electron donation upon the chemisorption of anionic OH⁻. To replace the base, experimental strategies should envisage playing with the polarization of the metallic nanoparticles.

Notes:

This work can be found in <https://pubs.acs.org/doi/pdf/10.1021/acscatal.8b03494>. Few months after publication we were informed of an inconsistency of the electrostatic reference potential between the VASPsol (i.e. the linear Poisson-Boltzmann model in VASP) and the standard VASP code. The energy correction affects only the charged system, thus an energy difference appears between the neutral and the charged surface like the adsorption of OH⁻ on a neutral surface in our study. With this correction, an OH⁻ adsorption on a p(3×3) on Au shifts from -1.04eV to +0.25 eV. As shown in Chapter 2, this adsorption turns to be endothermic and then exothermic around 1/16 ML, this is why we change all the p(3×3) calculations into the p(4×4) calculations.

Appendix 3.2

The assistance of OH species plays an important role in the alcohol oxidation^{108,127,131}. The possible first step of an alcohol oxidation, either an O-H cleavage or a C-H cleavage, was computed with and without the help of OH species in [Table A 3.2.1](#).

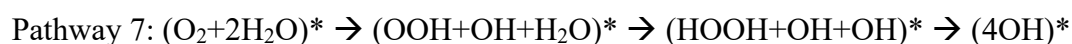
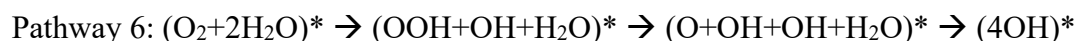
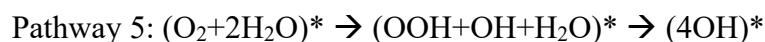
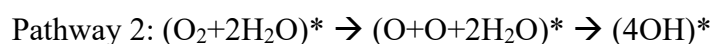
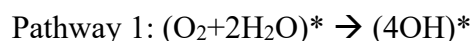
Table A 3.2.1 First step of ethanol oxidation with and without the help of OH in neutral environment

reaction	Au		Pt	
	E_a/eV	E_r/eV	E_a/eV	E_r/eV
$(CH_3CH_2OH + OH)^* \rightarrow (CH_3CH_2O + H_2O)^{*[a]}$	barrier-less	-0.03	barrie-less	0.00
$CH_3CH_2OH^* \rightarrow (CH_3CH_2O + H)^*$	+1.77	+1.47	+1.20	+1.08
$(CH_3CH_2OH + OH)^* \rightarrow (CH_3CHOH + H_2O)^*$	+0.60	-0.74	+0.80	-1.19
$CH_3CH_2OH^* \rightarrow (CH_3CHOH + H)^*$	+1.04	+1.02	+0.44	-0.38

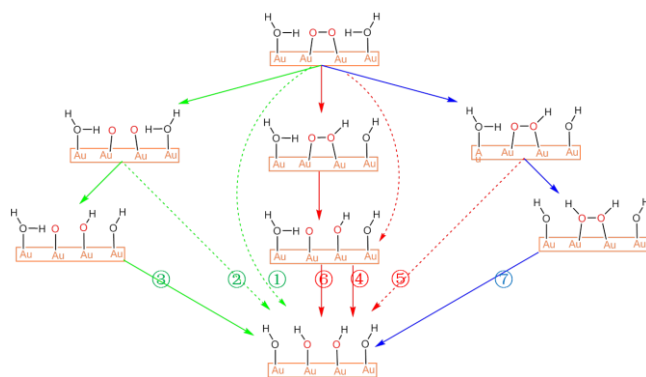
[a] Brackets means the molecules are co-adsorbed.

As is shown in [Table A 3.2.1](#), no matter the C-H cleavage or the O-H cleavage, the assistance of OH* favours a lot both from the thermodynamic or the kinetic point of view. The comparison between the O-H cleavage and the C-H cleavage as the first step of alcohol oxidation here, also determines the initiation step should be the O-H cleavage. Some other oxidant species were also tested, such as O, OOH and O₂, however, none of them is better than OH species. Thus, in the following study, OH is always taken into consideration in the alcohol oxidation.

All possible pathways to convert O₂ and two water molecules into four hydroxyl species adsorbed on Au are shown in [scheme A 3.2.1](#). The same pathways are possible in the case of Pt. Here followed the elementary steps considered for each pathway, where brackets mean the molecules are co-adsorbed, and * means the molecules are adsorbed on the surface:



Although all the possible synchronous steps were considered, some synchronous transition states could not be clearly distinguished from stepwise transition states. The transition state of the most difficult step O-O cleavage we found for Pathway 2 corresponding to the one of Pathway 3, the one of Pathway 4 corresponding to Pathway 6 and the one of Pathway 5 corresponding to Pathway 7, the similar transition states lead to the same reaction barrier, so only the stepwise steps of them are shown in [Table A 3.2.2](#). The corresponding reaction energies, activation energies and the O-O distances in the O-O scission transition states are reported in [Table A 3.2.2](#) for Au. In the case of Pt, according to the previous study on Au, we focused on the stepwise processes as reported in [Table A 3.2.3](#). It is noted that no proper hydroperoxide structure can be found when co-adsorbed with two OH*, which means that hydroperoxide is not a stable intermediate in this case. As we can see from [Table A 3.2.3](#), the direct O₂ activation is quite easy (Pathway 3), so in the case of Pt, the O₂ activation will go through a direct O₂ activation pathway.



scheme A 3.2.1 Simple structural diagram of all possible pathways of O₂ activation, dot lines represent synchronous step, solid lines represent stepwise step, green lines represent O-O cleavage pathways, red lines represent O-OH cleavage pathways and blue lines represent HO-OH cleavage pathways

Table A 3.2.2 Activation energy (G_a , in eV), reaction energy (G_r , in eV) and the O-O distance (in Å) in the O-O scission transition state for the different O₂ activation pathways on Au in neutral and basic environment.

Au	Cleavage order[a]	G_a /eV	G_r /eV	G_a /eV	G_r /eV	O-O distance/ Å	
		neutral		basic		neutral	basic
Pathway1	(HHO)	+1.05		+0.84		1.95	1.86
Pathway3	O-H-H	+1.02		+0.93		1.85	1.87
Pathway6	H-O-H	+0.70	+0.06	+0.60	-0.26	1.91	1.88
Pathway7	H-H-O	+1.11		+1.10		1.85	1.81

[a] Cleavage order: H represents an H transfer, O represents an O-O cleavage, the bracket represents it is a synchronous step with the steps inside occur at the same time.

It is noted that the O-O can be favoured by the charged surface is a general trend. And among all the possible pathways kinetically and thermodynamically, pathway 6 is the most favourable one with go through an O-OH cleavage. The same conclusion was also obtained on Pt in [Table A 3.2.3](#).

Table A 3.2.3 Activation energy (G_a , in eV), reaction energy (G_r , in eV) and the O-O distance (in Å) in the O-O scission transition state for the different O₂ activation pathways on Pt in neutral and basic environment.

Pt	Cleavage order[a]	G_a /eV		G_r /eV		O-O distance/ Å	
		neutral	basic	neutral	basic	neutral	basic
Pathway3	O-H-H	+0.27		+0.21		1.84	1.77
Pathway6	H-O-H	+0.43	-0.90	+0.47	-1.11	1.52	1.51
Pathway7	H-H-O	\		\		\	\

[a] Cleavage order: H represents an H transfer, O represents an O-O cleavage, the bracket represents it is a synchronous step with the steps inside occur at the same time.

The introduction of electron in the Pt catalysts does not affect a lot especially from the kinetic point of view, but it lowers the reaction energy. On Pt, the O₂ activation on Pt goes through pathway 3, where the O-O cleavage happens at the very beginning, which differs from on Au.

The co-adsorption of O₂ and two water molecules will finally generate 4 co-adsorbed OH* as we mentioned before. The two water molecules play the role of stabilizing the transition state of the O₂ activation, which should be surrounded by O₂ in the O₂ activation. However, as the following reaction we focused on the alcohol oxidation, the OH* are not co-adsorbed for the sake of simplification. Thus, it is important to link the O₂ activation with the ethanol oxidation in a smooth way. The sensitivity of the co-adsorbed OH species and single OH species were test in [Table A 3.2.4](#).

Table A 3.2.4 Adsorption energy of four OH species (G_{ads} of 4 OH* /eV) using (O₂+2H₂O) and a bare surface as a reference in function of the coverage intermediate

coverage	G_{ads} of 4 OH* /eV	
	neutral environment in Au	basic environment in Au
1OH*	0.67	0.42
2OH*	0.36	0.26
3OH*	0.14	-0.10
4OH*	0.26	0.04

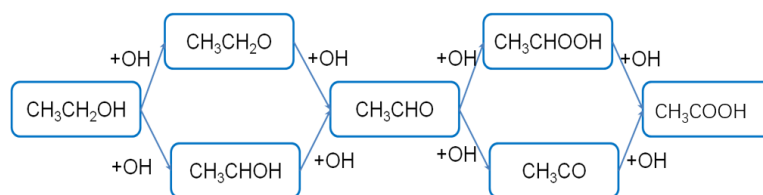
As is shown in [Table A 3.2.4](#), the largest adsorption energy difference up to 0.41 eV, which may lead to an unreasonable barrier if we did not take the co-adsorbed 4OH* in the following reaction. To conclude, the main idea of using the co-adsorbed energy of OH* is to keep consistence and build a bridge between the O₂ activation and the alcohol oxidation. Also, considering in reality, the OH species should also interact with each other on the surface, so it is more reasonable to use the co-adsorbed OH energy rather than the separate one.

So, along the whole pathway, the Gibbs free energy of OH* is always the mean energy derived from this co-adsorbed configuration, using the following relation:

$$G(\text{OH}^*) = (G(4\text{OH}^*) + 3 \times G(^*)) / 4 \quad \text{eq. 3.2.3}$$

in which $G(\text{OH}^*)$ represents the free energy of OH* species we use, $G(4\text{OH}^*)$ represents the free energy of 4OH species co-adsorbed on the surface, $G(^*)$ represents the free energy of the surface. It is worth noting that in all the calculations, the free energy of the OH* is always taken as $G(\text{OH}^*)$ as defined in equation eq. 3.2.3.

The ethanol oxidation into the corresponding carboxylic acid goes through the aldehyde intermediate. For the oxidation of ethanol into acetaldehyde, as we mentioned in the previous section in [Table A 3.2.1](#), the first step is the O-H cleavage with the help of OH. Once the aldehyde is generated, it is oxidized into the corresponding carboxylic acid. Here again, two possibilities depending on the ordering of the two elementary steps (C-H scission and addition of a OH fragment with the formation of a C-OH bond). The energetic data are collected in [Table A 3.2.5](#). Although the C-H cleavage is more exothermic, the OH addition is barrier-less step, so this process goes through the OH addition first and then the C-H cleavage.



Scheme A 3.2.2 The possible pathways from alcohol to acid

Table A 3.2.5 Determination of the third step of the ethanol oxidation

reaction	Au		Pt	
	E_a/eV	E_r/eV	E_a/eV	E_r/eV
$(CH_3CHO + OH)^{*[a]} \rightarrow CH_3CHOOH^*$	+0.07	-0.32	+0.25	-0.26
$(CH_3CHO + OH)^* \rightarrow (CH_3CO + H_2O)^*$	+0.47	-0.95	n/a	-1.56

[a] Brackets means the molecules are co-adsorbed.

Adsorption and desorption free energy

Table A 3.2.6 Adsorption and desorption free energy of molecules

Adsorption	$G_{ads}(O_2)/eV$		$G_{ads}(CH_3CH_2OH)/eV$		$G_{ads}(OH)/eV$	
	neutral	basic	neutral	basic	neutral ^[a]	Basic ^[b]
Au	+0.62	+0.36	+0.04	+0.12	+0.01	+0.06
Pt	-0.48	-0.56	-0.30	+0.07	-0.46	-0.85

Desorption	$G_{des}(H_2O)/eV$		$G_{des}(CH_3COOH)/eV$		$G_{des}(CH_3COO^-)$	
	neutral	basic	neutral	basic	neutral	basic
Au	+0.01	-0.05	-0.16	-0.07	\	+0.07
Pt	+0.31	-0.06	+0.27	-0.11	\	+0.90

[a] Adsorption of OH in neutral environment: $1/4 (O_2+2H_2O)^{+*} \rightarrow OH^*$

[b] Adsorption of OH⁻ in basic environment: $OH^{-+*} \rightarrow OH^*_e$, here * represent neutral surface, *_e represents charged surface.

Energy profile on Au

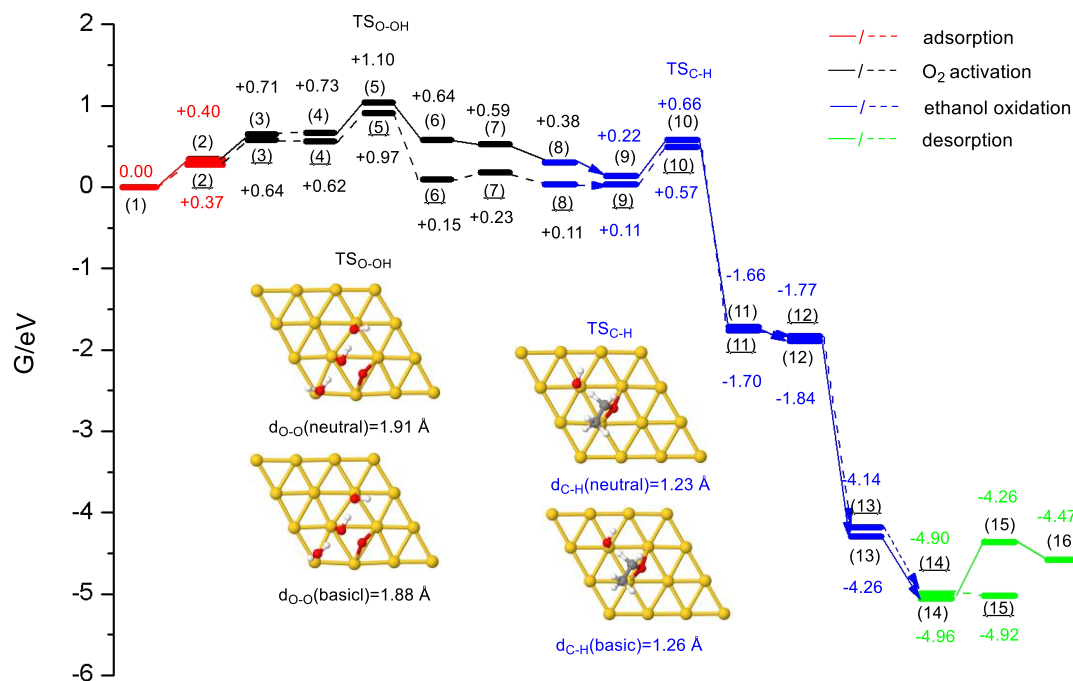


Figure A3.2.1 The whole pathway of alcohol oxidation on Au from adsorption of reactants to desorption of products both in basic (dashed lines) and neutral (solid lines) environment, red represents adsorption, black represents O₂ activation, blue represents alcohol oxidation and green represents desorption

Table A 3.2.7 Determining TDTS, TDI and energetic span on ethanol oxidation on Au

Au	TDTS/G _{TDTS} (eV)	TDI/G _{TDI} (eV)	δG_r (eV)	Position of TDTS	δG_{span} (eV)
Neutral	(5)/+1.10	(14)/-4.96	-4.47	before TDI	1.59
Basic	(5)/0.97	(1)/0.00	-4.92	after TDI	0.97

Reaction pathway in neutral environment on Au

- (1) $O_2(aq) + 2H_2O^* + CH_3CH_2OH(aq) + 4^* + 1/4(O_2 + 2H_2O)(aq)$
- (2) $(O_2 + 2H_2O)^* + CH_3CH_2OH^* + 3^* + OH^*$
- (3) $TS(OH + OOH + H_2O)^* + CH_3CH_2OH^* + 3^* + OH^*$
- (4) $(OH + OOH + H_2O)^* + CH_3CH_2OH^* + 3^* + OH^*$
- (5) $TS(OH + O + OH + H_2O)^* + CH_3CH_2OH^* + 3^* + OH^*$
- (6) $(OH + O + OH + H_2O)^* + CH_3CH_2OH^* + 3^* + OH^*$
- (7) $TS(4OH)^* + CH_3CH_2OH^* + 3^* + OH^*$
- (8) $(4OH)^* + CH_3CH_2OH^* + 3^* + OH^*$
- (9) $CH_3CH_2O^* + 3OH^* + H_2O^* + OH^*$
- (10) $TS(CH_3CHO + H_2O)^* + 3OH^* + H_2O^* + ^*$
- (11) $CH_3CHO^* + 3OH^* + 2H_2O^*$
- (12) $CH_3CHOOH^* + 2OH^* + 2H_2O^* + ^*$
- (13) $CH_3COOH^* + OH^* + 3H_2O^* + ^*$
- (14) $CH_3COO^* + 4H_2O^* + ^*$
- (15) $CH_3COOH^* + OH^* + 3H_2O^* + ^*$
- (16) $CH_3COOH(aq) + 2H_2O^* + H_2O(aq) + 4^* + 1/4O_2(aq) + 1/2H_2O(aq)$

* represents surface, molecules in brackets represent co-adsorbed molecules

Reaction pathway in basic environment on Au

- (1) $\text{OH}^-(\text{aq}) + \text{O}_2(\text{aq}) + 2\text{H}_2\text{O}^*_{\text{e}} + \text{CH}_3\text{CH}_2\text{OH}(\text{aq}) + 3^*_{\text{e}} + ^*$
- (2) $(\text{O}_2+2\text{H}_2\text{O})^*_{\text{e}} + \text{CH}_3\text{CH}_2\text{OH}^*_{\text{e}} + \text{OH}^*_{\text{e}} + 3^*_{\text{e}}$
- (3) $\text{TS}(\text{OH}+\text{OOH}+\text{H}_2\text{O})^*_{\text{e}} + \text{CH}_3\text{CH}_2\text{OH}^*_{\text{e}} + \text{OH}^*_{\text{e}} + 3^*_{\text{e}}$
- (4) $(\text{OH}+\text{OOH}+\text{H}_2\text{O})^*_{\text{e}} + \text{CH}_3\text{CH}_2\text{OH}^*_{\text{e}} + \text{OH}^*_{\text{e}} + 3^*_{\text{e}}$
- (5) $\text{TS}(\text{OH}+\text{O}+\text{OH}+\text{H}_2\text{O})^*_{\text{e}} + \text{CH}_3\text{CH}_2\text{OH}^*_{\text{e}} + \text{OH}^*_{\text{e}} + 3^*_{\text{e}}$
- (6) $(\text{OH}+\text{O}+\text{OH}+\text{H}_2\text{O})^*_{\text{e}} + \text{CH}_3\text{CH}_2\text{OH}^*_{\text{e}} + \text{OH}^*_{\text{e}} + 3^*_{\text{e}}$
- (7) $\text{TS}(4\text{OH})^*_{\text{e}} + \text{CH}_3\text{CH}_2\text{OH}^*_{\text{e}} + \text{OH}^*_{\text{e}} + 3^*_{\text{e}}$
- (8) $(4\text{OH})^*_{\text{e}} + \text{CH}_3\text{CH}_2\text{OH}^*_{\text{e}} + \text{OH}^*_{\text{e}} + 3^*_{\text{e}}$
- (9) $\text{CH}_3\text{CH}_2\text{O}^*_{\text{e}} + 3\text{OH}^*_{\text{e}} + \text{OH}^*_{\text{e}} + \text{H}_2\text{O}^*_{\text{e}}$
- (10) $\text{TS}(\text{CH}_3\text{CHO}+\text{H}_2\text{O})^*_{\text{e}} + 3\text{OH}^*_{\text{e}} + \text{H}_2\text{O}^*_{\text{e}} + ^*_{\text{e}}$
- (11) $\text{CH}_3\text{CHO}^*_{\text{e}} + 3\text{OH}^*_{\text{e}} + 2\text{H}_2\text{O}^*_{\text{e}}$
- (12) $\text{CH}_3\text{CHOOH}^*_{\text{e}} + 2\text{OH}^*_{\text{e}} + 2\text{H}_2\text{O}^*_{\text{e}} + ^*_{\text{e}}$
- (13) $\text{CH}_3\text{COOH}^*_{\text{e}} + 3\text{H}_2\text{O}^*_{\text{e}} + \text{OH}^*_{\text{e}} + ^*_{\text{e}}$
- (14) $\text{CH}_3\text{COO}^*_{\text{e}} + 4\text{H}_2\text{O}^*_{\text{e}} + ^*_{\text{e}}$
- (15) $\text{CH}_3\text{COO}^-(\text{aq}) + 2\text{H}_2\text{O}^*_{\text{e}} + 2\text{H}_2\text{O}(\text{aq}) + 3^*_{\text{e}} + ^*$

* represents neutral surface, $^*_{\text{e}}$ represents charged surface, molecules in brackets represent co-adsorbed molecules.

The reaction from state (1) to state (2) includes the adsorption of O_2 but also the co-adsorption of the two water molecules that were adsorbed separately in (1).

It is worth noting that the electron left by OH^- is removed by acetic acetate in basic environment. Although it is claimed by some researchers^{172,173} that the O_2 reduction in

water can remove the electrons, we found that the corresponding Gibbs reaction energy is strongly endergonic ($\text{O}_2 + 2 \text{H}_2\text{O} + 4\text{e}^- \rightarrow 4 \text{OH}^-$ $\Delta G = +4.21 \text{ eV}$).

Energy profile on Pt

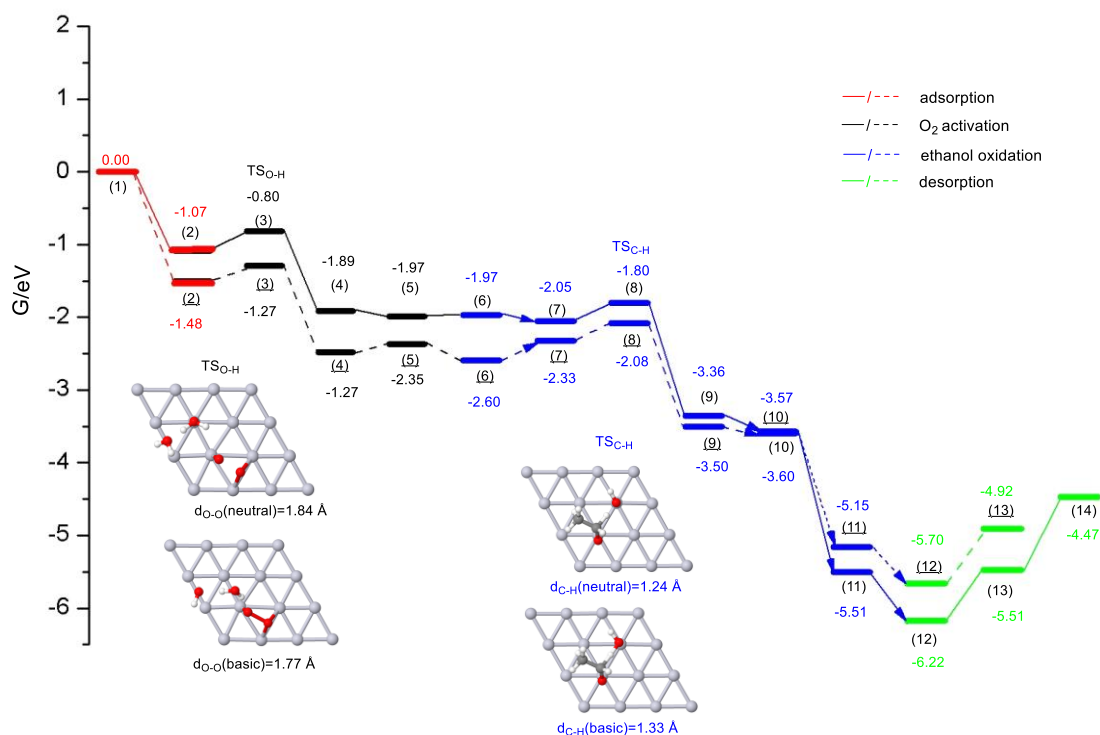


Figure A3.2.2 The whole pathway of alcohol oxidation from adsorption of reactants to desorption of products both in basic (dashed lines) and neutral (solid lines) environment, red represents adsorption, black represents O_2 activation, blue represents alcohol oxidation and green represents desorption on Pt

Table A 3.2.8 Determining TDTS, TDI and energetic span on ethanol oxidation on Pt

Pt	TDTS/ G_{TDTS} (eV)	TDI/ G_{TDI} (eV)	δG_i (eV)	Position of TDTS	δG_{span} (eV)
Neutral	(14)/-4.47	(12)/-6.22	-4.47	after TDI	1.75
Basic	(13)/-4.92	(12)/-5.70	-5.92	after TDI	0.78

Reaction pathway in neutral environment on Pt

- (1) $O_2 + 2H_2O^* + CH_3CH_2OH + 4^* + 1/4(O_2 + 2H_2O)$
- (2) $(O_2 + 2H_2O)^*_e + CH_3CH_2OH^*_e + 3^*_e + OH^*_e$
- (3) $TS(O + O + 2H_2O)^*_e + CH_3CH_2OH^*_e + 3^*_e + OH^*_e$
- (4) $(O + O + 2H_2O)^*_e + CH_3CH_2OH^*_e + 3^*_e + OH^*_e$
- (5) $(OH + O + OH + H_2O)^*_e + CH_3CH_2OH^*_e + 3^*_e + OH^*_e$
- (6) $(4OH)^*_e + CH_3CH_2OH^*_e + 3^*_e + OH^*_e$
- (7) $CH_3CH_2O^* + 3OH^* + H_2O^* + OH^*$
- (8) $TS(CH_3CHO + H_2O)^* + 3OH^* + H_2O^* + ^*$
- (9) $CH_3CHO^* + 3OH^* + 2H_2O^*$
- (10) $CH_3CHOOH^* + 2OH^* + 2H_2O^* + ^*$
- (11) $CH_3COOH^* + OH^* + 3H_2O^* + ^*$
- (12) $CH_3COO^* + 4H_2O^* + ^*$
- (13) $CH_3COOH^* + OH^* + 3H_2O^* + ^*$
- (14) $CH_3COOH + 2H_2O^* + H_2O + 4^* + 1/4O_2 + 1/2H_2O$

* represents surface, molecules in brackets represent co-adsorbed molecules

Reaction pathway in basic environment on Pt

- (1) $\text{OH}^- + \text{O}_2 + 2\text{H}_2\text{O}^*_{\text{e}} + \text{CH}_3\text{CH}_2\text{OH} + 3^*_{\text{e}} + ^*$
- (2) $(\text{O}_2 + 2\text{H}_2\text{O})^*_{\text{e}} + \text{CH}_3\text{CH}_2\text{OH}^*_{\text{e}} + 3^*_{\text{e}} + \text{OH}^*_{\text{e}}$
- (3) $\text{TS}(\text{O} + \text{O} + 2\text{H}_2\text{O})^*_{\text{e}} + \text{CH}_3\text{CH}_2\text{OH}^*_{\text{e}} + 3^*_{\text{e}} + \text{OH}^*_{\text{e}}$
- (4) $(\text{O} + \text{O} + 2\text{H}_2\text{O})^*_{\text{e}} + \text{CH}_3\text{CH}_2\text{OH}^*_{\text{e}} + 3^*_{\text{e}} + \text{OH}^*_{\text{e}}$
- (5) $(\text{OH} + \text{O} + \text{OH} + \text{H}_2\text{O})^*_{\text{e}} + \text{CH}_3\text{CH}_2\text{OH}^*_{\text{e}} + 3^*_{\text{e}} + \text{OH}^*_{\text{e}}$
- (6) $(4\text{OH})^*_{\text{e}} + \text{CH}_3\text{CH}_2\text{OH}^*_{\text{e}} + 3^*_{\text{e}} + \text{OH}^*_{\text{e}}$
- (7) $\text{CH}_3\text{CH}_2\text{O}^*_{\text{e}} + 3\text{OH}^*_{\text{e}} + \text{OH}^*_{\text{e}} + \text{H}_2\text{O}^*_{\text{e}}$
- (8) $\text{TS}(\text{CH}_3\text{CHO} + \text{H}_2\text{O})^*_{\text{e}} + 3\text{OH}^*_{\text{e}} + \text{H}_2\text{O}^*_{\text{e}} + ^*_{\text{e}}$
- (9) $\text{CH}_3\text{CHO}^*_{\text{e}} + 3\text{OH}^*_{\text{e}} + 2\text{H}_2\text{O}^*_{\text{e}}$
- (10) $\text{CH}_3\text{CHOOH}^*_{\text{e}} + 2\text{OH}^*_{\text{e}} + 2\text{H}_2\text{O}^*_{\text{e}} + ^*_{\text{e}}$
- (11) $\text{CH}_3\text{COOH}^*_{\text{e}} + 3\text{H}_2\text{O}^*_{\text{e}} + \text{OH}^*_{\text{e}} + ^*_{\text{e}}$
- (12) $\text{CH}_3\text{COO}^*_{\text{e}} + 4\text{H}_2\text{O}^*_{\text{e}} + ^*_{\text{e}}$
- (13) $\text{CH}_3\text{COO}^- + 2\text{H}_2\text{O}^*_{\text{e}} + 2\text{H}_2\text{O} + 3^*_{\text{e}} + ^*$

(* represents neutral surface, $^*_{\text{e}}$ represents charged surface, molecules in brackets represent co-adsorbed molecules)

The reaction from state (1) to state (2) includes the adsorption of O_2 but also the co-adsorption of the two water molecules that were adsorbed separately in (1).

3.3 AuCu/CeO₂ bimetallic catalysts for the selective oxidation of fatty alcohol (in collaborate with our experimental co-operator Marc Pera-Titus in Solvay China)

3.3.1 Introduction

Alcohol ether carboxylic acids (AECAs) are widely used as nonionic surfactants in the oil and gas, home and personal care and industrial formulations because of their low viscosity, high foaming capacity and low harm to eyes and skin^{174,175}. As of today, the main industrial route for AECA production proceeds via carboxymethylation using chloroacetic acid (i.e. Williamson's ether synthesis)¹⁸. However, this route is seriously questioned due to the use of excess amounts of toxic chloroacetic acid and the generation of sodium chloride as byproduct. As an alternative, nitroxyl radicals such as TEMPO can be used as catalysts for AECA production by the oxidation of alcohol ethoxylates (AEOs) with O₂ and nitric acid¹⁷⁶. Besides the use of highly corrosive nitric acid, this route suffers from low selectivity towards AECAs, encompassing the formation of large amounts of aldehydes and esters.

As a greener alternative, noble metal catalysts are often regarded as a good option for the direct oxidation of AEOs to AECAs in aqueous, alkaline medium (pH 9-11), using either O₂ or H₂O₂, affording water as main byproduct¹⁷⁷. Au nanoparticles have shown promise for catalyzing alcohol oxidation using O₂ and H₂O₂ as oxidants in the presence of a base.

Alloying is commonly regarded as a useful strategy for conditioning the activity of metal-supported catalysts. As a rule, the promoting effect of alloys on the catalytic activity can be rationalized by two main aspects¹⁴⁹: (1) a ligand effect, and (2) an ensemble effect. On the one hand, the ligand effect describes the change of chemical properties such as charge transfer between the different metals, orbital rehybridization and lattice strain¹⁷⁸. On the other hand, the ensemble effect describes the change of the

chemical composition, which alters the catalytic properties by providing different adsorption and active sites on the metal surface¹⁴⁹. Such effects can be used for designing surface and bulk alloys based in Au for conducting oxidation reactions. The addition of a second metal (e.g., Pd and Pt) is known to enhance the catalytic activity and stability of Au nanoparticles. In particular, the genesis of Pd monomers isolated by Au atoms on Pd-Au alloys can exert a considerable effect on the catalyst activity and selectivity for methanol and glycerol oxidation¹⁷⁹. The role of isolated atoms was also studied in formic acid decomposition catalyzed by a Ni-Au alloy. The authors found that isolated Ni destabilized the HCOO bidentate intermediate compared to pure Ni, decreasing the possibility of poisoning by HCOO species. This study illustrates the importance of isolated atoms with a catalytic role driven by the ensemble effect brought by Ni-Au sites¹⁸⁰.

In the choosing of the second metal, it is found that the particle size, shape, crystal structure and electronic properties of Au nanoparticles can be conditioned to an important extent by doping with Cu¹⁸¹. Supported Au-Cu catalysts have shown high activity, selectivity and stability against sintering in CO oxidation^{182,183}, and in liquid-phase aerobic oxidation reactions with special emphasis on biobased reagents (e.g., 5-hydroxymethylfurfural, HMF)^{38-40,117}. And the promoting effect of Cu on Au catalysts for CO oxidation in the presence of O₂ has also been confirmed by DFT calculations^{184,185}, which gives us a good reason of using Cu as the second metal in the catalysts.

The mechanism of the alcohol oxidation on pure Au has been studied theoretically in Chapter 3.2 on ethanol oxidation catalyzed by Au and Pt. Few theoretical studies focused on AuCu alloy, but the study on methanol oxidation catalyzed by AuPd bimetallic catalysts shows the similar mechanism found on the pure metals we mentioned before¹²¹. The mechanistic study gives us a principal idea of the AEO oxidation on AuCu alloy.

In our study, AEO7 was catalyzed to AECA6 catalyzed by different ratios of AuCu alloy supported by nanoceria in basic environment, using H₂O₂ as the oxidant. Then DFT calculations were done to unravel the advantages of the alloy compared to the pure metal catalysts.

3.3.2 Computational details

The optimal conventional cell parameter for Au and Cu were computed at 4.14 Å and 3.62 Å respectively, in excellent agreement with experimental data for Cu (3.62 Å) and reasonable agreement for Au (4.08 Å). Those parameters were used to build Au and Cu slabs. The slabs of surface Au-Cu alloys were built using the Au parameter. Considering that the (111) surface is the most exposed facet by the supported nanoparticles, Au(111) and Cu(111) were chosen to model the Au and Cu catalysts. Other computational details can be found in section 3.2.2.

3.3.3 Experimental results

All the experiments were performed at 80 °C for 16 h. A feedstock of 33 wt% AEO7 in water, AEO7/metal = 432 (mol/mol), H₂O₂/AEO7 = 6.4 (mol/mol) was used with the addition of H₂O₂ during 10 h.

Under the reaction condition above, the performance of pure Au, pure Cu and AuCu (Au:Cu=1:0.1) alloy in catalyzing AEO7 oxidation have been studied. Except the inactive catalyst pure Cu, both pure Au and the alloy displayed a similar performance with the AEO6 selectivity to AECA higher than 90%. However, the alloy shows a much better performance in the yield, 76% on alloy and only 50% on Au, and in turn over frequency (TOF), 366 mol AECA6/mol Au on alloy and only 180 mol AECA6/mol Au on Au. Here, the alloy catalyst shows a much better activity compared to the pure metal catalysts. To optimize the Cu loading, the AuCu alloy catalysts over nanoceria with a nominal Cu content in the range $x = 0.01-1$ wt% has been tested in performing the AEO7 oxidation as shown in [Figure 3.2](#).

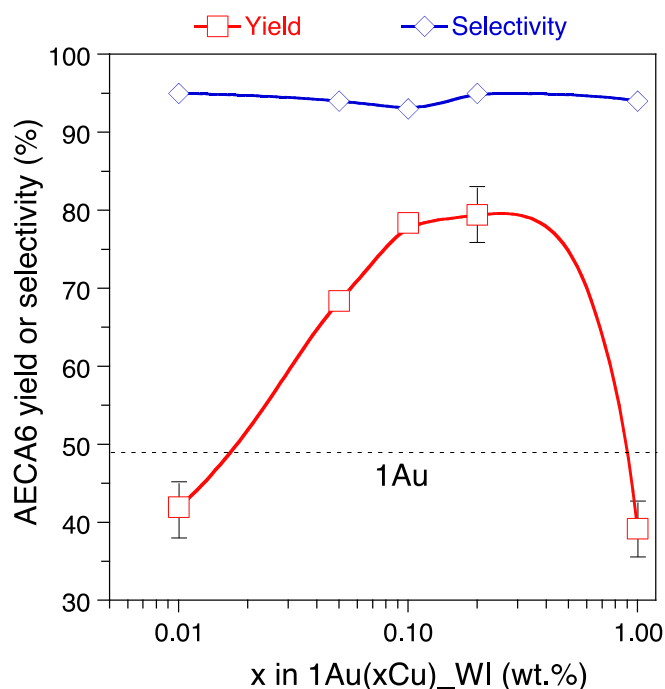


Figure 3.2 Effect of the Cu loading on the catalytic properties of 1Au(xCu)_WI formulations for AECA6 oxidation. Reaction conditions: 80 °C, 16 h, 33 wt% AEO7 in water, AEO7/metal = 432 (mol/mol), H₂O₂/AEO7 = 6.4 (mol/mol), H₂O₂ addition during 10 h, where WI represents the wet impregnation method of synthesizing alloy

The AECA6 yield shows a slight decline using 0.01 wt% Cu compared to the yield measured on the pure Au (from 49% to by 42%), whereas the AECA6 selectivity keeps almost unchanged at 95%. The AECA6 yield increases dramatically with the Cu loading in the range 0.01-0.20 wt% Cu until a maximum value of 80% for 1Au(0.2Cu) at an AECA6 selectivity of 93%, whereas it decreases further at higher Cu loading until 39% at 1wt%Cu, being lower than the yield obtained on pure Au. The best Au:Cu ratio is 1:0.01 and 1:0.02 with a TON of 336 and 343 mol AECA6 / mol Au, respectively, after 16 h.

The AuCu ratio of the bulk and the surface was also carefully check. Since the Au nanoparticles are very small (about 2 nm), we are unable to discern between bulk and surface alloys. Notwithstanding this fact, we can safely assume that the (Cu/Au) surface ratio of the 1Au(0.1Cu) can fall into the range 0.15-1.0. This range was computed from

the bulk (Cu/Au)=0.310 (ICP-AES) and surface (Cu/Au) (XPS) molar ratios corrected by the percentage of Cu on Au nanoparticles measured by STEM-EDX-SDD (50%). In light of these results, we built different Au-Cu surfaces and conducted a complete DFT study to rationalize the promoting effect of Cu on the catalytic activity of 1Au(0.1Cu) for the oxidation of ethoxylated alcohols.

3.3.4 DFT Results

3.3.4.1 Modelling the Au-Cu surface

Under the premise of low Cu on the Au surface, two general forms of Au-Cu alloy were modeled: (1) mono alloy, which represents a single Cu atom surrounded by Au, where one Au atom of the Au surface is substituted by one Cu atom; and (2) dimer alloy, which represents aggregated Cu in the Au alloy, where two neighboring Au atoms are exchanged by two Cu atoms. The configuration of both alloys is depicted in [Figure 3.3](#). As we mentioned in the experimental part, the bulk (Cu/Au) ratio for 1Au(0.1Cu) should be 0.31, so we chose a simplified pure Au bulk for our model. Hence, as mentioned in the computational details (section 2.5.1), we used the setting for Au, such as the cell parameter, the energy cut off and the Brillouin zone integration grid.

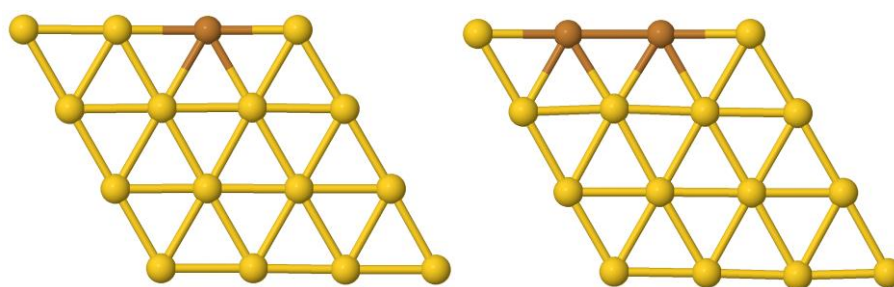


Figure 3.3 Mono alloy (left) and dimer alloy (right), yellow represents Au atoms and brown represents Cu atoms.

Then, we modeled the metallic surface in basic condition as a negatively charged surface. Using this model, we studied the complete oxidation path of AEO1, which was used as a model of AEO7, to acetate in basic environment (Eq (1)) on pure Au, pure Cu,

Au-Cu mono alloy and Au-Cu dimer alloy. In the following, AEO1 is expressed as AECH_2OH , while the corresponding aldehyde and acid are expressed as AECHO and AECOOH , respectively. Then, the overall reaction writes:



3.3.4.2 Catalytic cycle for AEO1 oxidation

The catalytic cycle for AEO1 oxidation with H_2O_2 is shown in Figure 3.4, whereas the corresponding Gibbs free energy profiles are plotted in Figure 3.8. In Figure 3.4, the basic environment is depicted as a grey rectangle charged by one electron indicated in blue. The structure of the reactants, products and intermediates on the different metals are represented in Figure A 3.3.2-Figure A 3.3.5. In these calculations, the reactants are in the aqueous phase, surrounded by a micro-solvation shell, which constitutes the reference state (1) in the Gibbs free energy profiles.

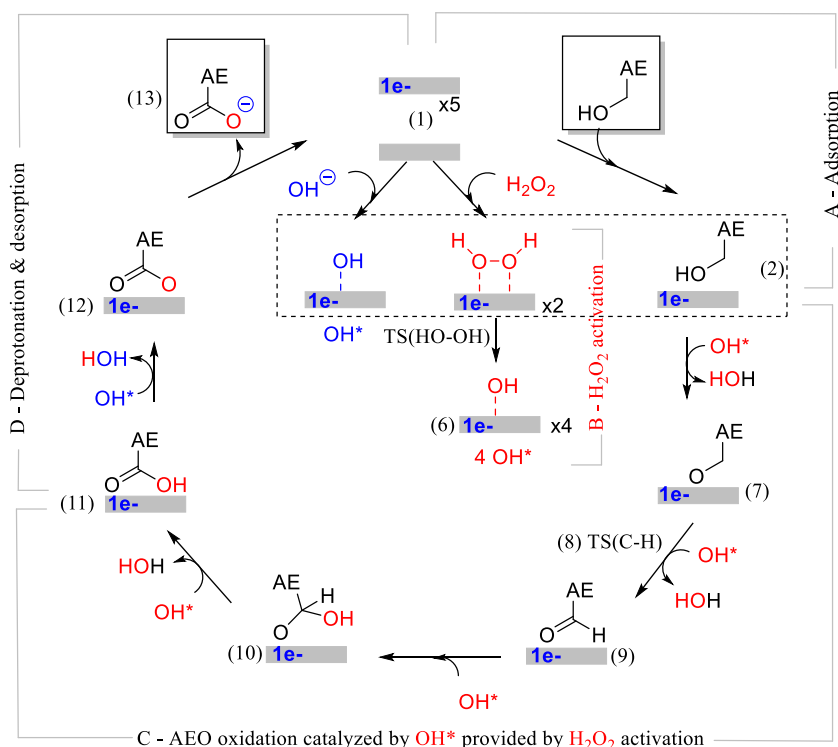


Figure 3.4 Catalytic cycle of AEO1 oxidation by hydroperoxide in presence of a base. The base (OH^- anion, shown in blue) polarizes the catalytic interface, a phenomenon that is taken into account in the modeling using

negatively charged metallic slab (one electron per surface exposed, shown in blue within a grey rectangular) with a counter charge described by a linearized Poisson-Boltzmann distribution of point charges. The split of two hydroperoxide molecules generates four surface hydroxyl that are the primary oxidants. Even if here they are labelled in red to trace them, surface hydroxyl can certainly exchange with the water solvent through the Grotthus mechanism. The resulting carboxylic acid AE₂COOH is further deprotonated by the last hydroxyl, generating AE₂COO that can desorb as a carboxylate anion, leaving a neutral, unpolarized surface behind.

To start, the alcohol and the two H₂O₂ molecules are chemisorbed on the negatively charged surface. In parallel, the OH⁻ is chemisorbed on a neutral surface, resulting in OH* (in blue) adsorbed on a negatively charged surface, resulting in state (2), named A-Adsorption. Then, we enter into the second stage (B), where H₂O₂* is cleaved to OH* (in red), from states (2) to (6). The OH* species can easily exchange with water through the Grotthus mechanism. This activation opens the door to the third stage (C), encompassing the alcohol oxidation from AECH₂OH* (7) to AE₂COOH* (11). The cycle closes up by the last stage (D) consisting of the deprotonation of AE₂COOH* into AE₂COO* (12) and its subsequent desorption into the water solvent under its anionic form, AE₂COO⁻ (13). Here, we first compare the different activities we obtained for the model catalysts on the four stages.

Adsorption

Table 3.2 Adsorption and desorption free energy of single molecule in basic environment at 80 °C

Catalyst	$\Delta G_{\text{ads}}(\text{kJ/mol})$			$\Delta G_{\text{des}}(\text{kJ/mol})$	
	AECH ₂ OH	OH ⁻	H ₂ O ₂	AE ₂ COO ⁻	H ₂ O
Au	22	6	17	30	-6
Cu	23	-30	13	51	-10
mono	8	-37	11	65	-8
dimer	2	-84	9	107	-8

Au and Cu show different properties when adsorbing OH⁻ on the neutral pristine (111) surface resulting into a OH* on a negatively charged surface (Table 3.2). On Cu,

OH^- is preferentially adsorbed at fcc sites with an adsorption energy of -30 kJ/mol, while on Au, OH^- is very weakly adsorbed on Au-Au bridge sites with an adsorption energy of 6 kJ/mol, which can be considered as a physical adsorption. On Au-Cu alloys, OH^- prefers to adsorb on Au-Cu or Cu-Cu bridge sites (-37 kJ/mol and -84 kJ/mol on the mono and dimer alloy respectively), demonstrating that Cu atoms in an Au matrix have specific properties especially in stabilizing the adsorbates.

As mentioned above, OH^- adsorption on metals results in partial charging of the surface, and the variable ability of metal surfaces to adsorb OH^- is expected to stem from their different capacity for accepting electrons. The charge density difference was calculated before and after the introduction of an electron from OH^- to explain the large difference in adsorption strength on Cu and Au as shown in **Figure 3.5**.

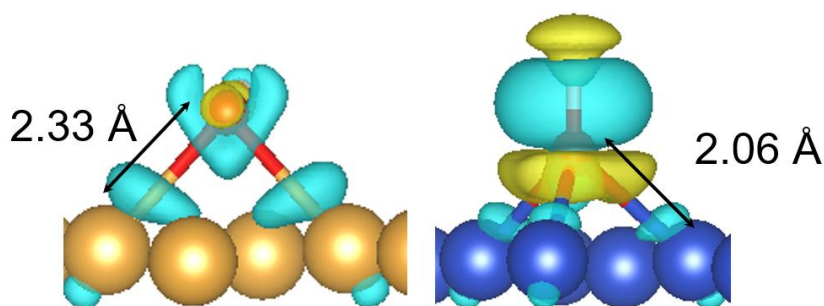


Figure 3.5 Charge density difference of OH^- adsorption on Au (left), Cu (right) with an isosurface value of 0.008 eV/bohr⁻³, yellow shows the accumulation of the electrons, light blue shows depletion of electrons.

After the adsorption of OH^- , no electron density accumulates around the Au-O bond, while the accumulation of electron density is found on Cu-O bond, which gives the explanation of the stronger adsorption on Cu. And we can also learn from the O_2 adsorption studied by Nørskov that the weak adsorption on Au may also come from the Pauli repulsion interaction between the valence states of O and the d band states of the Au, considering the 5d states from Au is more expanded than the 4d states from Cu, the repulsion interaction should be more obvious on Au which leads to the weaker adsorption¹⁸⁶. In alloys, the electron in Cu will transfer a bit to Au atoms, which decreases the electron density in the Cu 4d states and then decrease the repulsion interaction between Cu atoms and O atom, which contributes to the stabilization of the OH^- adsorption on alloy surface.

H_2O_2 adsorption energies and structures do not depend on the nature of the metal surface, while the adsorption of AECH_2OH is more sensitive. Alcohol adsorption is not favorable in all the cases and is the weakest on Cu while it is much stronger on the alloys, where surprisingly AECH_2OH prefers to adsorb on or near Cu atoms. It is worth noting that the alloys always adsorb the species involved in the reaction more strongly than the monometallic surfaces, especially OH^- and AECH_2OH , which may facilitate the reaction compared to the pure metals.

H_2O_2 activation

H_2O_2 is activated at the very beginning of the cycle to provide a source of OH^* . The activation of H_2O_2 is not difficult, especially on the alloy surfaces. The activation of a second H_2O_2 molecule is also required according to eq 13 to generate 4 OH^* in total and fulfill the oxidation of one AECH_2OH in the corresponding acid. We propose here to include that second activation readily after the first one, from (4) to (6). We also checked the situation when the second H_2O_2 molecule was activated after using the OH^* produced by OH^- and the first H_2O_2 , and we still obtained the same global barrier. The transition states of the HO-OH cleavage on different surfaces are shown in Figure 3.6.

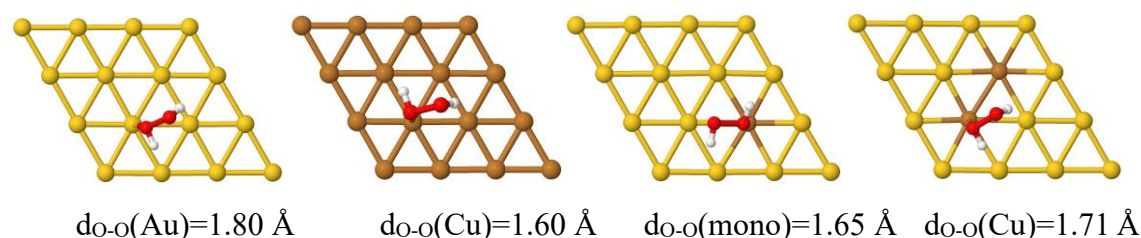


Figure 3.6 From left to right, transition state of HOOH cleavage on Au, Cu, mono and dimer alloy in basic environment.

The highest barrier is observed for Au (36 kJ/mol), along with the longest O-O bond in the TS (1.80 Å). When Cu is available in the alloy, H_2O_2 prefers to be adsorbed on Cu atom. The alloying Cu atom facilitates the dissociation of the adsorbed H_2O_2 (18 kJ/mol and 6 kJ/mol on mono and dimer alloys, respectively) with a short O-O bond in the TS (1.65 Å on mono alloy, 1.71 Å on dimer alloy). Last but not least, H_2O_2 dissociation is also quite easy on pure Cu (10 kJ/mol) with an even shorter O-O bond in the TS (1.60

Å).

AEO oxidation

With the help of the OH^* as a proton acceptor, the oxidation first goes through an O-H cleavage pathway from AECH_2OH^* (6) to AECH_2O^* (7) in a non-activated process (no TS could be located), followed by α -C-H cleavage from AECH_2O^* (7) to AECHO^* (9). The α -C-H cleavage is still quite easy on Au with $^*\text{OH}$ as a proton acceptor, with a small barrier of 35 kJ/mol (from other calculations they obtain a C-H cleavage barrier in the range of 12kJ/mol \sim 64 kJ/mol on ethanol^{88,106}). However, the barrier to overcome becomes larger when AECH_2OH^* reacts on Cu (114 kJ/mol) (a close barrier of 159 kJ/mol found by Zuo et. al. in ethanol oxidation¹⁸⁷) or on the alloys (61 kJ/mol on mono alloy and 127 kJ/mol on dimer alloy, respectively).

As mentioned above, the Cu sites in Au play the special role of stabilizing the adsorbates, which can explain the high barrier for the α -C-H cleavage on the alloys, especially on the dimer as is shown from step (6) to step (8) in **Figure 3.4**. The overstabilization of step (6) mainly comes from the stable OH^* species which displays an fcc configuration upon two Cu atoms as shown in **Figure 3.7**.

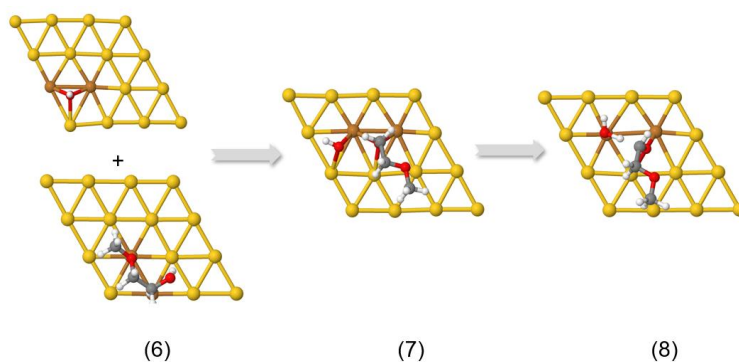


Figure 3.7 Reaction process from AEO to the α -CH cleavage

As shown in **Figure 3.7**, the stability of OH^* species in stage (6) causes difficulties when the OH^* is needed to be brought close to AECH_2OH for the following reaction which starts from stage (7). After the generation of the aldehyde AECHO^* from AECH_2O^* with OH^* , this step is followed by the addition of OH^* , generating

AECHOOH* (10) as an unstable intermediate, which quickly reacts with the fourth OH* to yield the acid AECO₂H* (11).

Deprotonation and desorption

In a basic and oxidative environment, AECO₂H* is not stable on the surface and will react with another OH* to generate AECO₂O*. In basic aqueous environment, the desorbed molecule is AECO₂O⁻ rather than AECO₂H. The same desorption pathway occurs for ethanol oxidation to acetic acid catalyzed by Au or Pt in basic environment, where acetic acid is easily deprotonated to acetic acetate, which further desorbs into the solvent. **Table 3.2** lists the desorption energies of AECO₂O* and H₂O*. AECO₂O* desorption from the metal surface to AECO₂O⁻ into the bulk solvent is somehow difficult for pure Cu and the Au-Cu alloys, but it is easier for Au. This is in line with the observed weaker HO⁻ adsorption on Au compared to the other surfaces (*vide supra*). Likewise, the adsorption of the other anions is not favored on Au, but is relatively favored on Cu and on the Au-Cu alloys. Also, as shown in **Figure A 3.3.2-Figure A 3.3.5**, the most stable structure of AECO₂O* on Au and on the alloys displays -CH₃ pointing to the metal surface, allowing a stronger interaction with the surface. In contrast, on Cu, the tail -CH₃ of AECO₂O⁻ is pushed far away from the surface. Last, H₂O* desorption is not sensitive to the nature of the metal surface and is exothermic for all metals and alloys.

Overall Pathway: Implications for AEO1 oxidation

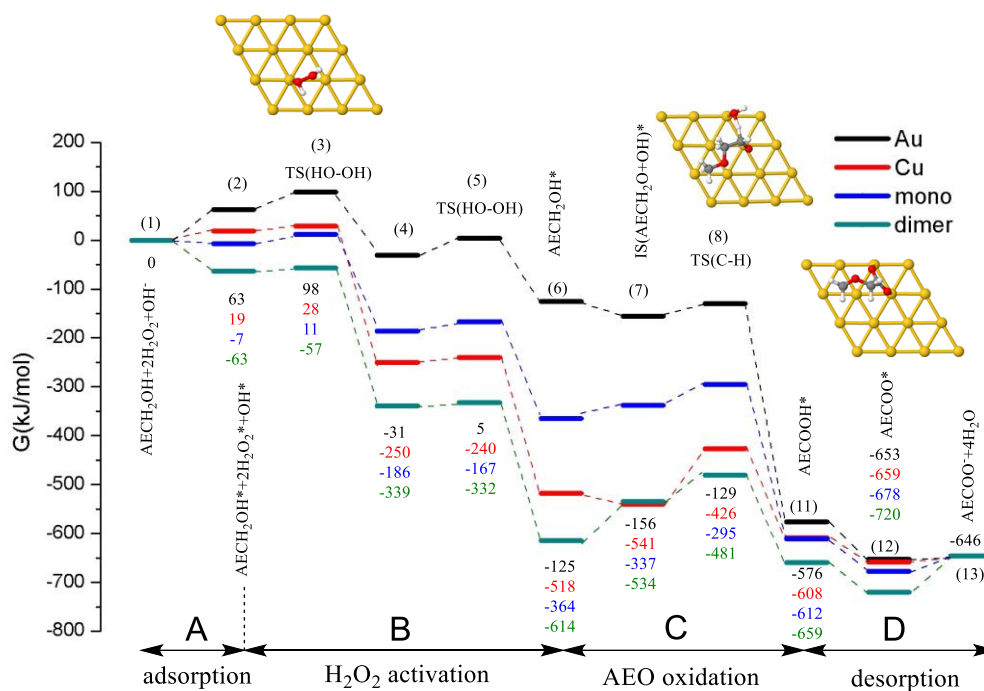


Figure 3.8 Free energy profile (G in kJ/mol) for AEO oxidation in basic environment at 80 °C catalyzed by Au (black line), Cu (red line), mono alloy (blue line) and dimer alloy (green line). To better represent the molecules, AEO1 is written as AECH₂OH here. Four main steps are shown as A (adsorption), B (H₂O₂ activation), C (AEO oxidation) and D (desorption).

Table 3.3 Barriers of every important steps ($\Delta G(A)$, $\Delta G(B)$, $\Delta G(C)$ and $\Delta G(D)$), energetic span (G_{δ}), reaction free energy (G_r), rate determining intermediate (TDI) and rate determining step (TDTS) of the whole AEO oxidation reaction on catalyzed by Au, Cu, mono alloy and dimer alloy in basic environment at 80 °C, all the results are shown in kJ/mol.

Catalyst	$\Delta G(A)^*$	$\Delta G(B)^*$	$\Delta G(C)^*$	$\Delta G(D)^*$	G_{δ}	G_r	TDI	TDTS
Au	63	36	27	6	105		(12)AECCO*	HOOH cleavage
Cu	19	10	114	12	114	-646	(AECH ₂ O+OH)*	α -C-H cleavage
mono	no	18	60	31	70		AECH ₂ OH*	α -C-H cleavage
dimer	no	6	134	73	134		AECH ₂ OH*	α -C-H cleavage

* $\Delta G(A)$ is the adsorption barrier refers to the initial state where all the molecules in solution; $\Delta G(B)$ is the H₂O₂ activation barrier of $G[\text{TS}(\text{HO-OH})^*] - G[\text{H}_2\text{O}_2^*]$; $\Delta G(C)$ is $G[\text{TS}(\text{C-H})] - G[\text{IS}(\text{AECH}_2\text{OH}+\text{H}_2\text{O})^*]$; $\Delta G(D)$ is the desorption barrier refers to AECCO*.

We collected the main barriers and energetic spans, as well as the rate determining

intermediate and transition state for each model catalytic surface (Figure 3.8, Table 3.3). The energetic span is very large on pure Cu (114 kJ/mol) (with a rate determining step of α -C-H cleavage and a rate determining intermediate of AECH₂OH*), but substantially smaller on pure Au (105 kJ/mol) (with a rate determining step of H₂O₂ cleavage and a rate determining intermediate of AECCO*) as the α -C-H cleavage is much easier with only a barrier of 35 kJ/mol, while the adsorption of molecules and the H₂O₂ cleavage are still the most difficult on Au compared to other metals, thus the energetic span on Au is still a bit high. For alloys, the rate-determining transition state is always α -C-H cleavage, whereas the rate determining intermediate is the preceding state, namely the adsorbed AECH₂OH. For the dimer alloy, the energetic span (133 kJ/mol) is the largest but for the mono alloy it is strongly reduced (70 kJ/mol). The large difference of the energetic span between mono and dimer alloy mainly comes from the α -C-H cleavage, where on dimer alloy, AECH₂OH* is much more stable than it is on mono alloy as we mentioned in the AEO oxidation part. It implies that the adsorption of OH* on Cu atoms is so stable that may poison the surface. Hence it can be concluded that isolated Cu sites on the Au surface show strongly enhanced reactivity due to the ensemble effect. The predicted catalytic activity for complete AECH₂OH oxidation is consistent with the experimental results as we mentioned in the experimental part: pure Cu is found inactive, Au shows moderate activity, and alloys with lower Cu: Au ratios perform best.

Also, in line with the study reported by Liu *et al.*¹⁸⁸, the presence of a large concentration of Cu atoms in the AuCu alloy leads to a surface completely covered by Cu atoms. This is expected to reduce the exposure of Au atoms on the alloy surface and accordingly the presence of Cu sites isolated in an Au matrix, affecting negatively AEO oxidation, especially α -CH cleavage. Overall, the promoting effect of Cu in the alloys can be rationalized as follows: (i) isolated Cu site in Au favors the adsorption of the reactants compared to pure metals, and (ii) isolated Cu site in Au lowers the barrier for H₂O₂ cleavage compared to pure metals. Since the mono-alloy shows a lower energetic span than the dimer, isolated Cu sites are key for catalytic promotion, which explains the importance of the low ratio of Cu in Au alloy to observe experimentally a promotion of AEO oxidation. The main role of Au is to provide sites in the α -CH cleavage which largely decrease the C-H cleavage barrier compared to Cu. The main drawback of the dimer alloy or aggregated Cu atoms lies in that it easily over stabilizes adsorbates on the

surface, which is especially relevant in the case of AEO, leading to a much higher energy barrier.

Finally, we also performed calculations for AEO oxidation in neutral environment. **Table A3.3.1** and **Figure A 3.3.7** collect the main barriers and energetic span, as well as the rate determining intermediate and transition state for each surface. Under a neutral environment, no matter the thermodynamic or the kinetic point of view, all the catalysts are much less active, and the catalytic surfaces are easily to be poisoned by the deprotonated product AECOO species, resulting in an almost absence of reactivity matching the experimental observations. Accordingly, a base (OH^-) is necessary for catalyzing AEO oxidation.

3.3.5 Conclusion

A mechanism study was done on Au, Cu and AuCu alloy catalysts using DFT. Comparing the reactions both in basic and neutral environment, it was found that a basic environment is necessary in the AEO oxidation. In basic environment, Cu shows a poor ability in oxidizing AEO due to the difficulty in breaking the $\alpha\text{-C-H}$ bond. Compared to Cu, the $\alpha\text{-C-H}$ cleavage is quite easy on Au, thus the AEO oxidation can still proceed when catalyzed by Au. Then an Au atom is substituted by Cu to build the mono alloy catalysts and shows great ability in catalyzing AEO: (i) in the presence of Au atoms, the $\alpha\text{-C-H}$ cleavage is largely decreased compared to Cu; (ii) with the help of Cu, the H_2O_2 activation also becomes lower compared to Au. The aggregation effect of the Cu atoms was also tested here, and it is found that aggregated Cu sites can over stabilize the intermediates and leads to a large energy barrier. In conclusion, in the oxidation of AEO to AECA, isolated Cu atoms in alloy plays a critical role.

Appendix 3.3

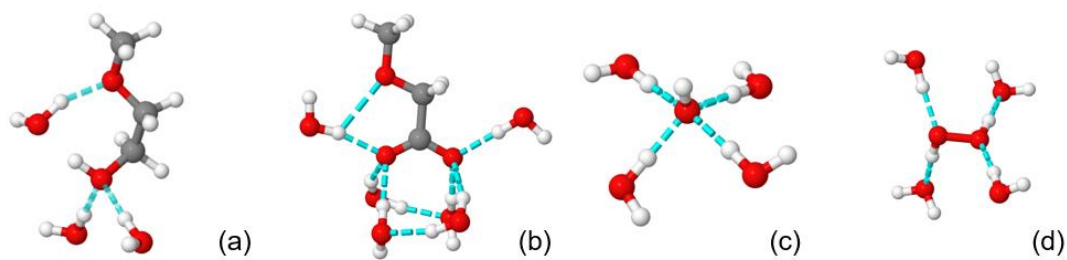


Figure A 3.3.1 Microsolvated (a)AECH₂OH, (b)AECOO⁻, (c)OH⁻ and (d)H₂O₂, light blue lines represent H bonds

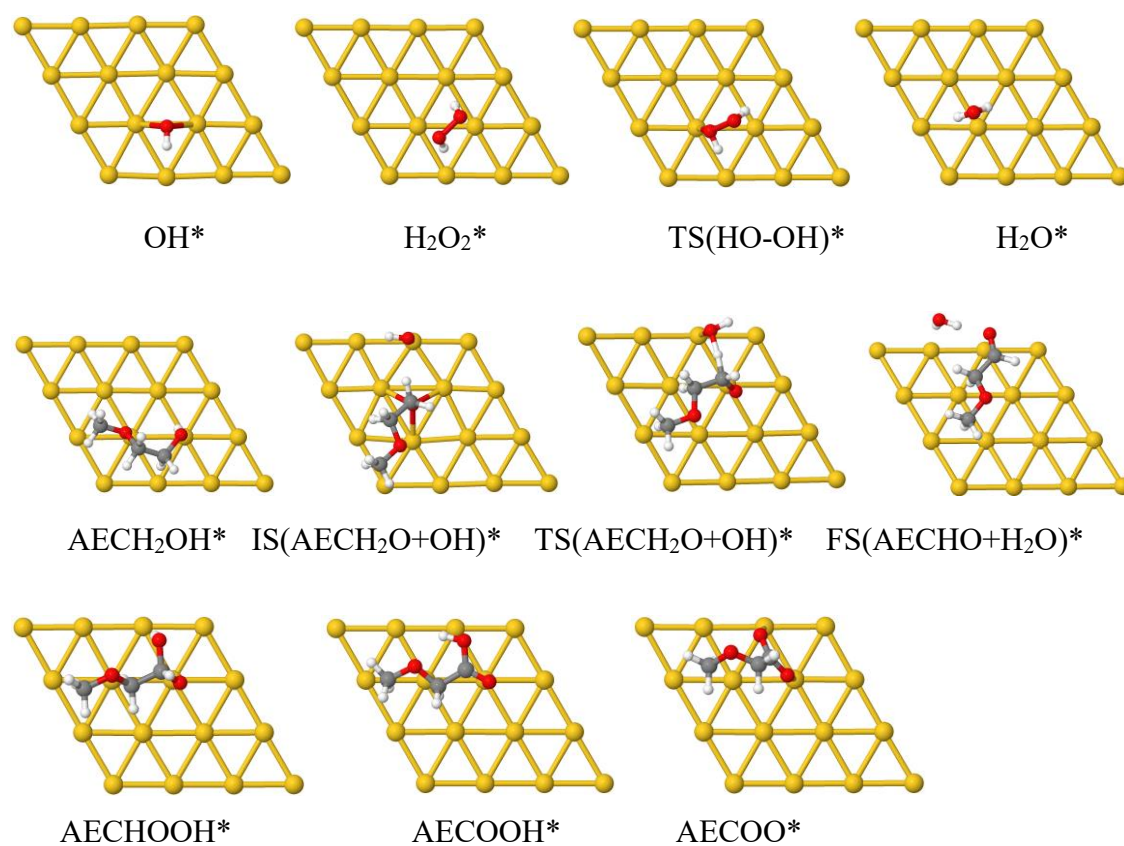


Figure A 3.3.2 Structures involved in AEO oxidation on Au in basic environment.

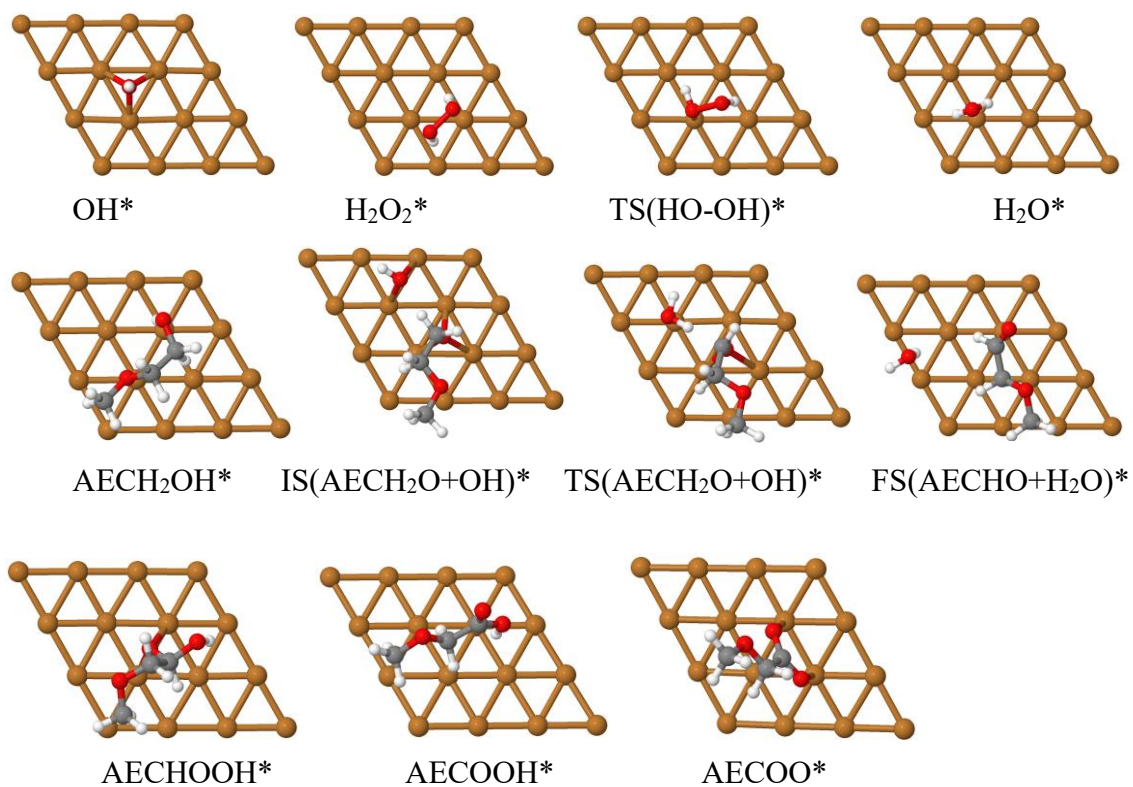


Figure A 3.3.3 Structures involved in AEO oxidation on Cu in basic environment.

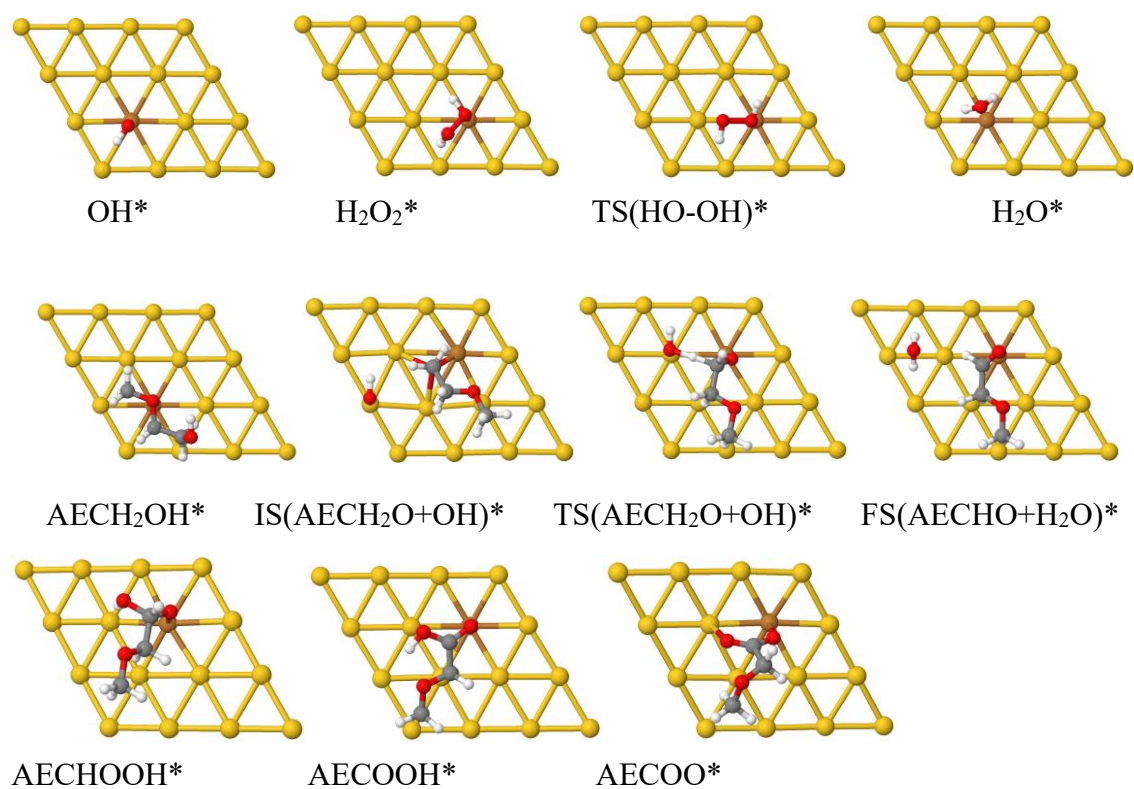


Figure A 3.3.4 Structures involved in AEO oxidation on mono alloy in basic environment.

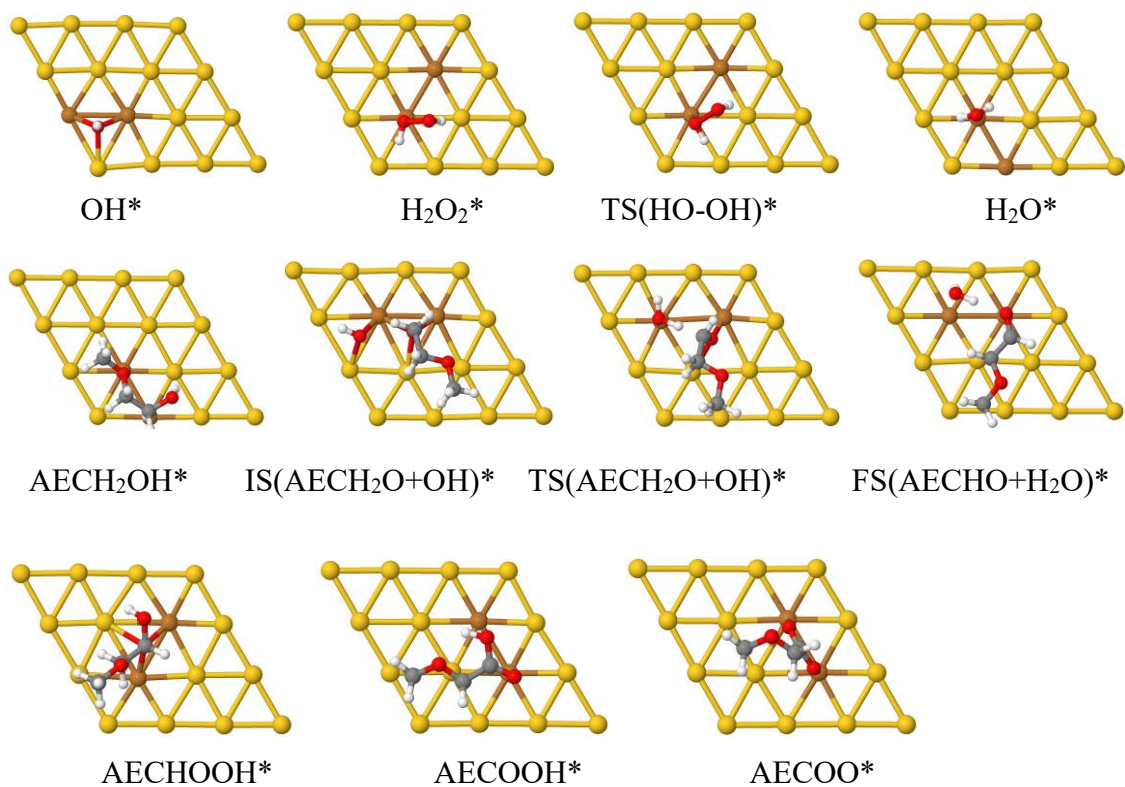


Figure A 3.3.5 Structures involved in AEO oxidation on dimer in basic environment.

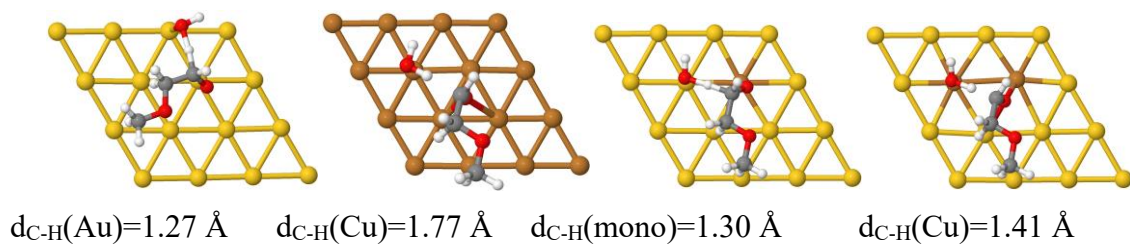


Figure A 3.3.6 Transition state of α -C-H cleavage from AECH₂O to AECHO on Au, Cu, mono and dimer alloy (from left to right) in basic environment.

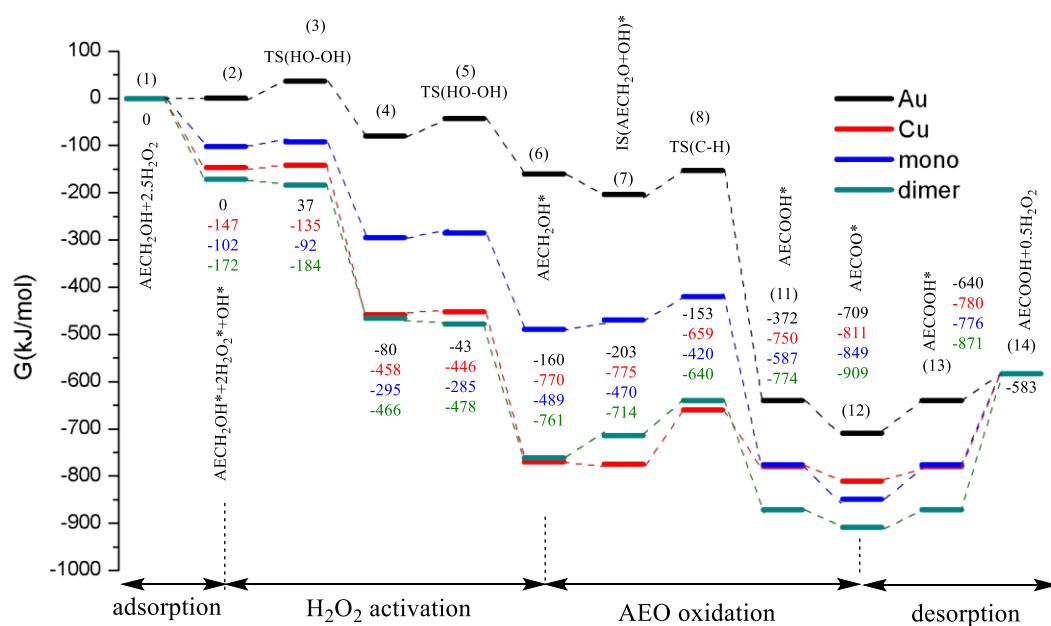


Figure A 3.3.7 Free energy profile of AEO oxidation at 80 °C catalyzed by Au (black line), Cu (red line) mono alloy (blue line) and dimer alloy (olive line) in neutral environment. To better represent the molecules, AEO1 is written as AECH₂OH here. Four main steps are shown as A (adsorption), B (H₂O₂ activation), C (AEO oxidation) and D (desorption).

Table A3.3.1 Barriers of most relevant steps G(A), G(B), G(C) and G(D), energetic span (G_{δ}), reaction free energy (G_r), rate determining intermediate (TDI) and rate determining step (TDTS) of the complete AEO oxidation reaction catalyzed by Au, Cu, mono alloy and dimer.

Catalyst	G(A)	G(B)	G(C)	G(D)	G_{δ}	G_r	TDI	TDTS
Au	0	37	50	126	163		AECOO*	HOOH cleavage
Cu	no	12	116	227	227	-583	AECOO*	desorption
mono	no	11	69	266	266		AECOO*	desorption
dimer	no	0	120	325	325		AECOO*	desorption

Chapter 4 Modeling dehydration reactions on metal phosphate catalysts

Considering the wide use of metal phosphates, more and more phosphate materials are studied, and learning from the existing natural phosphate structures, many new materials are constructed to have a better practicability and a novel application in our daily life.

For alkali metal phosphates (AMP), all the AMP are soluble in water, and the most substantial AMP are sodium and potassium. In agriculture, phosphates are one of the main nutritional ingredients for plants, including the water-soluble metal phosphates such as monocalcium phosphate ($\text{Ca}(\text{H}_2\text{PO}_4)_2$). In food industry, the soluble alkali-metal phosphates such as sodium phosphates ($\text{Na}_x\text{H}_{(3-x)}\text{PO}_4$) and potassium phosphates ($\text{K}_x\text{H}_{(3-x)}\text{PO}_4$) which are always used as food additives.

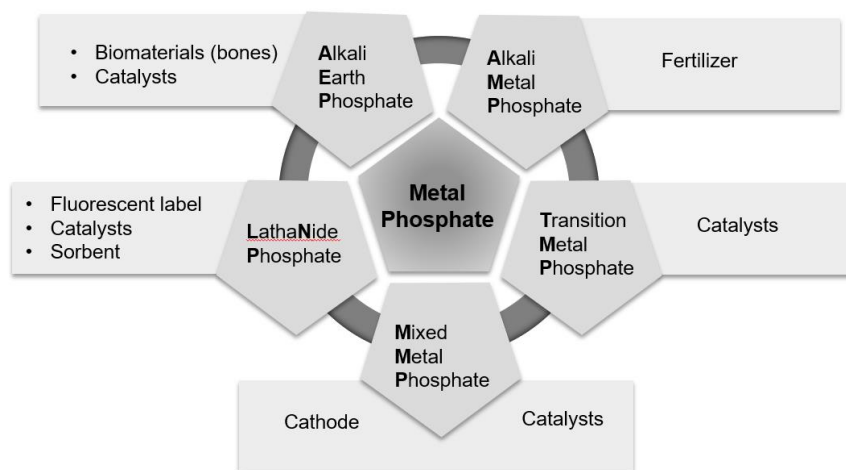
For alkali-earth phosphates (AEP), the most useful AEP is Calcium phosphates as we mentioned before. Calcium phosphates have a great biological and medical significance, such as in bones, in teeth, in shells and in some other hard tissues¹⁸⁹. Because of its importance as a biomaterial, more and more Calcium phosphates, especially HA materials are used in orthopaedic and trauma surgeries as solid ceramic, as self-setting cement, or as implant coating¹⁹⁰. Metal phosphates are ubiquitous and

indispensable materials in human life. In human body, around 1% body composition is phosphorus and it mainly exists in bones in the form of hydroxyapatite ($\text{Ca}_5(\text{PO}_4)_3(\text{OH})$, HA).

For transition metal phosphates (TMP), due to its easy functionalization of PO_4 and PO-H groups and the transition metal-containing mesoporous, TMP are normally superior catalysts for all kinds of chemical reactions. The most widely used vanadium phosphates are one of the TMP that have been commercialized in the oxidation of butane to maleic anhydride¹⁹¹. Zirconium and Titanium phosphates have already shown their great ability as catalysts in alcohol dehydration, oxidative dehydrogenation, partial or selective oxidation and polymerization reactions in 80s¹⁹².

For Lanthanide phosphates (LNP), from the clinical point of view, the LNP nanorods can be as inorganic fluorescent labels in cell¹⁹³; from the catalytical point of view, it works as a good catalyst such as in dehydration reactions¹⁹⁴⁻¹⁹⁶; and photocatalytic CO_2 reduction when deposited with Pt¹⁹⁷; thanks to the mesoporous structure, it can also be used as a novel sorbent¹⁹⁸.

For mixed metal phosphates (MMP), namely the metal phosphates doped or substituted with the second or even more metal ions, they may show more abundant using compared to the monometallic phosphates. Among all the MMP, the doping of Li in all kinds of metal phosphates takes large amount of the MMP field. Li_xMPO_4 materials have become some of the most promising cathode materials for rechargeable Li and Li-ion batteries¹⁹⁹, thanks to the mobility of the Li ions inside the materials. LiFePO_4 has now already been commercialized as the active cathode element of a new generation of lithium-ion batteries²⁰⁰. Wide using of MMP also lies in the catalytic field, where the additional metal normally plays an important role in providing acido-basic sites in the different catalytic reactions such as classic catalytic reactions²⁰¹, photocatalytic reactions²⁰² and electrocatalytic reactions²⁰³.



Scheme 4.1 Different kinds of metal phosphates and their functions

Metal phosphates used as catalysts in biomass reactions

As we mentioned in Chapter 1, biomass is becoming a more and more essential feedstock in building an environmentally friendly society. Metal phosphates have been studied a lot in the biomass reactions such as the direct conversion of cellulose substrates and lignocellulosic biomass²⁰⁴ and the dehydration of biomass derivatives such as carbohydrates^{204,205}.

To start the biomass reactions, the cleavage of the long chain biomass derivatives into short chain organic compounds is a necessity. The direct conversion from cellulose substrates, lignocellulosic biomass and sugarcane bagasse into HMF (5-hydroxymethylfurfural) was first detected in the research of Bhaumik in 2012²⁰⁴, with a yield of HMF around 20%. The reactions were performed under 413 K using the MTiP-1 (mesoporous titanium phosphates) catalyst in DMA (dimethylacetamide)–LiCl solvents. Thanks to the surface Lewis acidity and the high surface area of the MTiP-1 catalysts, Bhaumik also obtained good yields in some other short chain dehydration to HMF such as from biomass derived carbohydrates, fructose, glucose, mannose and sucrose.

The main difference between the biomass feedstock and the useful chemicals lies in

the length of the chain and the numbers of oxygen-contained functional groups on the chains. The idea is to (i) break the chains, as we mentioned before, the MTiP-1 catalysts play an important role. (ii) decrease the number of oxygens, which we will mainly discuss in this paragraph, by dehydrating the oxygen-abundant organics. One very important dehydration reaction is the HMF synthesis, which we also mentioned a bit in the above paragraph. Except using titanium catalysts, the synthesis of HMF from biomass derivatives can also be catalyzed by some other metal phosphates such as vanadium phosphate²⁰⁵, zirconium phosphates^{5,206}, manganese phosphates²⁰⁷ and some other transition metal phosphates^{208–210}. Another large branch of the biomass reactions lies in the short chain molecule glycerol which derives from triglycerides. Among the glycerol reactions, dehydration also takes an important role in the following fine chemical production. It is generally accepted that Brønsted acid sites are superior to Lewis acid sites for the selective conversion of glycerol into acrolein²⁰¹, which may come from the easy dehydration of the OH from glycerol and the H from the Brønsted acid sites on the surface. Many metal phosphates are effective in catalyzing glycerol dehydration reactions, such as vanadium phosphates²¹¹, zirconium phosphates²¹² and calcium phosphates²¹³. Another essential biomass derivative, isosorbide, is widely used in pharmaceutical compounds, cosmetics and products of food industry²¹⁴. The IV group metals show high selectivity to isosorbide with a moderate conversion in the sorbitol dehydration reaction²¹⁵. The dehydration of sorbitol is considered to have a strong relationship with the moderate and strong surface sites, and is favored by the large pores²¹⁶.

Besides the dehydration reactions that start from the very beginning of the biomass reactions, there exists many other types of chemical reactions catalyzed by MP especially from the glycerol, as is shown in **Figure 1.1**. Metal phosphates also play an important role in catalyzing oxidation reactions^{217,218}, hydrogenation reactions²¹⁹, decomposition reactions²²⁰ and pyrolysis reactions²²¹. However, we are facing many problems in the research of metal phosphates, especially the fundamental structural problem of the MP

catalysts. Under different reaction conditions, such as different temperatures, different pressures, different pH and different surrounding environments, the surface morphology will have some changes. A common but representative case is the hydration level of the surface, the water coverage changes a lot according to the changing of temperature and the pressure. Even under the same environment, the defects and amorphism properties of the surface also increase the uncertainty of the morphology. To understand well the reaction mechanism of the MP catalysts, it is necessary to know well about the surface structure through characterization and modeling methods.

Characterization of metal phosphates

To have a clear understanding of the catalytic structure, the TEM (Transmission electron microscope) measurement, XRD (X-ray diffraction) measurement and IR (infrared spectra) measurement are normally necessary. TEM can give us a direct-viewing impression of the morphology, we can also obtain the information of the size of the catalysts. XRD can provide an accurate crystalline structural information such as atom distribution and cell parameter. And for IR measurement, we can get the surface structural information by adsorbing different adsorbents. The TEM and XRD mainly provide us details on modeling the surface, while the IR provides more information related to the catalytic properties. Thus, in the following paragraph, IR measurements are mainly focused on.

The most important information IR gives should be the acido-basic properties of the catalysts. It can also give a more accurate view of the functional groups on the surface, and pave the way for the mechanism study in the following surface reactions. Aboulayt et. al²²² studied the relationship between phosphate structure and acid-base properties of phosphate-modified zirconia, which is the sufficient catalysts for the alcohol dehydration. Here the acidity was probed by 2,6-dimethylpyridine (lutidine, DMP) adsorption and the basic properties were probed using CO₂ adsorption. According to the results of Raman and IR spectroscopies, it shows that the formation of P₂O₄⁻⁷ surface species for low P

amount, whereas HPO_4^{2-} surface species become predominant at the highest P loadings.

Acido-basic properties of metal phosphates

MP catalysts are famous for its acido-basic properties in many catalytic reactions as section 4.1.1 mentioned. Normally the confirmation of the surface structure is accompanied by the probe of the acido-basic sites. To investigate the acid sites, an adsorption of NH_3 or pyridine is always performed. Take NH_3 as an example, for Lewis acid (LA) site, the lone pair from NH_3 will coordinate with the acid center, a characteristic peak around 3300 cm^{-1} and 1640 cm^{-1} will appear. For Bronsted acid (BA) sites, NH_3 will directly react with the H^+ from the BA center and generate NH_4^+ on the surface, which gives a characteristic peak around 3120 cm^{-1} and 1450 cm^{-1} . To investigate the basic sites, an adsorption of CO_2 or SO_2 is performed. Take CO_2 as an example, carbon dioxide is reported to adsorb on the basic site as a unidentate complex when the pressure of carbon dioxide is relatively high²²³. C_2H_2 adsorption is also widely used in probing a more complicated acido-basic pair as shown in Figure 4.1²²⁴.

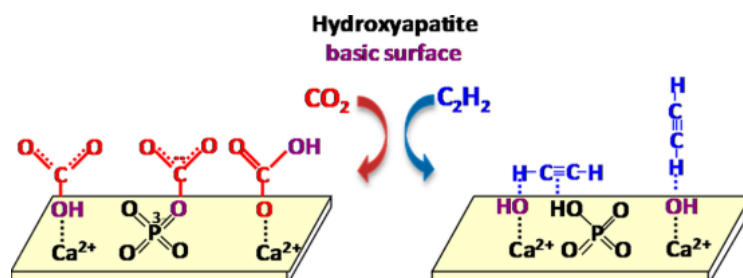


Figure 4.1 The acido-basic sites probing on hydroxyapatite by CO_2 and C_2H_2 adsorption reproduced from work of Diallo-garcia²²⁴

As shown in Figure 4.1, it is proposed that CO_2 interacts with basic OH^- and O_2^- of PO_4^{3-} groups to form hydrogen carbonates and surface carbonates, respectively. For the adsorption of C_2H_2 , an interaction between of acido-basic pair (POH-OH) is observed, and the most stable C_2H_2 adsorption on the basic OH^- can also be detected. The pre-determination of the acido-basic sites is significant for the following reaction mechanism

on the surface.

Modeling of metal phosphates

Based on the well performed characterization, we can obtain all the structural information for the modeling. Apatites are the most abundant phosphate materials in the world, and are also the most studied phosphate materials in theory. Different series of apatites can be represented as: (1) The most common fluorapatite $\text{Ca}_{10}(\text{PO}_4)_6\text{F}_2$ (the most common phosphate mineral which can be used as source of both phosphoric and hydrofluoric acids industrially); (2) The chlorapatite $\text{Ca}_{10}(\text{PO}_4)_6\text{Cl}_2$ (a common accessory mineral in layered mafic intrusions); (3) The hydroxyapatite $\text{Ca}_{10}(\text{PO}_4)_6(\text{OH})_2$ (the main composition of bone and enamel); (4) And the carbonate apatite $\text{Ca}_{10}(\text{PO}_4, \text{CO}_3, \text{OH})_6(\text{F}, \text{OH})_2$ (also exists in bone and enamel)²²⁵. Different monovalent anions (F^{-1} , Cl^{-1} , OH^{-1}) contribute to different apatites, hence lead to different applications.

Among all the apatites, hydroxyapatite (HA) attracts much attention for its wide using in bones and teeth as a biomaterial with applications in the repair both experimentally and theoretically²²⁶. Astala et. al.²²⁶ studied the low-index HA surfaces, including (001), (101) and (010) surfaces. In the modeling procedure of HA slabs, all the different surfaces are cut from the bulk in different directions. A stoichiometric structure is always kept to avoid the dipole in Z direction. Then a vacuum layer of 17 Å or more is added to separate the systems in Z direction and avoid the interaction between the slabs. The PO_4 and OH ions are left intact to avoid the breaking of the P-O and O-H bonds when cutting the surface. Above is the normal modeling procedure of a metal phosphate surface, and according to such a procedure, the structures of surfaces are modeled stoichiometricly in **Figure 4.2**, and the ion-rich cases are also taken into consideration.

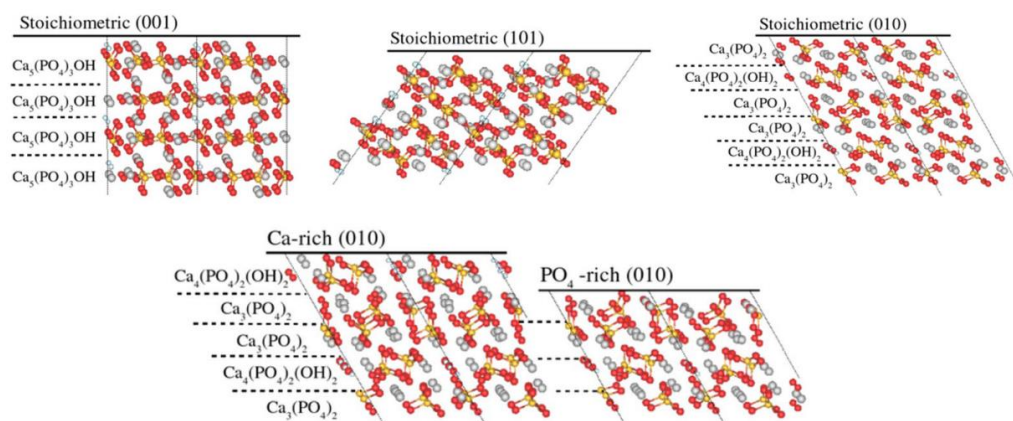


Figure 4.2 Side vies of low-index HA surfaces, Multiple unit cells of the periodic structure are shown. The tetrahedral groups are PO_4 ions, the large spheres are Ca atoms, and the small spheres are H atoms. The layered structure has been highlighted reproduced from work of Astala²²⁶

In Stott's study, the coverage of H_2O on the surface and the defective surface with Ca vacancies are also modeled. The (010) surface is found to be the most reactive surface when adsorbing waters. The defective surface, or we say the Ca vacancy is quite favorable on the stoichiometric (001) and Ca-rich (010) surfaces. This theoretical study shows clearly the importance of the environment, that the surface morphology depends much on the environment.

Lanthanide phosphates are becoming more and more attractive because of its protonic conduction and high-temperature chemical stability²²⁷. Many theoretical investigations are focused on its morphology controlling and growth^{228,229}, on the proton-transfer mechanism²²⁷, on phase transition under different pressures²³⁰ and electronic properties²³¹. The similar surface morphology controlling study as we mentioned in HA is also done in the LaPO_4 by Wang²²⁸ and Zhang²²⁹. They used different H concentration on the LaPO_4 surface to roughly represent different pH. By constructing the Wulff graph in different pH conditions, they related theoretical nanoparticle morphologies with those in experiments and obtained a good consistency, the surface structures and the corresponding Wulff graphs are shown in [Figure 4.3](#).

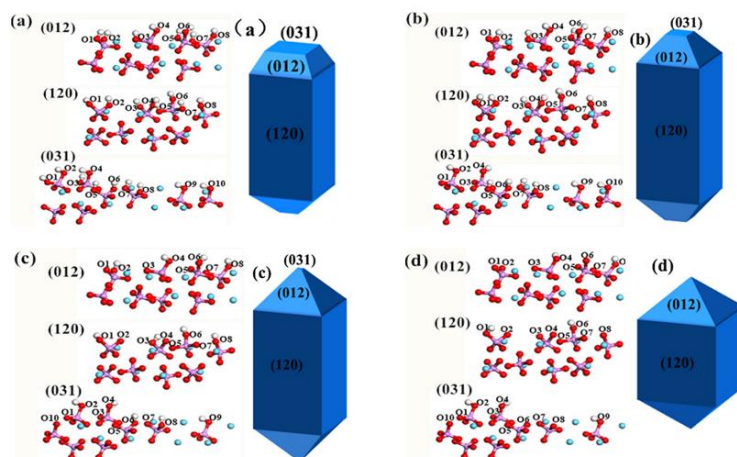


Figure 4.3 Surface structures of LaPO_4 under different pH conditions and its corresponding Wulff graph reproduced by work of Zhang²²⁹

To have a more accurate description of the catalytic surface and a closer relationship between the characterization and theoretical modeling of the surface structure, and also considering the IR study plays such an essential role in the surface material, especially the solid catalysts, more and more researchers are taking the IR spectra modeling as a necessity in their researches. A fine study on the Fourier transform infrared vibrational spectrum of Brushite ($\text{CaHPO}_4 \cdot 2\text{H}_2\text{O}$) is investigated both experimentally and theoretically²³². They built the Brushite bulk based on the neutron single crystal diffraction study²³³. Then they obtained the vibrational frequencies using the frozen phonon approach, and the corresponding peak intensities from the Born effective charge tensor. Here they compared the experimental and theoretical IR spectra of the Brushite, and found a good consistency of each important peak as shown in **Figure 4.4**, especially the vibration peaks of waters, which always remain to be a debate for their stretching and bending modes. Such an IR combination study gives us a more accurate structural information of Brushite and also gives us a clearer figure for future acido-basic sites conformation.

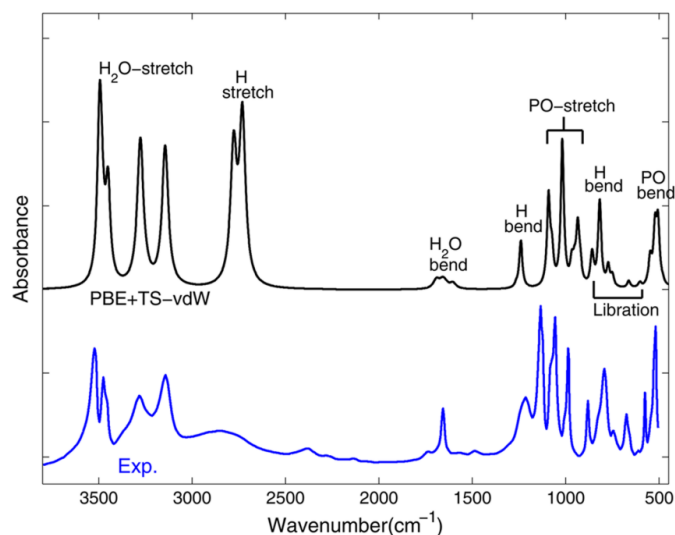


Figure 4.4 Comparison of the experimental (77 K) and calculated (PBE+TS-vdW) IR spectra. Assignment of the main vibrational modes is indicated on the calculated spectrum reproduced from work of Hirsch²³²

Then it comes to the difficulty in modeling, the simulation of the defective and the amorphous surface. Deficiency in material are inevitable, the commonest defects in a material is the vacancies of one or several atoms. In HA, a Ca/P molar ratio is often found to be in the range from 1.5 to 1.67 depending on the surrounding chemical and experimental environments, although it should be 1.67 according to its chemical formula, this shows there exists Ca^{2+} vacancies in HA²³⁴. And it has been considered from the 60s that the formula of the defective HA should be $\text{Ca}_{10-x}\text{H}_{2x}(\text{PO}_4)_6(\text{OH})_2$, i.e. protons will substitute Calcium ions²³⁵. Although the defects break the symmetry and stoichiometry of the lattice structure, the material itself still takes full advantage of the defects in all kinds of usages. The role of defects has also been studied experimentally and theoretically. Sleight et. al has already found the extended defects in VPO ($(\text{VO})_2\text{P}_2\text{O}_7$) catalysts is related to the catalytic properties, and the best ones are those where these defects are very prominent²³⁶. In a theoretical study, the defective VPO (100) surface with O vacancies is modeled, through the study on the electronic structure of this VPO surface, it shows that the located vacancies modify the electronic states of the nearby cation centers, in particular the high-coordinated vacancies yield an important reduction of the energy gap,

which enhances the activity and selectivity of VPO catalysts²³⁷. The stability properties of defects have also been studied by theory in the past few years. Wu et. al studied different kinds of point defects, including intrinsic Frenkel and vacancy defects, in CePO₄ using DFT²³⁸, and it was found the cerium defects are more difficult to form than the oxygen ions in monazite-Ce, well consistent with the experimental results for monazite-La.

The accurate modeling of amorphous materials is elusive no matter from the experimental or the theoretical point of view. Recently, a combination of classical molecular dynamic (MD) and DFT calculations to model the amorphous surface has been gradually used in the amorphous surface models such as amorphous silica surface²³⁹, ZnO amorphous surface²⁴⁰ and amorphous ternary phosphates²⁴¹. However, a simplicity of the amorphous surface, that taking one of the crystallized surfaces as the object to study, is still more widely used especially in surface catalytic surface reactions, as it can represent the proper properties of the amorphous surface in some degree.

4.2 Dehydration reaction of Lactic acid to acrylic acid on Calcium phosphates (in cooperation with Stéphane Loridant and Jean-Francois Paul)

4.2.1 Introduction

Acrylic Acid (AA) is a platform molecule used as a building block to produce acrylate polymers and plastics and currently produced by catalytic oxidation of propylene in large volume (6 Mt predicted by 2020)^{242,243}. From both environmental and economical point of view, alternative routes to produce acrylic acid should be developed. Glycerol, as the important chemical from biomass as we mentioned before, is a potential renewable raw material to produce acrylic acid by oxidehydration²⁴⁴. Yields higher than 50% were obtained on W-V-Nb mixed oxides with hexagonal tungsten bronze structure^{245,246}.

Another investigated route is the dehydration of Lactic Acid (LAA), a platform molecule used to produce chemical commodities and PLA polymers^{242,243,247}. Lactic acid is currently yielded by carbohydrates fermentation^{242,243,247} but can also be obtained by alternative fermentation processes using various substrates^{248,249} and by glycerol catalytic dehydrogenation²⁵⁰. The global market for lactic acid was 0.75 Mt in 2017 and is projected to reach 1,8 Mt by 2022²⁵¹. Modified zeolites, sulfates/nitrates, and phosphates were specifically investigated. The best yields were obtained using alkaline earth metal phosphates (up to 85 % AA yield) which furthermore are more stable than zeolites^{242,243,247}.

From the theoretical point of view, the mostly modeled alkaline metal phosphate catalyst is the calcium phosphate especially the hydroxyapatites due to its important using in biomaterials. However, considering the unique behavior of CaHAP in catalyzing the LA dehydration, the study on CaHPO₄ and its hydrate crystal as the research object is needed. A previous theoretical study on the dehydration reaction of LA to AA has been

done by Paul et. al¹⁰¹ on zirconia. On different zirconia surfaces, including (011), (101) and (111), it was found LA is preferentially stabilized in a bidentate bridging mode upon the Zr-O acido-basic site. Then a dehydration of H₂O molecule, where the α -OH cleaves from LA and the H comes from the methyl group, occurs thanks to the acido-basic site. Here the acid site Zr⁴⁺ acts as an acceptor of the α -OH and the basic O site on the zirconia plays the role of receiving H, which clearly shows the importance of acido-basic pair in dehydration reactions, and implies the necessity of modeling the acido-basic properties on the surface. Many studies focusing on the vibration of the bulk^{232,252} and the vibration of a portion of the crystal, especially the important clusters inside the crystal^{253,254} are studied theoretically. However, few theoretical infrared spectra studies on the surface determination under reaction temperature have been done. In the present work, acid and basic sites of alkaline-earth phosphates catalysts probed by NH₃ and CO₂ adsorption were characterized by IR spectroscopy at the dehydrated state and in the presence of water vapor. The IR spectra were assigned from DFT calculations which also explained acido-base properties determined by NH₃ and CO₂ adsorption. Characterization of acidity was strengthened by adsorption of pyridine and lutidine followed by IR spectroscopy.

According to the study performed by our experimental cooperator Loridant, correlations between the NH₃ and CO₂-TPD curves and the AA selectivity using alkaline earth phosphates as catalysts were established²⁵⁵. First, only the catalysts with only weak acid and basic sites were selective and their NH₃ and CO₂-TPD curves were surprisingly quite similar. Furthermore, the best AA selectivity was obtained for an acid to base balance close to 1 suggesting the participation of acid base pairs in the mechanism. Though, TPD measurements were achieved after pre-treatment at the calcination temperature while water vapor was present in the reaction feed and generated by dehydration. More recently, characterization of the prepared alkaline earth phosphates showed the presence of a surface amorphous layer containing POH species²⁵⁶. In situ DRIFT measurements have revealed that formation of POH groups was favored under water vapor and that these species interacted with reactants or reaction products at the

reaction temperature.

4.2.2 Computational details

Density functional theory (DFT) calculations were carried out using the Vienna ab initio simulation package (VASP)^{156–158}. The exchange and correlation terms were obtained by the Perdew–Burke–Ernzerhof form of Generalized Gradient Approximation (GGA-PBE)⁶⁹ functional. The core electrons were kept frozen and a projector-augmented wave (PAW) method was used to substitute the core electrons⁸¹. A cutoff energy of 550 eV of the plain wave basis set was used to describe the valence electrons. The bulk optimization would reach the convergence when the energy was converged to 1×10^{-6} eV and the force was smaller than 0.01 eV/Å with a k-point mesh of $5 \times 2 \times 5$. For the optimization of the slab, same energy convergence was used as bulk, for forces convergence, a criteria of 0.03 eV/Å was used, and a $5 \times 5 \times 1$ k-point mesh was used in the super cell calculation.

Considering Barium and Calcium have the same valence shell structure, which gives the similar electrostatic interaction between phosphates. For the sake of simplifying the building of the structure, we used Calcium, which is better characterized in previous studies^{232,233,257}, in the following modeling. As is discussed in our previous work²⁵⁶, the surface property information obtained from XPS, NMR, DRIFT and TEM all showed the presence of a surface amorphous layer, so a bulk of brushite ($\text{CaHPO}_4 \cdot 2\text{H}_2\text{O}$) is modeled first as the base of the amorphous surface. The surfaces were cleaved in three different directions including (001), (010) and (100). The surface energy for them are 0.047 eV/Å², 0.016 eV/Å² and 0.032 eV/Å² respectively, then the most favorable surface (010) surface was studied in our work. The (010) surface was cleaved to a $p(2 \times 2)$ slab constructed using 16 $\text{CaHPO}_4 \cdot 2\text{H}_2\text{O}$, where top surface layer, including 8 $\text{CaHPO}_4 \cdot 2\text{H}_2\text{O}$, were allowed to relax while the bottom 8 $\text{CaHPO}_4 \cdot 2\text{H}_2\text{O}$ were constrained during the geometry optimization. A vacuum layer of 15 Å is used to avoid the interaction between

the slabs.

The IR spectroscopy is modeled by accurately determining the vibrational spectrum of a system. We used the density functional perturbation theory in our study to determine the Hessian matrix, and finally obtain the frequency of every vibration mode²⁵⁸.

The surface energy of a symmetric bare surface Γ_{sym} and the asymmetric surface are calculated using the equation in Chapter 2 to investigate the water coverage on the surface.

The scaling factor between experimental and DFT is 0.98 for the wave number of stretching vibration modes and 1.00 for wave numbers of the bending vibration modes as shown in [Table 4.1](#).

Table 4.1 Scaling factor of different vibration mode between experimental and the original DFT NH_3 vibration data

	Mode	frequency_exp/cm ⁻¹	frequency_dft/cm ⁻¹	scaling
Stretching N-H	ν_{as}	3444	3519	0.98
	ν_{s}	3336	3395	0.98
	δ_{as}	1628	1623	1.00
Bending H-N-H	δ_{as}	1628	1614	1.00
	δ_{s}	950	1001	0.95

4.2.3 The construction of the surfaces

The Brushite is a layered oxide as shown in [Figure 4.5](#). The bulk structure of brushite was built based on the neutron single crystal diffraction study²³³, with a composition of $4 \text{ CaHPO}_4 \cdot 2\text{H}_2\text{O}$. The brushite structure is C-centered monoclinic with space group Cc (#9, C_s^4), with the calculated cell parameter of $a=5.98 \text{ \AA}$, $b=15.14 \text{ \AA}$ and $c=6.24 \text{ \AA}$, which has a good consistence with the experimental data where $a_{\text{exp}}=5.80 \text{ \AA}$, $b_{\text{exp}}=15.13 \text{ \AA}$, $c_{\text{exp}}=6.32 \text{ \AA}$ ²³³. A detailed description of the brushite can be found in Hirsch's work²³².

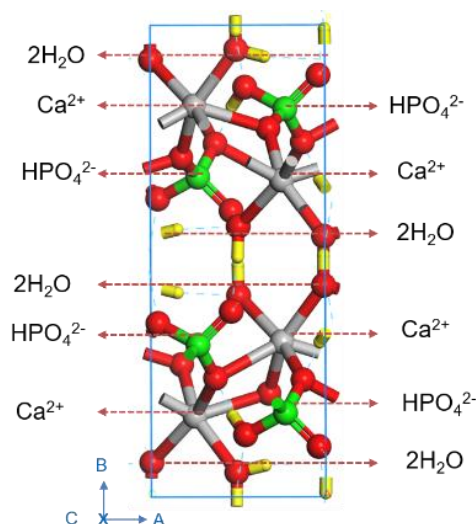


Figure 4.5 Layered structure of the Brushite unit cell, containing Ca atoms (grey), O atoms (red), H atoms (yellow) and P atoms (green)

As we mentioned before, the surface is found to be amorphous. To represent this amorphous surface, several periodic surfaces with different amount of water were used. They are shown in **Figure 4.6**.

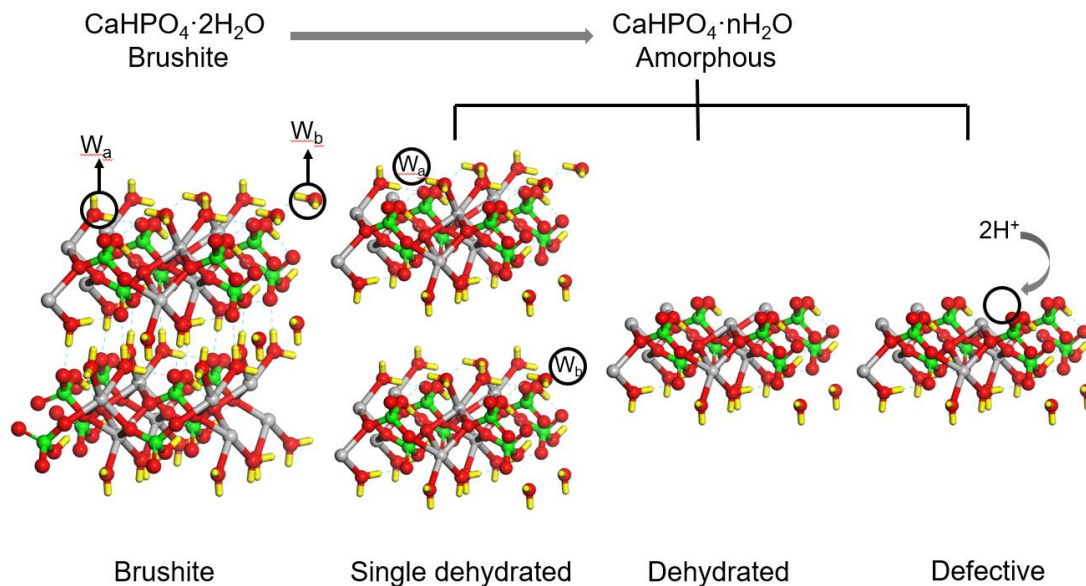


Figure 4.6 Different possible surfaces (side view) of $\text{CaHPO}_4 \cdot n\text{H}_2\text{O}$, grey for Calcium, red for oxygen, green for phosphorus and yellow for hydrogen

As is shown in **Figure 4.6**, the top of the (010) surface of Brushite, is covered with 2 layers of water, one layer of water is perpendicular to the surface, marked as W_a , W_a is 2.55 Å far away from the nearest Ca^{2+} atom, it has a H bond with the O on HPO_4^{2-} and with another H_2O molecule nearby. The other layer of water is parallel to the surface, marked as W_b , W_b is above the Ca^{2+} atom with a distance of 2.47 Å and has a H bond with W_a . To mimic the amorphous surface, different numbers of water were deleted as shown in **Figure 4.6**. In the case of dehydrating one water, both W_a and W_b were deleted, and it was found that the structure with W_b deleted is -0.21 eV more stable than the other case. Also, a dehydrated surface was also computed, where the top two layers of water were deleted but the water inside and the water in the bottom layers were still reserved. To have a more comprehensive description of the possible surface structure, a defective surface was also constructed with a Ca^{2+} vacancy and completed with two H.

Different temperatures lead to different thermal decomposition of Brushite, and finally lead to different surface structures. The thermal decomposition of Brushite ($CaHPO_4 \cdot 2H_2O$) to Monetite ($CaHPO_4$) and the amorphous phases has been studied systematically by Dosen⁵². It was found that Brushite starts to dehydrate around 80 °C, and Monetite begins to form between 130 °C and 140 °C and is complete between 200°C and 220 °C, as soon as Brushite starts to lose water, the amorphous then starts to form. To confirm the surface structure at different temperatures, an ab initio thermodynamic study was performed in **Figure 4.7**.

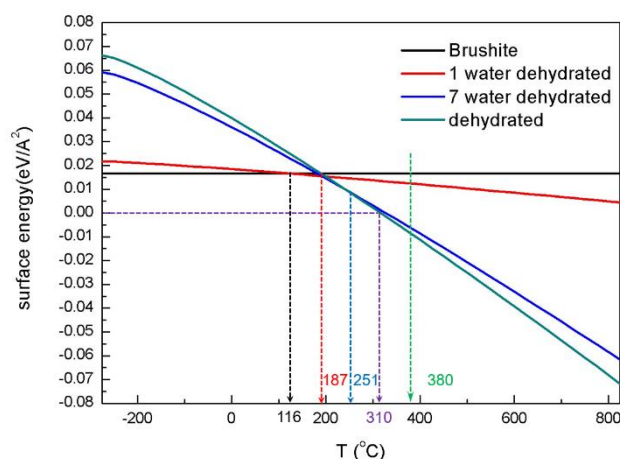


Figure 4.7 Ab initio thermodynamic curve of different surfaces at different temperature under 1 atm

As shown in Figure 4.7, four different possible surfaces, Brushite (with 2 layers of water, in total 8 water on the surface), 1 water dehydrated surface, 7 water dehydrated surface and the dehydrated surface as we mentioned before were modeled. It shows clearly the distribution of the surfaces under different temperatures. When the temperature is lower than 116°C, the surface prefers to be covered with water, so Brushite is the most favorable surface structures. At 116 °C, the surface starts to dehydrate, and between 116°C and 187 °C, it exists in the form of one top layer water W_b dehydrated. The computed temperature for Brushite starting to dehydrate is quite consistent with the experimental temperature 80°C as we mentioned before. The total dehydrate surface is the most stable surface when the temperature is higher than 251°C, which also shows a good consistency with experiments where the Monetite is complete between 200 °C and 220 °C. It is worth noting that although the total dehydrate surface supercell is not exactly the modeling of Monetite, as it still has water inside the supercell and on the bottom, they still have the same exposed surface structure which consists of CaHPO_4 . At the range of 116 °C and 251°C, the surfaces with different water coverages are distributed at different temperatures, such as an example we mentioned here, the surface with 1 water on the surface distributes mainly between 187°C and 251 °C. It should also be noted that the surface energy becomes negative when the temperature is higher than 310 °C, which means the reorganization of the bulk may occur. The most possible bulk structure should

be CaHPO_4 for the reorganization, which finally forms Monetite. But we will still use our surface modeling (based on the $\text{CaHPO}_4 \cdot 2\text{H}_2\text{O}$ bulk) in the following study, as we mentioned before that the exposed surface structure of our modeling can represent well the surface from Brushite to Monetite. Based on the above discussion, it is clear that at the reaction temperature $380\text{ }^\circ\text{C}$ (which is also the IR spectrum performing temperature), the most favorable surface is the dehydrated surface.

To have a more comprehensive view of the surface, the defective surface with a Ca^{2+} vacancy is also taken into consideration. The most favorable structure of the defective surface is shown in **Figure 4.8**.

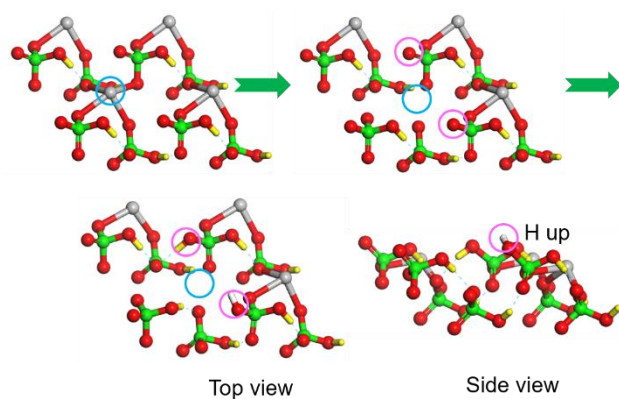
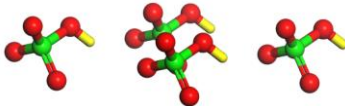
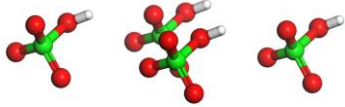


Figure 4.8 The generation of the defective surface with a Ca^{2+} vacancy, with top view above and side view below, blue circles show the changing of Ca^{2+} and the pink circles shows the addition of H^+ , H up is marked with white

As **Figure 4.8** shows, the two additional H^+ were added on two HPO_4^{2-} and generated 2 H_2PO_4^+ groups. One of the additional H points down to another HPO_4^{2-} inside with a H bond, we call it “H down”, while the other additional H points up to the outside, we call it “H up”. The “H up” is so stable that even if it was artificially placed down, it still tended to be up after optimization.

The special property of the “H up” is also tested in the total dehydrated surface in **Table 4.2**.

Table 4.2 Possible surface structures of the dehydrate surface and their possibilities of existence

No.	Surface structure*	Relative energy/eV	Boltzmann distribution $F_{(\text{Config X})}/F_{(\text{Config 1})}$
Config 1		0.00	\
Config 2		0.11	0.15
Config 3		0.49	0.0002

* H up shows in white and H down shows in yellow

The most stable structure of the total dehydrated surface is Config 1, the surface with 4 “H down”. But Config 2, the surface with one “H up” is also quite stable, only 0.11 eV less stable than Config 1, and the possibility of its existence is 0.15 compared to Config 1, which shows the rationality of the existence of Config 2. However, when it comes to Config 3, the surface with 4 “H up”, it becomes much less stable and its ratio compared to Config 1 is only 0.0002, which means the surface with 4 “H down” is impossible to exist. In fact, the H up and down represent different basic and acidic properties of the surface. The “H up” represents a Brønsted acid site, which is difficult to detect when the H is pointing inside the surface. The configuration distribution, namely, that in most cases the dehydrated surface exists in the Config 1 form, and might also reasonably exist in the Config 2 form, interprets the Brønsted acid sites detected from experiments well. Results have shown that the Brønsted acid sites exist, but in very small numbers, which is consistent with the experimental data. The similar study of the dehydrated surface with NH₃ adsorbate was also done in [Table A 4.2.1](#), in which the “H up” structure is still much more stable compared to the “H down” structure. It is also worth noting that when adsorbed with NH₃, the possibility of “H up” is even lower, only

0.04 compared to the “H down” structure, and there’s even no stable structure of 4 “H up” can be obtained. This shows the trend that with more NH_3 adsorbed on the surface, more H atoms prefer to be down.

4.2.4 TPD study on NH_3 and CO_2 adsorption on the catalytic surface

Our experimental collaborator also performed the TPD study of both CO_2 and NH_3 on CaPP-Na ($\beta\text{-Ca}_2\text{P}_2\text{O}_7$, tetragonal, ICDD 00-033-0297). Before the TPD, the surface was first heated with a rate of $10^\circ\text{C}/\text{min}$ upto 500°C in the Helium environment for 1 hour to desorb any possible adsorbates, then the catalysts were cooled to 100°C . After cooling down, a mixed flow, such as $\text{NH}_3\text{-He}$ or $\text{CO}_2\text{-He}$, was supplemented to adsorb NH_3 and CO_2 on the surface for 30 min followed 10 min of He flow under 100°C . Then the catalysts were then heated under He flow with a heating rate of $8^\circ\text{C}/\text{min}$ till 500°C . The acid and basic surface densities were calculated integrating the peaks areas from 100 to 450°C , using pulse calibrations and surface areas values⁵⁰.

They found it is quite interesting that NH_3 and CO_2 have the similar peak as shown in Figure 4.9, to figure out the reason of their similarity in adsorption property, we studied the adsorption energy of NH_3 and CO_2 on the dehydrated surface.

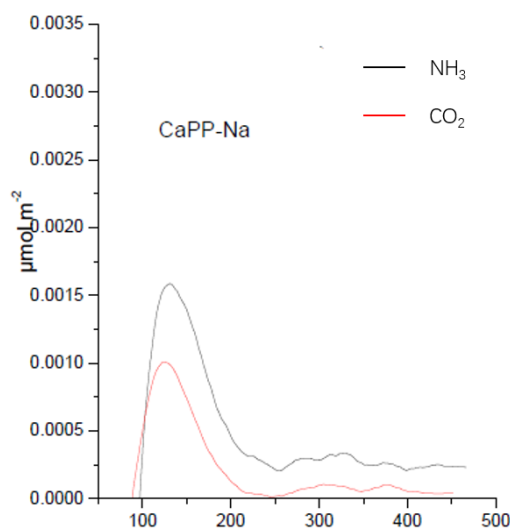


Figure 4.9 TPD curve of CO_2 and NH_3 adsorption on CaPP-Na

According to the redhead analysis²⁵⁹, we can have the Polanyi-Wigner equation under the hypothesis of desorption energy and pre-exponential factor are independent of coverage and temperature:

$$-\frac{d\theta}{dT} = \frac{A}{\beta} \theta^m \exp\left(\frac{-E_d}{RT}\right) \quad \text{eq. 4.2.1}$$

A: pre-exponential factor

θ : coverage

E_d : desorption energy

β : heating rate

T: temperature

R: gas constant

m: kinetic desorption order

The derivation at T_p (T at peak) $-\frac{d\theta^2}{dT^2} = 0$ in the TPD curve, so we can obtain the equation:

$$\frac{E_d}{RT_p^2} = \frac{A}{\beta} m \theta^{m-1} \exp\left(\frac{-E_d}{RT_p}\right) \quad \text{eq. 4.2.2}$$

If both the adsorption of NH_3 and CO_2 are the first order desorption, i. e. the desorption of the molecules is a monolayer desorption, then we can obtain the relation between the E_d and T_p

$$E_d = RT_p \left(\ln\left(\frac{AT_p}{\beta}\right) - \ln\left(\frac{E_d}{RT_p}\right) \right) \quad \text{eq. 4.2.3}$$

Considering the heating rate β remains unchanged during the TPD analysis, if the T_p has the same number, then it is clear that the desorption energy E_d should also be the same. However, in our dehydrated surface, the adsorption energy of an NH_3 is -0.92 eV, and for CO_2 it is -0.27 eV. If taking the coverage effect into account, the desorption energy of per NH_3 is -0.90 eV (with a monolayer of NH_3 molecules), and the adsorption

energy of per CO₂ is -0.28 eV (with a monolayer of CO₂ molecules). The adsorption on defective surface is also investigated. The desorption energy of per NH₃ on defective surface is -0.92 eV (with a monolayer of NH₃ molecules), and the adsorption energy of per CO₂ on defective surface is -0.27 eV (with a monolayer of CO₂ molecules). The inconformity of the adsorption energy between NH₃ and CO₂ can have two explanations : (1) the hypothesis we mentioned before is invalid, which means in this study, the desorption energy and pre-exponential factor changes a lot with the changing of coverage and temperature ; (2) The adsorption here may not be a monolayer adsorption, especially for NH₃, which has a quite strong adsorption on the surface, but it desorbs a lot even in a very low temperature shown in TPD curve.

To confirm the property of the multilayer adsorption for NH₃, we adsorbed another layer of NH₃ on the monolayer of NH₃ as shown in **Figure 4.10**.

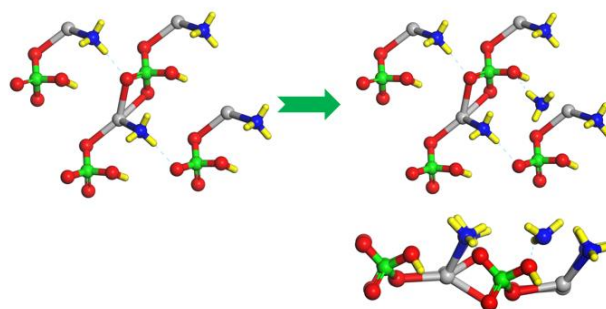


Figure 4.10 The adsorption of the second layer NH₃

The second layer NH₃ has a distance of 2.59 Å to Ca²⁺, a bit longer than the distance compared to the first layer NH₃, 2.51 Å. Like the first layer NH₃, it still has a H bond with the nearby HPO₄²⁻, but for the second layer the H bond is connected with the O from OH, and for the first layer NH₃, it comes from the interaction between O and NH₃. The adsorption energy of the second layer NH₃ is -0.53 eV (-50 kJ/mol), quite close to the experimental data as shown in **Figure 4.11** (65 kJ/mol). So, it is speculated that the adsorption of NH₃ should be a multilayer adsorption. However, the similar peak of CO₂ and NH₃ TPD curve still remains unsolved. To unravel the similarity between CO₂ and

NH₃ in the TPD curve, two possibilities were also modeled: (1) Taking the dispersion correction into consideration to obtain a more proper adsorption energy. To verify such a possibility, we optimized the bulk and then the slab using the D3 dispersion, and calculated the second layer NH₃ adsorption and the first layer CO₂ adsorption, it was found the values were -0.70 eV (-67 kJ/mol) and -0.44 eV (-42 kJ/mol) respectively, the close energies can explain the similarity of the TPD curve in some degree. (2) The incomplete desorption of water (remains one most stable water) in the pretreatment of the TPD curve measurement is also taken into consideration. With the water residual upon the surface, the possibility of generating HCO₃⁻ rises up. The most stable structure of HCO₃⁻ on the dehydrated surface were shown in [Figure A4.2.2](#). The reaction energy of $\text{H}_2\text{O} + \text{CO}_2 + \text{HPO}_4^{2-} \rightarrow \text{HCO}_3^- + \text{H}_2\text{PO}_4^-$, or we say the CO₂ adsorption energy in this case is only -0.002 eV, but the adsorption energy of NH₃ in this case is still quite large, up to -0.99 eV, close to the pure NH₃ adsorption, which means the impossibility of this case. In summary, during the TPD process, only the second layer of NH₃ molecules desorb, and the first layer of NH₃ molecules are too stable to be desorbed. The adsorption energies of the second layer NH₃ and CO₂ are quite close, which explains the similarity of the TPD curve. But the adsorption of NH₃ is still a bit stronger than the CO₂ adsorption, which explains NH₃ peak is a bit back forward in the TPD curve than the peak of CO₂.

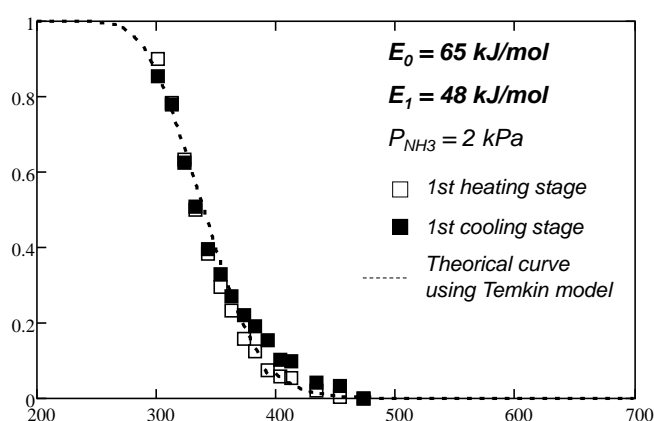


Figure 4.11 Determination of heats of NH₃ adsorption using AEIR, E_0 represents the adsorption energy at zero coverage and E_1 represents the adsorption energy of full coverage

4.2.5 IR spectrum study on NH₃ adsorption on a dehydrated surface

Based on the structural study above, in the following IR spectra study, we mainly focused on the dehydrated surface and the defective surface.

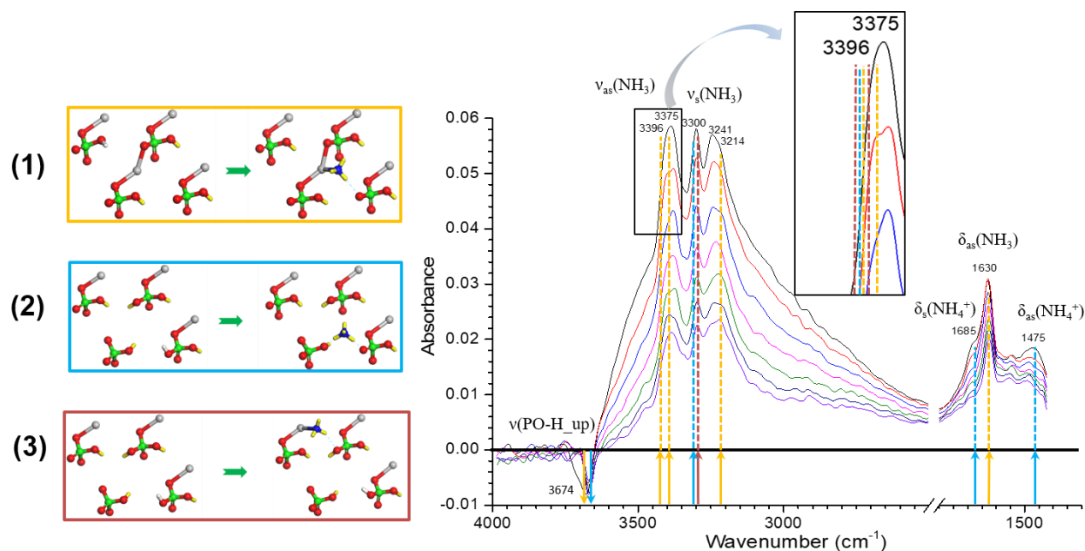


Figure 4.12 The comparison of differential IR spectra between experimental and scaled computed results, the left shows the different models marked with different colors, the right shows the experimental IR spectra and the computational results with straight lines, arrow up shows the appearance of the peak and the arrow down shows the disappearance of the peak, magnified area shows all the scaled DFT results in this area, detailed scaled DFT wavenumber information can be found in Appendix (Table Table A 4.2.2 to Table A 4.2.4).

In the IR spectra figure, there are mainly two peaks needed to be paid attention to. First is the disappearing peak of 3674 cm^{-1} . The peak shows a normal O-H stretching vibration. Considering the surface is pretreated with a high temperature dehydration process, H₂O cannot contribute to such a peak. Hence the only possible source comes from the PO-H vibration. Normally a free O-H can lead to such a peak around 3700 cm^{-1} , the only possible way to obtain the disappearance of the peak should be the constrained O-H vibration, such as the H bonding of the PO-H with the HPO₄²⁻. In the dehydrated surface and the defective surface, the free PO-H can be the “H up” case and the constrained PO-H can be the “H down” case. The disappearing of the peak 3674 cm^{-1} can

be the changing of the H orientation in PO-H, i. e. the case from “H up” to “H down”. The second important peak is the appearance of the peak around 3200 cm^{-1} . We used to think the peak is the PO-H vibration with a H bond with NH_3 , we also constructed a dehydrated surface with an NH_3 adsorbed directly upon the PO-H with an H bond connected, the adsorption energy of this configuration is -0.50 eV , and the frequency of the PO-H in this situation is only 2451 cm^{-1} . The low adsorption energy and the far away frequency shows clearly the impossibility of such a H bonding PO-H --- NH_3 adsorption state. As the peak is quite close to the symmetric stretching of an NH_3 molecule in gas phase, 3336 cm^{-1} , we think it maybe a new NH_3 stretching peak that is affected by the surrounding environment. According to the above inference, we modeled the NH_3 adsorption both on the dehydrated and defective surface, focused on the orientation of the PO-H and the different positions of the NH_3 , to try to find a proper configuration both from the energetic and the spectral aspect.

For model (1), possible adsorption of NH_3 on dehydrated surface has been computed and the adsorption structure in model (1) is the most favorable. The NH_3 generates a 2.06 \AA bond with the Ca^{2+} cation. The NH_3 also has an H bond with the top layer O from the HPO_4^{2-} nearby. In this case, the adsorption energy of NH_3 is -0.92 eV , which is much more stable than when the NH_3 captures an H from HPO_4^{2-} and becomes an NH_4^+ , where the adsorption energy is only -0.12 eV . Then, we compare the IR spectra before and after the adsorption of NH_3 . In the experimental IR spectra, it is shown that after the adsorption, the peak at 3674 cm^{-1} disappears, and several peaks around 3000 cm^{-1} and 1600 cm^{-1} appear, as shown in [Figure 4.12](#). According to the computational results, it is known that the disappearing peak at 3674 cm^{-1} is related to the PO-H up to PO-H down. The peak at $3375/3396\text{ cm}^{-1}$ is the NH_3 asymmetric stretching peak, and due to the surrounding environment, the symmetry is broken and the asymmetric stretching splits into two similar peaks. However, there still remains only one symmetric stretching NH_3 peak at 3227 cm^{-1} . The peak at 1630 cm^{-1} shows the asymmetric bending of NH_3 .

Model (2) and model (3) both occur on the defective surface. The adsorption energy

of model (2) is -1.22 eV and -0.87 eV for model (3). Model (2) is the most stable structure after the adsorption of NH_3 on the defective surface. The adsorbed NH_3 captured the “H up” from the H_2PO_4^- and generated H bonds with the nearby oxygens. Model (3) is the most stable one when the “H up” site has already been occupied, the NH_3 also adsorbed on the Ca^{2+} , like model (2), but with longer bond, the bond length is 2.53 Å bond in this model, which also leads to a weaker adsorption compared to model (1). A combined structure of these two models was also tested in [Table A 4.2.5](#) to confirm the consistency of their vibration information with the separate models. The co-adsorption energy of 2 NH_3 on the defective surface is -2.00 eV, maintains frequencies similar to their separate adsorption. The asymmetric vibrations of NH_3 (or NH_4^+ in model (2)) are always located around 3400 cm^{-1} , which is a bit higher than the experimental peak $3375/3396\text{ cm}^{-1}$. The two models also both mimic the symmetric stretching of NH_3 (NH_4^+ in model (2)) quite well, with a wavenumber of 3360 cm^{-1} in model (2) and 3303 cm^{-1} in model (3). This is consistent with the experimental wavenumber 3300 cm^{-1} . Considering the different properties of the adsorbates on the surface, model (2) simulated well the bending information of NH_4^+ and model (3) simulated well the bending peak of NH_3 .

Now let's go back to the two original key peaks, the disappearance of the peak 3674 cm^{-1} and the appearance of the peak around 3200 cm^{-1} . We consider both the dehydrated and the defective surface exist in the whole surface, then (1) The disappearance of the peak 3674 cm^{-1} mainly comes from the PO-H from “H up” to “H down” in dehydrated surface. We also tested the possibility of this case in defective surface, but it turned out to be that the “H up” case cannot become the “H down” configuration. (2) The appearance of the peak around 3200 cm^{-1} comes from the symmetric stretching of NH_3 in dehydrated surface.

4.2.6 IR spectrum study on NH_3 adsorption on a dehydrated surface in water environment

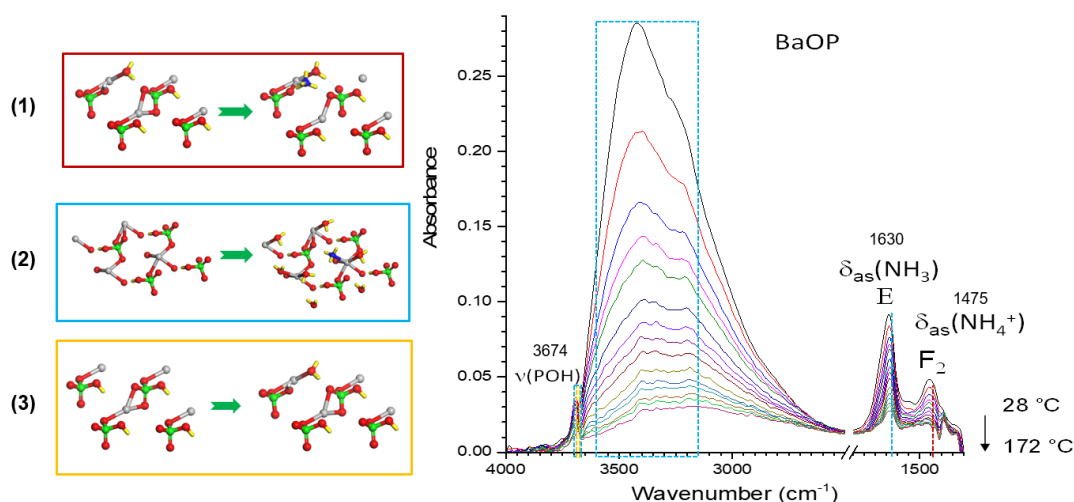


Figure 4.13 The comparison of differential IR spectra between experimental and scaled computed results, the left shows the different models marked with different colors, the right shows the experimental IR spectra and the computational results with dashed lines and dashed rectangles, detailed scaled DFT wavenumber information can be found in Appendix (Table A 4.2.7 to Table A 4.2.9).

From experiments we know that when the adsorption of NH_3 in the water environment, as is shown from the FTIR spectra, it shows a quite different properties compared with the spectra when only adsorbing NH_3 . The peak at 3674 cm^{-1} increases with the co-adsorption of water, and the peaks where used to be the stretching of the NH_3 becomes much more indistinguishable and become one broad band with the bunch of vibrations around 3000 cm^{-1} . Also, the peak of the asymmetric NH_4^+ bending at 1475 cm^{-1} increases a lot, which indicates the easier generation of NH_4^+ when we have water in NH_3 gas flow.

The appearance of the peak at 3674 cm^{-1} : This peak normally comes from two possible groups, the PO-H_{up} vibration and the HO-H vibration. Considering during the adsorption of NH_3 , the PO-H from down to up is not favorable as confirmed both in IR spectrum and the computational results, if the appearance of the peak in 3674 cm^{-1} mainly comes from the PO-H_{up}, the only possibility is the PO-H from down to up after the adsorption of water. The most favorable surface structure co-adsorbed with one water both on dehydrated and the defective surface is both the case when PO-H is pointing

inside the surface (except the case that the original PO-H is pointing to the outside in defective surface), with the energy difference of 0.09eV with the artificial one H pointing up on dehydrated surface (see Table A 4.2.6), but for defective surface the H up case is too unstable to exist. The close energy between the PO-H_{up} and PO-H_{down} in dehydrated surface with a H₂O molecule co-adsorbed indicates the PO-H from down to up, may contribute to the appearance of this peak, as is shown in (3). Such an increase of this peak also indicates the increase of the Bronsted acid sites. However, considering the surface with PO-H up is a perfect position for the adsorption of NH₃ and generating NH₄⁺ (with an adsorption energy of -0.57 eV, with the process shown in Table A 4.2.8), this PO-H up may contribute little for the increase of the peak around 3674 cm⁻¹. The similar trend was found by Panpranot in the methanol dehydration to dimethyl ether catalyzed by AlPO₄, where the pretreatment with water vapor showed to result in an increase of catalytic activity of AlPO₄. And the improvement of the catalytic activity was proposed to be increase of the Bronsted acid sites on the pretreated AlPO₄²⁶⁰. There's also another possibility, that the appearance of the 3674cm⁻¹ peak comes from the water. To confirm the water configuration on the surface, a decomposition test of the water was done both on dehydrated and defective surface. It was found that in both cases, the water always exists in the form of H₂O and no decomposition occurred. This means it is the HO-H vibration may also contribute to the appearance of the peak of 3674cm⁻¹. As the process (2) and (3) shows clearly that after the adsorption of H₂O, the peak around 3674cm⁻¹ appears. For (2), only one peak of 3698cm⁻¹ comes from the vibration of H₂O. However, considering the asymmetric environment of the surface, the H₂O vibration from process (2) takes up a range from 3645~3700cm⁻¹.

The indistinguishable band between 3000cm⁻¹ and 3500cm⁻¹: No matter the dehydrate surface or the defective surface, they both have a more symmetric environment for the adsorption of NH₃, which makes the vibration of the NH₃ quite unique. But when the water also takes part in the adsorption, the symmetric environment is broken and the vibration of the NH₃ shows the similar peak but not exactly the same, also, more water

adsorbed on the surface, as the process (2) shows, more water molecules will be taken into the vibration, at last in the spectra, it shows the property of a large range of noisy peaks, which exactly comes from the co-vibration of many H₂O molecules and NH₃ molecules.

The increasement of the NH₄⁺ peak at 1475 cm⁻¹: When co-adsorbed with water, the asymmetric bending peak of NH₄⁺ increased a lot, which may come from the following three aspects: first is the H capture from PO-H becomes much easier and the co-adsorbed water also provides the source of H; second is the pre-adsorption or the co-adsorption of water makes the adsorption of NH₄⁺ much easier and increase the coverage of the NH₄⁺ on the surface; third is the possibility of the existence of more vacancies. For the first hypothesis, we first tested the possibility of the H capture from the neighboring water. However, both on dehydrated and defective surface, the decomposition of the water and giving an H to NH₃ is impossible, the water always tends to stay in the form of H₂O. We also computed the situation when the H source comes from the PO-H_{down}. On the dehydrated surface, it is found that NH₃ still prefers to exist in the form of NH₃, and generates an H bond with PO-H in the top layer as shown in [Figure A4.2.1](#). On the defective surface, NH₃ can capture the H from the PO-H up and generates NH₄⁺, which is the normal way of generating NH₄⁺ as we mentioned before without the co-adsorption of water. Considering the increasement of the bending peak of NH₄⁺, cases with several “H up” on defective surfaces were computed but none of them was stable enough to exist. To verify the second hypothesis, one water is pre-first adsorbed on the defective surface, based on the pre-adsorbed water dehydrated surface, the adsorption energy of NH₄⁺ is -1.13 eV, that is weaker than the adsorption on the defective surface (-1.22 eV, as shown in [Table A 4.2.3](#)), indicating the adsorption of NH₄⁺ on defective surface does not be favored by the pre-adsorption of some H₂O molecules. But as we mentioned in the previous paragraph, the preadsorption of H₂O favors the appearance of PO-H up in dehydrated surface, which provides positions for the generation of NH₄⁺, and finally enlarge the signal of NH₄⁺ stretching as shown in process (1). Then it comes to the third

hypothesis, the increasing of the Ca^{2+} vacancies in the water abundant environment. As we mentioned before, the NH_4^+ is easy to exist in the presence of Ca^{2+} vacancies, where the PO-H up is easy to generate, and the existence of the PO-H up is a key site for the generation of NH_4^+ . The generation of the Ca^{2+} vacancy can come from such reaction: $\text{Ca}^{2+} + 2\text{H}_2\text{O} \rightarrow \text{Ca}(\text{OH})_2 + 2\text{H}^+$, and the addition of OH^- from H_2O is a key step. However, no matter in the defective or in the dehydrated surface, as we mentioned before, the cleavage of H_2O is almost impossible, and the only stable structure we obtained is the case on the dehydrated surface (as shown in [Figure A4.2.3](#)) but with 1.74 eV less stable than the most favorable defective surface with unbroken water.

It is also worth noting that the bending peak around 1630 cm^{-1} , which is considered to be the asymmetric vibration of NH_3 . It was found in the hydrated surface with NH_3 adsorbed on the surface, this peak is indeed a vibration combined with H_2O and NH_3 bending.

4.2.7 Conclusion

Based on the characterization by our experimental cooperator, we built the proper model of the catalyst, which we used a mixed surface of dehydrated and defective surface to represent the amorphous surface. By modeling the TPD and IR spectrum, we obtain the following conclusion both on experimental and on theoretical side:

- The similarity of the NH_3 and CO_2 -TPD curves come from the second layer desorption of NH_3 and the first layer desorption of CO_2 . It was found that the first layer of NH_3 molecules are too stable to be desorb, but the adsorption energy of the second layer of NH_3 molecule is bit stronger than the adsorption energy of CO_2 , which contributes to the similar TPD curve.
- The best catalyst for the LA dehydration to AA has a ratio of acid: base = 1. In our modeling of dehydrated surface, the ratio between the acid sites(Ca_2^+) : basic sites (PO)=1. For the defective surface, the ratio between the acid sites(Ca_2^+) : basic sites (PO+PO-H) still equals to 1, which validates the modeling from a rough view.

- The experimental IR spectrum is well reproduced by DFT both in the vacuum or in the water environment. Experimentalists found that the formation of POH groups was favored under water vapor, through the modeling of catalysts under water environment, it is considered that the water vapor helps the existence of PO-H_{up} compared to the non-water vapor case.

Appendix 4.2

Table A 4.2.1 Possible surface structures of the NH₃ on dehydrated surface and their possibilities of existence

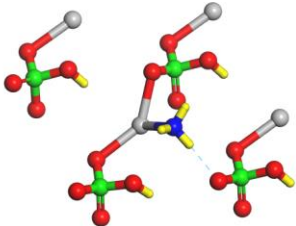
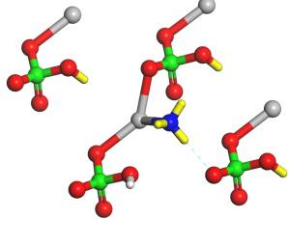
No.	Surface structure	Relative energy/eV	Boltzmann distribution $F_{(\text{Config X})}/F_{(\text{Config 1})}$
Config 1		0.00	\
Config 2		0.18	0.04

Table A 4.2.2 Frequencies of NH₃ adsorption on dehydrated surface

NH ₃ @dehydrate	Peak_exp/cm ⁻¹	Peak_dft/cm ⁻¹	Peak type
Peaks disappear	3674	3690	PO-H up
	3375/3396	3380/3438	$\nu_{\text{as}}(\text{NH}_3)$
Peaks appear	3300	/	/
	3241/3214	3227	$\nu_{\text{s}}(\text{NH}_3)$
	1630	1639	$\delta_{\text{as}}(\text{NH}_3)$

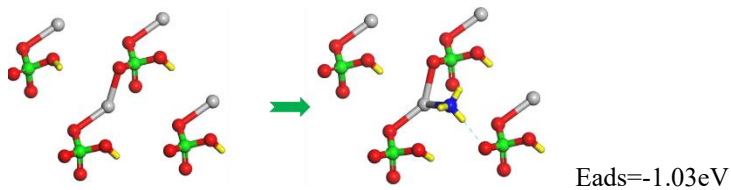
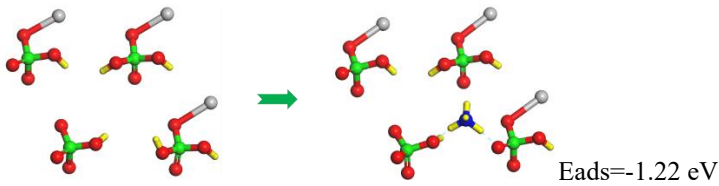
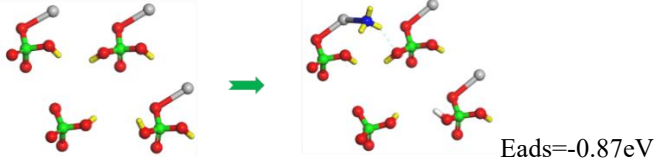


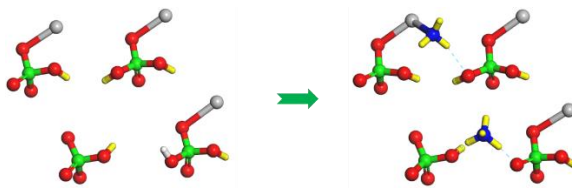
Table A 4.2.3 Frequencies of NH_4^+ adsorption on defective surface


NH_4^+ @defect	Peak_exp/ cm^{-1}	Peak_dft/ cm^{-1}	Peak type
Peaks disappear	3674	3665	PO-H_up
	3375/3396	3439	$\nu_{\text{as}}(\text{NH}_4^+)$
	3300	3360	$\nu_{\text{s}}(\text{NH}_4^+)$
Peaks appear	3241/3214	/	/
	1685	1679	$\delta_{\text{s}}(\text{NH}_4^+)$
	1475	1465	$\delta_{\text{as}}(\text{NH}_4^+)$

Table A 4.2.4 Frequencies of NH_3 adsorption on defective surface


NH_3 @defect	Peak_exp/ cm^{-1}	Peak_dft/ cm^{-1}	Peak type
Peaks disappear	3674	/	/
	3375/3396	3399/3443	$\nu_{\text{as}}(\text{NH}_3)$
	3300	3303	$\nu_{\text{s}}(\text{NH}_3)$
Peaks appear	3241/3214	/	/
	1630	1630	$\delta_{\text{as}}(\text{NH}_3)$

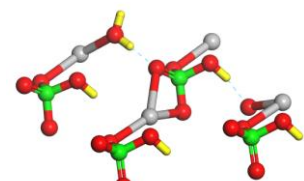
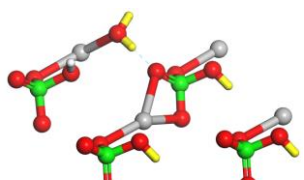
Table A 4.2.5 Frequencies of NH₃ and NH₄⁺ co-adsorption on defective surface



Eads=2.00 eV

NH ₄ ⁺ @defect	Peak_exp/cm ⁻¹	Peak_dft/cm ⁻¹	Peak type
Peaks disappear	3674		/
	3375/3396	3466/3461/3422	ν _{as} (NH ₃)
	3300	3364/3321	ν _s (NH ₃)
Peaks appear	3241/3214	/	/
	1685	1676	δ _s (NH ₄ ⁺)
	1630	1623	δ _{as} (NH ₃)
	1475	1457	δ _{as} (NH ₄ ⁺)

Table A 4.2.6 Possible surface structures of the H₂O on dehydrated surface and their possibilities of existence

No.	Surface structure	Relative energy/eV	Boltzmann distribution $F_{(\text{Config X})}/F_{(\text{Config 1})}$
Config 1		0.00	\
Config 2		0.09	0.20

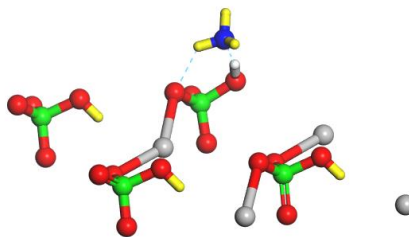
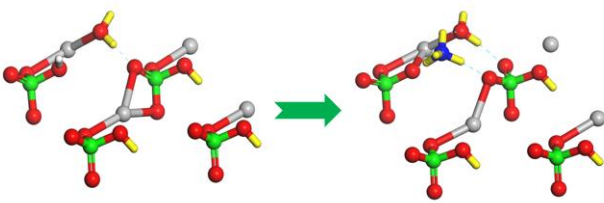


Figure A4.2.1 NH₃ adsorption on dehydrated surface with an H bond between HPO₄

Table A 4.2.7 Frequencies of NH₃ and water adsorption on a dehydrated surface

	Peak_exp/cm ⁻¹	Peak_dft/cm ⁻¹	Peak type
Peaks appear	3674	3645~3700	v(H ₂ O)
	3000~3600	3156~3598	v _{as} (NH ₃)
	1630	1637	v _s (NH ₃)& v(H ₂ O)

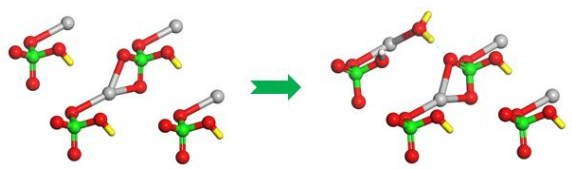
Table A 4.2.8 Frequencies of NH₄⁺ adsorption on a dehydrated surface with one water preadsorbed



$E_{\text{ads}} = -0.57 \text{ eV}$

	Peak_exp/cm ⁻¹	Peak_dft/cm ⁻¹	Peak type
		3506, 3270	$\nu_{\text{as}}(\text{H}_2\text{O})$
	3000~3600	3468	$\nu_{\text{as}}(\text{NH}_4^+)$
		3389	$\nu_{\text{s}}(\text{NH}_4^+)$
Peaks appear		3039, 3027	$\nu(\text{PO-H})$
	/	2901, 1718	$\nu_{\text{s}}(\text{NH}_4^+)$
	1630	1650, 1635, 1533	$\delta_{\text{s}}(\text{NH}_4^+)$
	/	1583	$\delta_{\text{s}}(\text{H}_2\text{O})$
	1475	1434	$\delta_{\text{as}}(\text{NH}_4^+)$

Table A 4.2.9 Frequencies of NH₄⁺ adsorption on a dehydrated surface with one water preadsorbed



$E_{\text{ads}} = -0.84 \text{ eV}$

	Peak_exp/cm ⁻¹	Peak_dft/cm ⁻¹	Peak type
Peaks appear		3698	$\nu(\text{H}_2\text{O})$
	3674	3676	$\nu(\text{PO-H}_{\text{up}})$

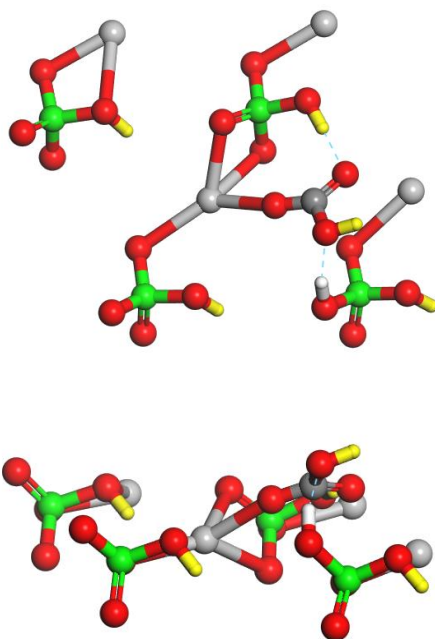


Figure A4.2.2 HCO_3^- on dehydrated surface (top view above and side view below)

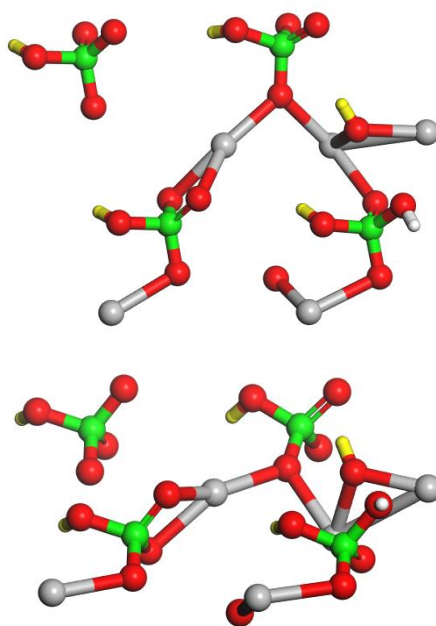


Figure A4.2.3 Dissociated H_2O on defective surface (top view above and side view below)

4.3 Dehydration reaction of 2,3-butanediol on Lanthanum phosphate (in cooperation with Jean Marc Millet in IRCELYON)

4.3.1 Introduction

As an important biomass derivative, methyl ethyl ketone (MEK) is an effective and common solvent and is also utilized in the synthesis of various fine chemicals and as a plastic welding agent²⁶¹, and the overall consumption of MEK in 2014 was over 1 000 000 t²⁶². The 2,3-butanediol (2,3-BDO) (\$200/ton, 98% purity) is found to be able to provide not only an environmentally friendly route but also an economical route to MEK (\$1700/ton, 99.9% purity)⁵.

Synthesis of MEK from 2,3-BDO has been reported over many heterogeneous catalysts such as H-Nafin²⁶³, zeolites^{264,265}, earth oxides^{266,267} and metal phosphates^{49,268,269}. Among all the possible catalysts for the 2,3-BDO dehydration, many metal phosphates show good ability and are considered to be outstanding catalysts in catalysing the dehydration reaction of 2,3-BDO to MEK thanks to its abundant basic and acid sites on the surface. A detailed 2,3-BDO dehydration study which covers many phosphate catalysts (including boron (BP), aluminum (AlP), titanium (TiP), zirconium (ZrP), and niobium (NbP) phosphates) have been done by Ivanova, and an activity order of the catalysts BP<TiP<ZrP=NbP<AlP is found with the highest selectivity towards MEK (78%) at 100% 2,3-BDO conversion under 250°C²⁶⁹.

However, along with the production of MEK, the amount of the product butadiene (BD) cannot be neglected no matter which catalyst is used. Fortunately, the product BD is also a valuable chemical product which can be used in hydrocarbon fuel, synthetic rubber, polymers, fibers and plastics²⁶¹. Kinetic model shows that reaction route for the production of 1,3-BD highly depends on temperature and that other routes are less dependent on temperature, which gives us an idea of adjust the temperature to adjust the selectivity of MEK and BD²⁶¹. Also, another solution can be to find a catalyst that can be

selective to both MEK and BD using its own morphology advantage, such as the different facets, should also be an ideal catalyst in the 2,3-BDO dehydration.

In our study, the Lanthanide phosphate was used in the 2,3-BDO dehydration. Both relatively high selectivity of BD and MEK was considered using different facets of the same catalyst. To understand the mechanism, especially the different selectivity of the different facets, theoretical calculations were also applied to model all the surfaces of the Lanthanide phosphate according to the experimental characterization.

4.3.2 Computational details

Density functional theory (DFT) calculations were carried out using the Vienna ab initio simulation package (VASP)^{156–158}. The Perdew–Burke–Ernzerhof form of Generalized Gradient Approximation functional (GGA-PBE) was used to obtain the exchange and correlation terms⁶⁹. To better describe the dispersion between molecules, the density-dependent dispersion correction (dDsC) has been applied. The core electrons were kept frozen and a projector-augmented wave (PAW) method was utilized to describe the electron-ion interactions by substituting the core electrons⁸¹. The valence electrons were described by setting a cutoff energy of 400 eV using the plain wave basis set. The bulk optimization would be converged when the energy was smaller than 1×10^{-7} eV and the force was smaller than 0.02 eV/Å with a k-point mesh of $7 \times 7 \times 7$. For the optimization of the slab, a 2×2 large, 3-layer thick surface is computed here with the bottom two layers fixed. The electronic self-consistent convergence was 1×10^{-6} eV and the ionic relaxation convergence is 0.02 eV/Å in geometric optimization at the gamma-point considering the system is relatively large.

The IR spectroscopy is modelled by accurately determining the vibrational spectrum of a system. We used the density functional perturbation theory in our study to determine the Hessian matrix, and finally obtain the frequency of every vibration mode²⁵⁸.

The surface energy of a symmetric bare surface Γ_{sym} and the asymmetric surface are calculated using the equation in Chapter 2.4.

The shape of the catalysts is constructed by Wulff law. Wulff law is a standard method to determine the equilibrium shape of bulk crystal, which can be found by the surface energy with respect to a given particle volume according to the Gibbs thermodynamic principle²⁷⁰. The Wulff law draws a proportional relationship between the surface area and the distances of its faces from one given point for a given volume.

To easily compare the experimental IR spectrum data and the DFT computed frequency, a scaling factor based on CO and C₂H₂ molecule is calculated in [Table 4.3](#).

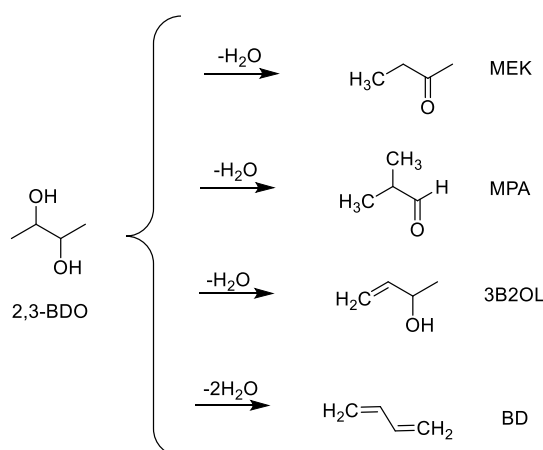
Table 4.3 Scaling factor of different vibration mode between experimental and the original DFT vibration data

	Mode	frequency_exp/cm ⁻¹	frequency_dft/cm ⁻¹	scaling
CO	v _{CO}	2140	2126	0.99
$\overleftarrow{\text{H}}-\text{C}\equiv\text{C}-\overrightarrow{\text{H}}$	v ₁	3373	3451	1.02
$\overrightarrow{\text{H}}-\text{C}\equiv\text{C}-\overrightarrow{\text{H}}$	v ₂	3295	3352	1.02
$\overleftarrow{\text{H}}-\overleftarrow{\text{C}}\equiv\overrightarrow{\text{C}}-\overrightarrow{\text{H}}$	v ₃	1974	2015	1.02

As is shown in [Table 4.3](#), the scaling factor between experiment and DFT calculation on CO is 0.99 and 1.02 on C₂H₂. In the following computation, a scaling factor of 1.005 (the average of 0.99 and 1.02) is used for the functional on surface, but when it comes to the molecular vibration of CO and C₂H₂, a scaling factor of 0.99 and 1.02 is still used here.

4.3.3 Experimental results

The general mechanism of the dehydration of 2,3-BDO is shown in [Scheme 4.2](#).



Scheme 4.2 General mechanism of 2,3-BDO dehydration

The product 3-buten-2-ol (3B2OL) is a direct dehydration product, while to obtain the product BD requires to go through two steps of dehydration. The product MEK and 2-methylpropanal (MPA) are the products of rearrangement. Different synthesis methods of NdPO_4 were compared and the sol-gel prepared NdPO_4 ($\text{NdPO}_4\text{-M1}$) gave the highest conversion of 2,3-BDO (total conversion), with 35% selectivity to MEK and 57% selectivity to BD and less than 10% byproduct, MPA and 3B2OL. Thus, in the following modelling, the characterisation of the NdPO_4 catalyst all comes from the $\text{NdPO}_4\text{-M1}$.

A TEM analysis of the $\text{NdPO}_4\text{-M1}$ and the length distribution is shown in [Figure 4.14](#).

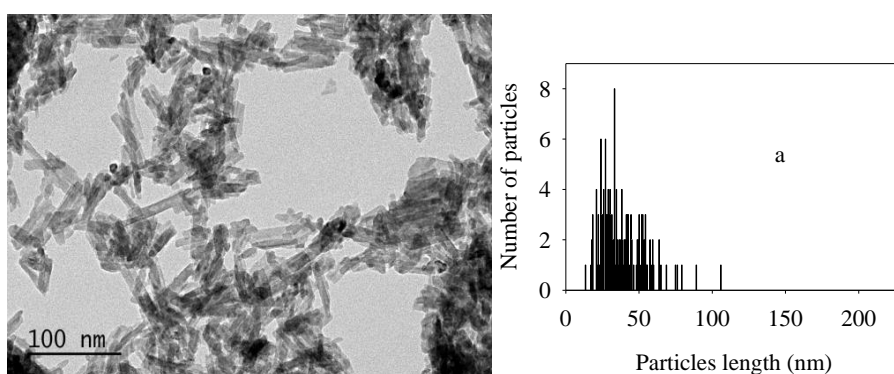


Figure 4.14 TEM of the $\text{NdPO}_4\text{-M1}$ (left) and the distribution of length of the particles (right)

Compared to other synthesis methods, the sol-gel method can produce shorter

catalytic rods. The maximum length distribution of the particles locates around 30~50 nm, the width of the particle is around 10 nm. So, the ratio between the length: width = 3~5.

A silylation method of NdPO_4 was developed by our experimental partners to figure out the different activity of the different facets of the NdPO_4 catalysts, where the catalysts were silylated first and then grinded the catalytic rods to cut them and obtain the catalyst with only the tip facet exposed. The selectivity of different products on different facets is shown in Figure 4.15.

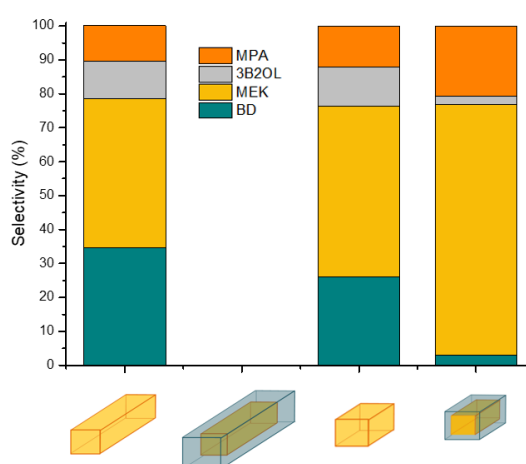


Figure 4.15 Selectivity of MPA, 3B2OL, MEK and BD catalysed by NdPO_4 rods, silylated NdPO_4 rods, cutted NdPO_4 rods and cutted silylated NdPO_4 rods (from left to right) at $T=320^\circ\text{C}$ when the conversion of 2,3-BDO=6%

The NdPO_4 rods both have Tip and Lateral facets exposed, with a selectivity to MEK around 44% and 35% to BD. In the case of silylated NdPO_4 rods, where all the facets are covered, no catalytic reactivity is observed, which also validates that the catalysts are well covered by silica. The cutted NdPO_4 rods have a similar product distribution with the NdPO_4 but are 10% more selective to MEK. The selectivity of MEK remarkably increases up to 79% in the cutted silylated NdPO_4 rods, which has only the Tip(001) facet. This study clearly shows the different selectivity of the Lateral facet and the Tip facet, that the Later facet is more selective to BD and the Tip facet is rather selective to MEK.

The interesting selectivity property of different facets rises interests on the study of both the Tip and Lateral facets, on which the characterization was performed to have a clear view of the surface structure and provided useful information for the theoretical modelling, which we will mention in the following text.

4.3.3 Modelling details

The Rhabdophane-type NdPO_4 catalysts were prepared by our experimental partners and used in the following characterization and reaction. In our modelling, LaPO_4 was modelled instead of NdPO_4 considering the similar chemical properties due to the similar electronic configuration. Also, the IR spectrums of different LNP have been studied by our experimental partners as shown in **Figure 4.16**, that the change of metal in LNP did not change the IR spectrum characteristic. The reactivity properties of light alcohol dehydration catalysed by them have also been tested by Nguyen²⁷¹, and all of them show similar conversion and selectivity to the dehydration products.

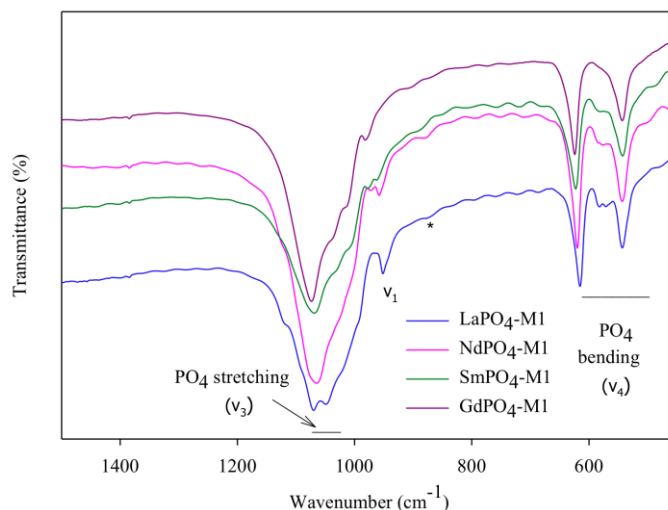


Figure 4.16 IR spectroscopy of different Lanthanide phosphates, blue line represents LaPO_4 , pink line represents NdPO_4 , green line represents SmPO_4 and purple line represents GdPO_4 , M1 means the catalysts are prepared using sol-gel method

The crystal structure of the LaPO_4 was obtained by our partners using XRD. The computed cell parameter in our modelling is $a=7.104 \text{ \AA}$, $b=7.104 \text{ \AA}$ and $c=6.419 \text{ \AA}$ with $\angle \text{AOB}=120^\circ$, which is optimized based on the experimental data where $a=7.081 \text{ \AA}$, $b=7.081 \text{ \AA}$ and $c=6.468 \text{ \AA}$ with $\angle \text{AOB}=120^\circ$ from the XRD. The computational cell parameter a and b are both 0.3% longer than the experimental one, and the computed cell parameter c is 0.8% shorter. The different quality of the a , b cell parameters and the c cell parameter between experimental results and computational results comes from the different bonding in different directions. It involves the P-O bond and the La-O bond both in a and b direction, while only weak La-O bond is found along the c direction. The crystal structure of the Rhabdophane-type LaPO_4 is shown in **Figure 4.17**.

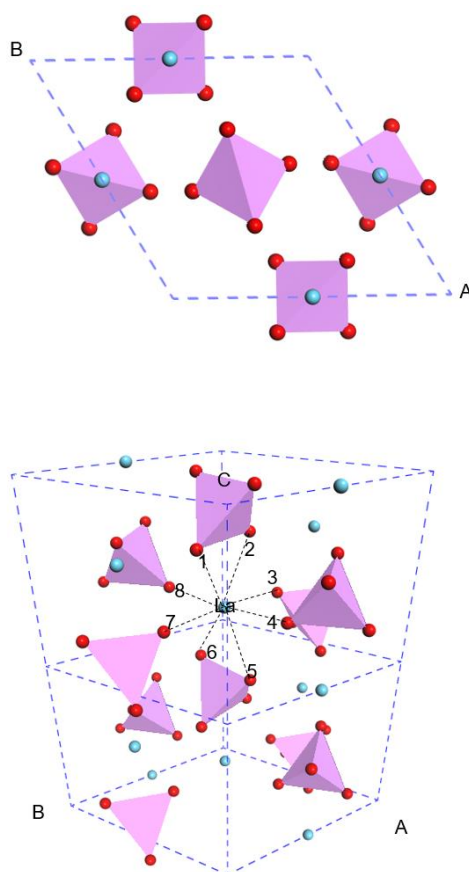


Figure 4.17 Crystal structure of Rhabdophane-type LaPO_4 . The distorted tetrahedra represent PO_4 units, where the corner red atoms are O atoms and P atoms locate inside. La is in blue with eight coordinated O atoms. The top view is shown in top, the perspective side view is shown in bottom.

Two “layers” of the bulk structure are shown in **Figure 4.17**. La atoms are eight-fold coordinated by O atoms which come from eight different PO₄ units. La atom is four-fold coordinated with O along plane perpendicular to c axis with $d(\text{La-O}_{3,4,7,8}) = 2.413\text{\AA}$. Another 4 O atoms generate 2 perpendicular planes, that is O₁-La-O₂ \perp O₅-La-O₆, with a bond length of $d(\text{La-O}_{1,2,5,6}) = 2.572\text{\AA}$.

4.3.3.1 Modelling of Tip facet

According to XRD, it shows that the Tip facet is a (001) facet. We cut the (001) surface based on the bulk crystal structure obtained before. To have a clear view of the surface structure, some characterisations were performed and we can obtain the following information in **Table 4.4**.

Table 4.4 Characterization (XPS) information we obtained on Lateral facet

	Experiments	Information extracted
(1)	No H _n PO ₄ ⁽³⁻ⁿ⁾⁻ signal is found (XPS)	No H ₂ O dissociation
(2)	No excess of phosphorus (XPS)	Tip facet should be stoichiometric
(3)	Both Nd ³⁺ and PO ₄ ³⁻ signals are detected (XPS)	La ³⁺ and PO ₄ ³⁻ are exposed on the surface

The modelling procedure is described as followed. First, the bulk crystal structure was cut into a 2×2 large, 3-layer thick (001) surface. All the possible terminations are modelled including the O-terminated, P-terminated and La-terminated surfaces as shown in **Figure A 4.3.1**, but we discuss only the best results. Then some excess atoms and functions are deleted, at one hand we need to keep the stoichiometry of the surface, at the other hand, the symmetry of the surface is also needed to avoid the polar surfaces. The surface energies of these surfaces are calculated in **Table A 4.3.1**. Several most stable surface structures are selected to adsorb water molecules to see the possibility of the water dissociation on the surface in **Table A 4.3.2**.

The selection of the Tip(001) surface has been done, and the structure of the Tip surface is shown in **Figure 4.18**.

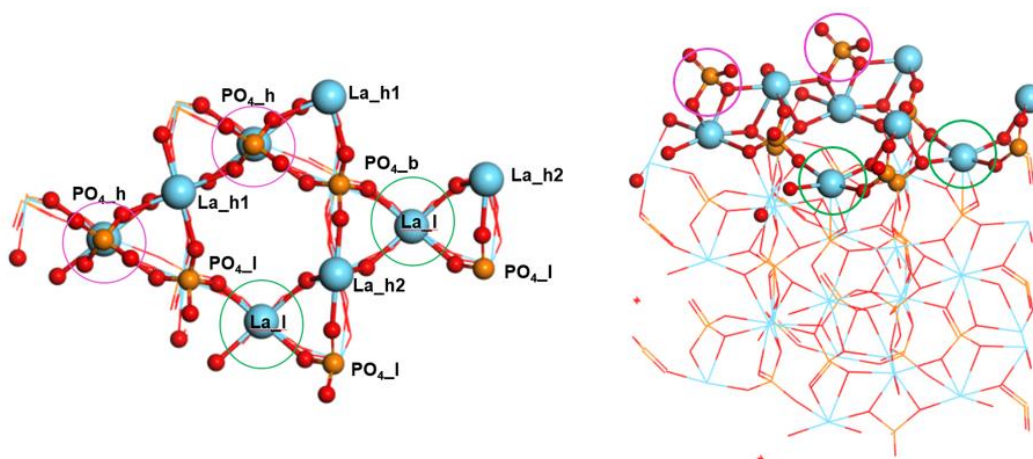


Figure 4.18 The selected Tip(001) facet morphology, two pink circles indicate the position of two PO₄ functional groups and two green circles indicate the position of two La atoms are used both on top view (left) and side view (right) to show clearly the relative positions

The surface we modelled has the following consistency with the experimental characterization as we conclude in [Table 4.4](#): (1) no H_nPO₄⁽³⁻ⁿ⁾⁻ on the surface, the H₂O dissociation is thermodynamically studied on the surface (taking H₂O as a reference, E_{ads}(H₂O)=-2.117 eV, E_{ads}(H+OH)=-0.40 eV), and the molecular adsorption of H₂O is much more favourable than its dissociative adsorption; (2) no excess P element and the surface is stoichiometric; (3) both La³⁺ and PO₄³⁻ elements are exposed on the surface as shown in [Figure 4.18](#). For the following reactivity study, we named the different sites as follows, PO₄_h (the PO₄ groups at higher altitude) and PO₄_l (the PO₄ groups at lower altitude). More different types of La atoms were found due to the deletion of the two PO₄ groups which used to be present above them in the bulk phase. In total we have three different types of La, including La_h1, La_h2 (two types of La atoms at higher altitude) and La_l (the La atoms at lower altitude). On Tip facet, the Lewis acid sites La³⁺ are the most abundant sites followed by the Lewis basic sites PO₄³⁻ groups, and no Bronsted acid sites exist.

4.3.3.2 Modelling of Lateral facet

According to the characterization, we can also obtain the following information in

Table 4.5.

Table 4.5 Characterization (XPS, NMR and Raman) information we obtained on Lateral facet

	Experiments	Information extracted
(1)	$H_nPO_4^{(3-n)-}$ signal is found (XPS)	H_2O dissociation is possible
(2)	Phosphorus element is excessive (XPS)	Lateral facet should be stoichiometric, And P element is more excessive
(3)	The signal of $H_2PO_4^-$ is found (NMR and Raman)	$H_2PO_4^{2-}$ group should be on the surface
(4)	Both Nd^{3+} and PO_4^{3-} signals are detected (XPS)	La^{3+} and PO_4^{3-} are exposed on the surface

There are in total two different Lateral facet phases, the (010) and the (100) surface. Both of them were built and showed to have the same surface structures. So, in the following, only the simulation of (010) surface is shown.

The similar steps were performed as in Tip facet surface modelling. All the possible terminations of the surfaces are shown in [Figure A 4.3.2](#), then several atoms are deleted to keep the symmetry. Considering the excess P in Lateral facet, a La^{3+} atom is removed and as a compensation 3 H^+ are added. Possible positions to accept protons are shown in [Figure 4.19](#).

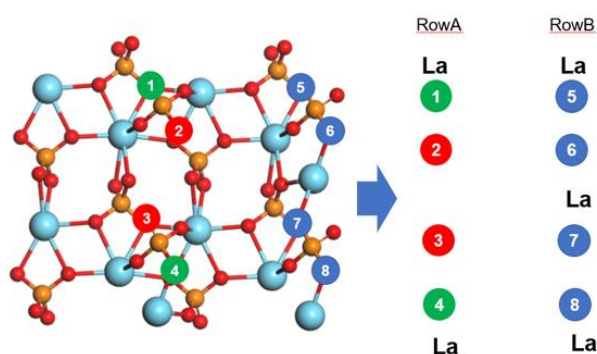


Figure 4.19 Possible positions for protons

In [Figure 4.19](#), we marked the O from 1-8. Different sites are marked with different

colours. The three protons adsorption on PO_4^{3-} obeys the following rules: ① H is always added to the highest O atom, just as the sites we show in **Figure 4.19**; ② The H_2PO_4^- group should be included, that is to say one of the (1,2), (3,4), (5,6) and (7,8) situation should appear; ③ Both the H up (H atom pointing outside the surface) and the H down (H atom pointing inside the surface) cases are tested.

The first test was done on the 3 H atoms added to (123) and (124) position respectively, and the situation of (123) occupied is found to be 1.59eV more stable than (124) occupied case, which is as expected as the position 2 and 3 should be both bonded with protons as they used to be bonded with La^{3+} , which becomes the fourth constrain for our modelling.

According to the restrictions, the position (123), which is equal to position (234), is the best position for protons. Then the configurations of the H are tested. Only the most favourable one is shown in every possibility.

Table 4.6 Possible positions of the additional protons in position (123)

G(123)-G(most stable)/eV			
0 H down	1 H down	2 H down	3 H down
Not stable	+0.24	0.00	Not stable

The most favourable configuration is shown in **Figure 4.20**.

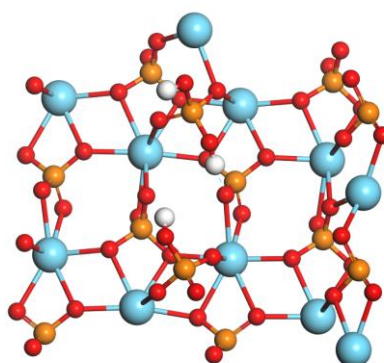


Figure 4.20 The structure of the Lateral(010) facet

As shown in **Figure 4.20**, the most stable and fit best the restriction and descriptions from characterisation should be the one with 2 H in position 2 and 3 pointing inside the surface, and one of the H from H_2PO_4^- generates an H bond with the second layer PO_4^{3-} .

4.3.3.3 Wulff structure of the catalytic morphology

The surface energy of the Tip facet $\Gamma(\text{Tip})$ is easy to get as it is not only symmetric but also stoichiometric. represent

$$\Gamma(\text{Tip}) = \frac{G_{\text{Tip}} - N_{\text{LaPO}_4} G_{\text{bulk}}}{2S} = 0.070 \text{ eV}/\text{\AA}^2$$

$$G_{\text{Tip}} \approx E_{\text{Tip}}^{\text{DFT}}$$

Where Γ represents the surface energy, G_{Tip} represents the Gibbs free energy of the Tip facet, N_{LaPO_4} represents the number of LaPO_4 bulk, and G_{bulk} represents the Gibbs free energy of the bulk, S represents the surface area.

The surface energy of the Lateral facet cannot be directly computed due to its non-stoichiometry. The chemical potential of the extra PO_4^{3-} and H^+ can be expressed by the combination of $(\text{P}_2\text{O}_5)_2$ and H_2O in gas phase.

Using $1/2 (\text{P}_2\text{O}_5)_2$ and $3\text{H}_2\text{O}$:

$$\mu_{(\text{P}_2\text{O}_5)_2}(T, P_{(\text{P}_2\text{O}_5)_2}) = E_{(\text{P}_2\text{O}_5)_2}^{\text{DFT}} + E_{(\text{P}_2\text{O}_5)_2}^{\text{ZPE}} + \Delta\mu_{(\text{P}_2\text{O}_5)_2}(T, P^0) + k_B T \ln\left(\frac{P_{(\text{P}_2\text{O}_5)_2}}{P^0}\right)$$

$$\mu_{\text{H}_2\text{O}}(T, P_{\text{H}_2\text{O}}) = E_{\text{H}_2\text{O}}^{\text{DFT}} + E_{\text{H}_2\text{O}}^{\text{ZPE}} + \Delta\mu_{\text{H}_2\text{O}}(T, P^0) + k_B T \ln\left(\frac{P_{\text{H}_2\text{O}}}{P^0}\right)$$

$$\Gamma(\text{Lateral}) = \frac{G_{\text{Lateral}} - N_{\text{LaPO}_4} G_{\text{bulk}} - N_{(\text{P}_2\text{O}_5)_2} \mu_{(\text{P}_2\text{O}_5)_2}(T, P^0) - N_{\text{H}_2\text{O}} \mu_{\text{H}_2\text{O}}(T, P^0)}{2S}$$

$$= 0.026 \text{ eV}/\text{\AA}^2$$

Where $\mu_{(\text{P}_2\text{O}_5)_2}(T, P^0)$ represents the chemical potential of the $(\text{P}_2\text{O}_5)_2$ in gas phase at standard pressure, both $E_{(\text{P}_2\text{O}_5)_2}^{\text{DFT}}$ and $E_{(\text{P}_2\text{O}_5)_2}^{\text{ZPE}}$ come from the DFT calculation, $\Delta\mu_{(\text{P}_2\text{O}_5)_2}(T, P^0) = -TS$, S is the molecular entropy in gas phase, T is the room temperature. The same treatment is done for H_2O .

The Wulff structure of the LaPO_4 catalyst is shown in **Figure 4.21**. A hexagonal prism is obtained with the surface ratio of the $S_{\text{Tip}(001)}: S_{\text{Lateral}(010)} = 1:4.43$, and the ratio of length : width = 1:2.43, which is in a good consistency with the experimental result 1:3~5 as we mentioned previously, which can be considered as the first validation of our model.

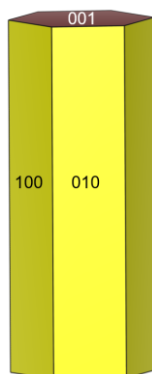


Figure 4.21 The Wulff construction of the LaPO_4 catalyst

In the following IR spectrum simulation, the modelling of the adsorption of CO and C_2H_2 was only done on the Lateral facet due to its larger ratio of surface area compared to the Tip facet.

4.3.4 IR spectrum comparison between experiments and simulation

First, an ab initio thermodynamic calculation is first done in **Figure 4.22** to understand the surface state under the IR spectrum performing condition ($T=77\text{K}$).

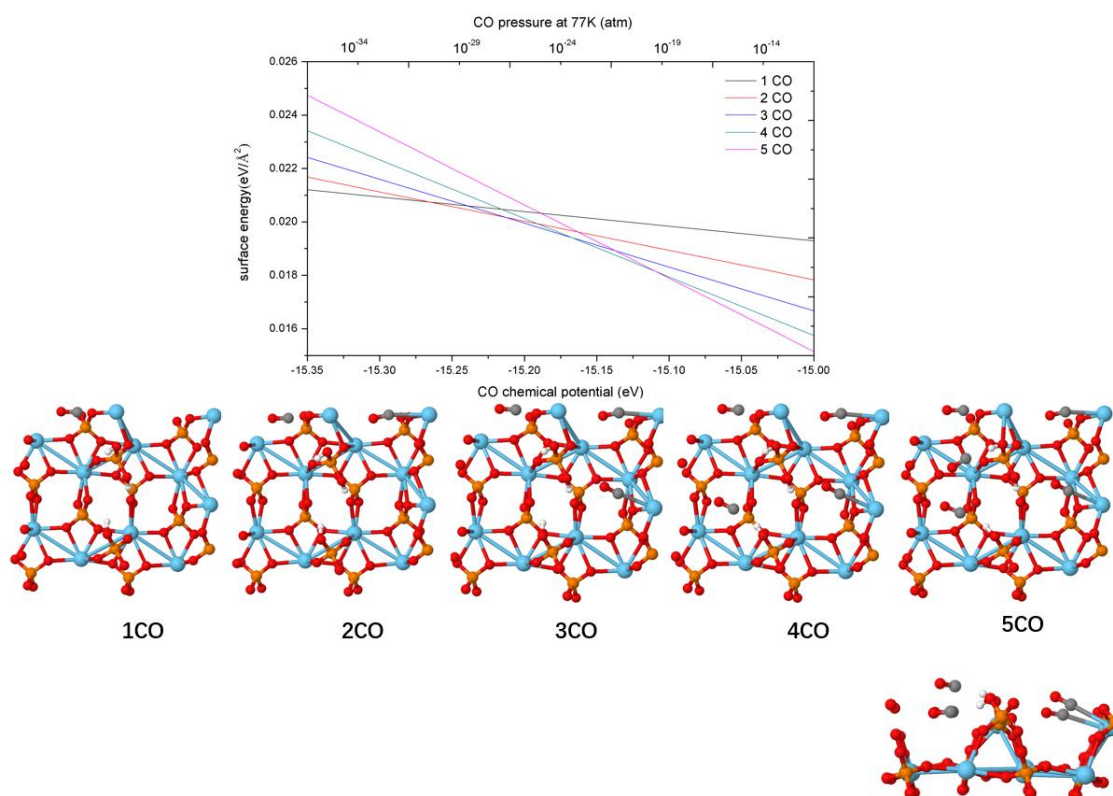


Figure 4.22 An ab initio thermodynamic calculation on CO adsorption on Lateral facet is shown in top, top views of the structures of different numbers of molecular CO adsorption named 1CO ~ 5CO are shown in the middle, the side view of surface 5CO is shown in bottom

As is shown in **Figure 4.22**, the coverage of CO increases from 1~5, C atoms in the CO interact with either the Bronsted acid $H_nPO_4^{-(3-n)}$ or La^{3+} . In total there are 2 H sites and 3 La sites available on the surface, thus up to 5 CO molecules are adsorbed on the surface. According to the ab initio thermodynamic calculation, 5 CO can be adsorbed on the surface when the pressure is higher than 10^{-19} atm, which means in the IR spectroscopy study, using 5CO@surface is reasonable from the thermodynamic point of view. What's more, the more CO molecules using, the more the environmental effects are taken into consideration. Then the frequency calculation was done compared with the wavenumbers from experimental IR spectroscopy in **Figure 4.23** and **Table 4.7**.

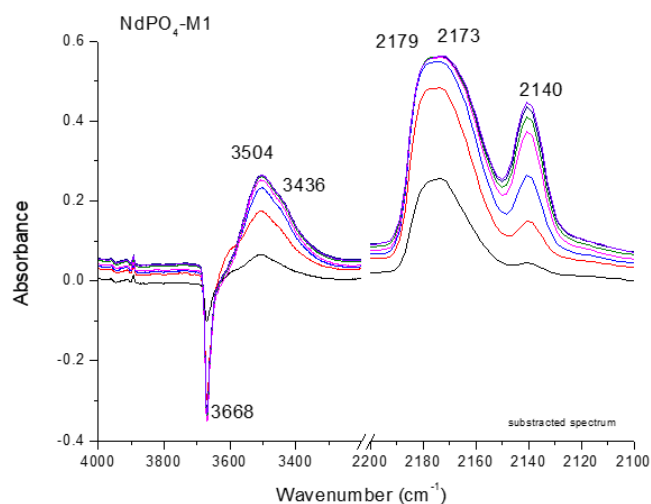


Figure 4.23 Differential IR spectroscopy of CO adsorption on NdPO₄-M1 at 77K

Table 4.7 Comparison of important peaks between experimental (Peak_exp) and theoretical (Peak_dft) IR spectroscopy before and after the CO adsorption, peaks disappear means the signal is negative in the IR and appear means the signal is positive

5CO@surface	Peak_exp/cm ⁻¹	Peak_dft/cm ⁻¹	Peak type
Peaks disappear	3668	3677, 3692	PO ₃ -H, PO ₁ -H
Peaks appear	3504, 3436	3491, 3411	PO ₃ H--CO, PO ₁ H--CO
	2179,2173	2188~2147	C-O
	2140	/	C-O in gas phase

As is shown in Table 4.7 and Figure 4.23, a peak disappears at 3668 cm⁻¹ experimentally after the adsorption of CO and the corresponding peak shows 3677 cm⁻¹ and 3692cm⁻¹ theoretically, which has also been revealed by the previous study²²⁴. This peak represents the O-H vibration both on H₂PO₄⁻ and HPO₄²⁻, which disappears after the interaction with CO. Such interaction contributes to an appearance of the peak around 3500 cm⁻¹, this contribution has also been detected in the CO adsorption in alumina–silicas and has been claimed to be the vibration of O-H species interacting with CO²⁷². Other CO molecules are far away from the protons and directly generate a bond with the

La^{3+} with a C-O vibration of around 2170 cm^{-1} experimentally, consistent with the computed value $2188\sim 2147\text{ cm}^{-1}$. The IR spectrum of CO adsorption is well reproduced by the modelling which validate the surface structure, and also confirm the Bronsted and Lewis acid sites at the same time.

The C_2H_2 molecule can not only interact with basic sites, weak acid sites (through π bonding) but also interact with acido-basic pair with dissociative or non-dissociative adsorption^{273,274}. Thus, the C_2H_2 adsorption at room temperature was also done and characterized. First, the ab initio thermodynamic calculation was also done in Figure 4.24 to figure out the coverage of C_2H_2 in room temperature.

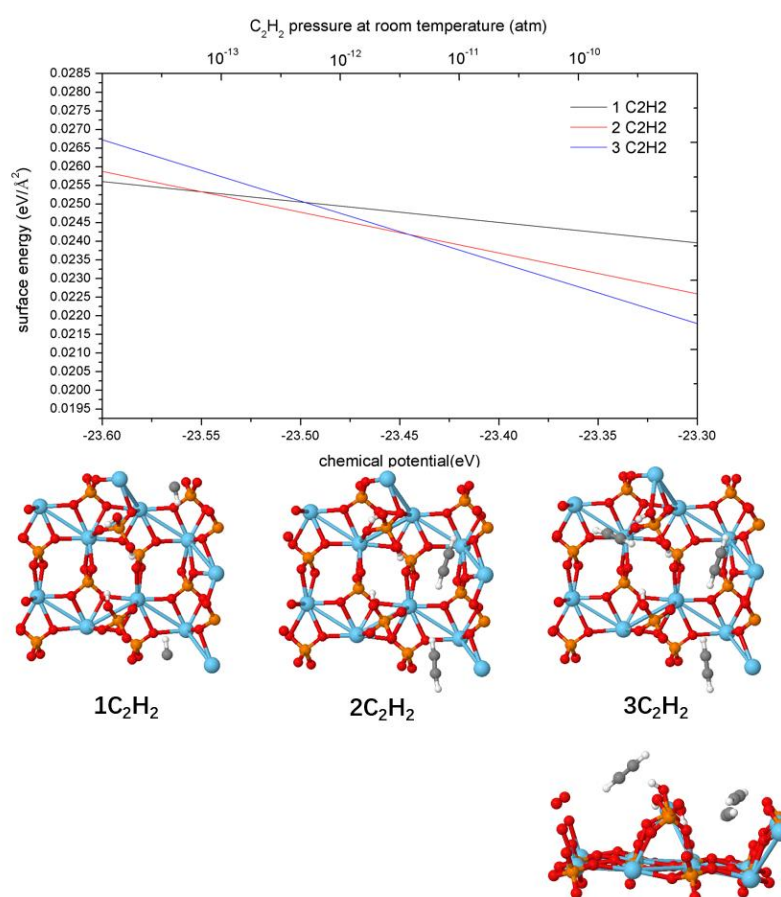


Figure 4.24 An ab initio thermodynamic calculation on C_2H_2 adsorption on Lateral facet is shown in top, top views of the structures of different numbers of molecular C_2H_2 adsorption named 1 $\text{C}_2\text{H}_2 \sim 3\text{C}_2\text{H}_2$ are shown in the middle, the side view of surface $3\text{C}_2\text{H}_2$ is shown in bottom

As shown in **Figure 4.24**, the most stable C_2H_2 molecule is parallel in the “tunnel” like structure and weakly interacts with the La^{3+} site. Such parallel configuration can make the distance between $C\equiv C \cdots La^{3+}$ and the $C-H \cdots OP$ both at a relative short situation, thus shows the property as we mentioned before that C_2H_2 can interact with acido-basic pair. Then the third C_2H_2 is adsorbed close to the Bronsted acid site $H_2PO_4^-$ with a small dihedral angle with the parallel plane. In fact, there exist a more stable structure (0.09 eV more stable than) as shown in **Figure A 4.3.3**, where the third C_2H_2 is also parallel to the surface. However, this configuration cannot reflect the disappearing of the peak around 3668 cm^{-1} (PO-H vibration) as no C_2H_2 is directly interacting with the HOP here, thus, considering their stability are quite close, we still use the second most stable structure as shown in **Figure 4.24**.

Then we show the comparison between the experimental IR spectroscopy and the computed one in **Figure 4.25** and **Table 4.8**.

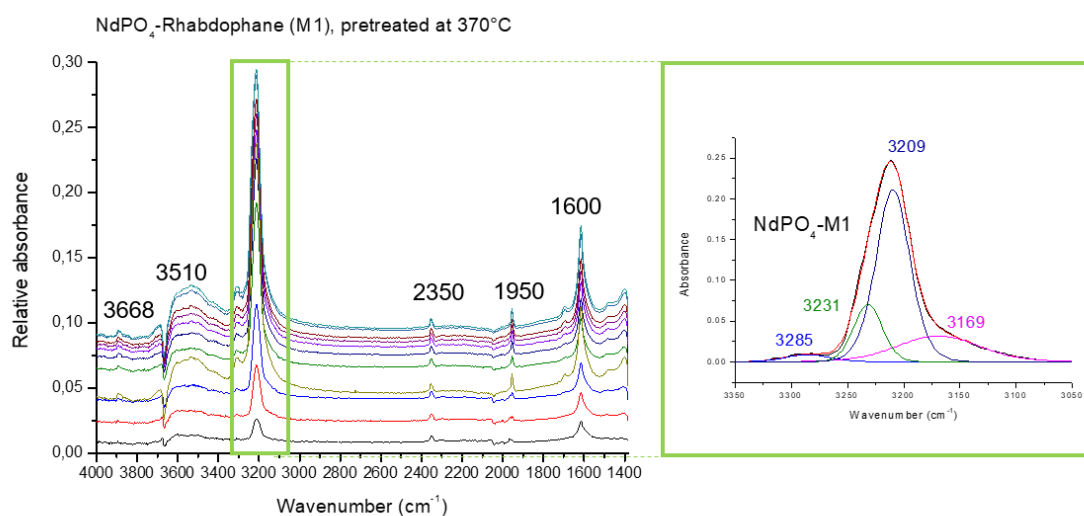


Figure 4.25 Differential IR spectroscopy of CO adsorption on $NdPO_4$ -M1 at 77K

Table 4.8 Comparison of important peaks between experimental and theoretical IR spectroscopy of C₂H₂ adsorption

3C ₂ H ₂ @surface	Peak_exp/cm ⁻¹	Peak_dft/cm ⁻¹	Peak type
Peaks disappear	3668	3692	PO ₁ -H
	3510	3355, 3344	$\begin{array}{c} \text{La} \\ \\ \text{H}-\text{C}\equiv\text{C}-\text{H} \\ \leftarrow \quad \rightarrow \end{array}$
		3343	$\begin{array}{c} \text{HO}_1\text{P} \\ \\ \text{H}-\text{C}\equiv\text{C}-\text{H} \\ \leftarrow \quad \rightarrow \end{array}$
	3285	3266	$\begin{array}{c} \text{La} \\ \\ \text{H}-\text{C}\equiv\text{C}-\text{H} \\ \leftarrow \quad \leftarrow \end{array}$
	3231	3242	$\begin{array}{c} \text{La} \\ \\ \text{H}-\text{C}\equiv\text{C}-\text{H} \\ \leftarrow \quad \leftarrow \end{array}$
Peaks appear	3209	3212	$\begin{array}{c} \text{HO}_1\text{P} \\ \\ \text{H}-\text{C}\equiv\text{C}-\text{H} \\ \leftarrow \quad \leftarrow \end{array}$
	3169	/	
	2350	2500	PO ₂ -H
	1950	1951, 1953, 1956	$\begin{array}{c} \text{La} \qquad \qquad \text{HO}_1\text{P} \\ \qquad \qquad \qquad \\ \text{H}-\text{C}\equiv\text{C}-\text{H} \quad \text{H}-\text{C}\equiv\text{C}-\text{H} \\ \leftarrow \leftarrow \rightarrow \rightarrow \quad \leftarrow \leftarrow \rightarrow \rightarrow \end{array}$
	1600	/	H ₂ O vibration

Not as clear as the IR spectroscopy of CO adsorption, the one for C₂H₂ adsorption is much more complicated due to the more vibration modes of C₂H₂ itself and the symmetric non-symmetric environment caused by surrounding groups. However, there are two peaks that is quite clear, the appearance of the $\begin{array}{c} \leftarrow \leftarrow \rightarrow \rightarrow \\ \text{H}-\text{C}\equiv\text{C}-\text{H} \end{array}$ vibration located at around interacting with either La³⁺ or H₂PO₄⁻ (located at around 1950 cm⁻¹) and the disappearing of the O-H vibration in H₂PO₄⁻ due to the interaction between C₂H₂ and H₂PO₄⁻. There are two peaks that we did not detect from theoretical part, the peak of 3169 cm⁻¹ and the peak of 1600 cm⁻¹. The peak of 1600 cm⁻¹ is easy to tell as it is a normal peak for the water vibration, which means some water molecules either physisorbed

water or exist in the environment. The peak around 3169 cm^{-1} , which may be similar with the peaks in the range of $3212 \sim 3266\text{ cm}^{-1}$ from DFT calculation if we take the possible error in computing wavenumbers into consideration, thus the peak of 3169 cm^{-1} may be the asymmetric C_2H_2 vibration. There is also a peak around the 3510 cm^{-1} experimentally, however, this peak is a bit broad, thus although it is not so close the calculated $\overleftarrow{\text{H}}-\text{C}\equiv\text{C}-\overrightarrow{\text{H}}$ vibration peak (around 3350 cm^{-1}), we still consider this peak is from $\overleftarrow{\text{H}}-\text{C}\equiv\text{C}-\overrightarrow{\text{H}}$ interacting with the acid and weak basic sites on the surface.

Thus, intensity calculation should be done to exclude some noisy peaks so that we can obtain clear IR simulation peaks.

4.3.6 Conclusion

A LaPO_4 modelling was done both on the Lateral facet and the Tip facet on account of the interesting and distinguishing activity properties to the 2,3-BDO dehydration reaction on different facets. The IR spectrum on Lateral was also compared between the experimental one and the simulation one, at one hand, it can be used to validate the surface modelling to obtain more information on the acido-basic sites, on the other hand it is also a validation of the surface modelling. The simulation of the IR spectrum of CO adsorption has a good consistence with the experimental results. However, considering the complexity of the C_2H_2 adsorption, we cannot model the IR results well, with which an intensity calculation is needed to simplify the spectrum.

Appendix 4.3

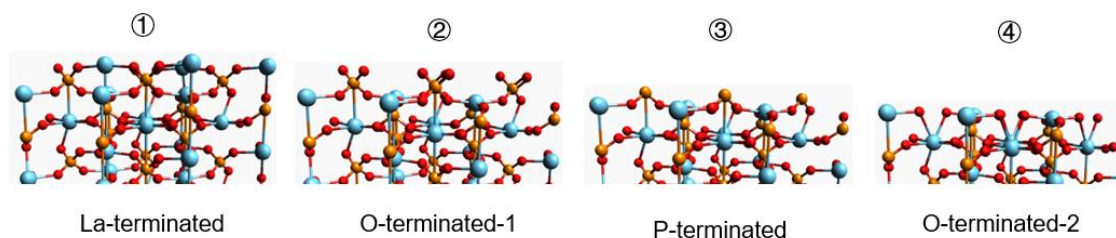
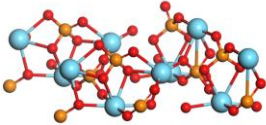
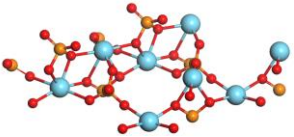
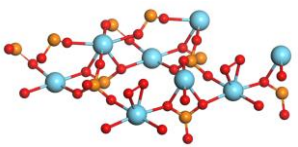


Figure A 4.3.1 Different terminations of Tip(001) surface

Table A 4.3.1 Surface energy of all the symmetric and stoichiometric Tip(001) surface

Surface	Original surface	Surface energy/(eV/Å ²)
	La-terminated	0.071
	O-terminated-1	0.070
	P-terminated	0.095

It is worth noting that only the surface symmetric surface and the surface with La³⁺ and PO₄³⁻ sites are listed here.

The measures are taken from the symmetric surfaces obtained from the Original slab in the second column to the stoichiometry surface.

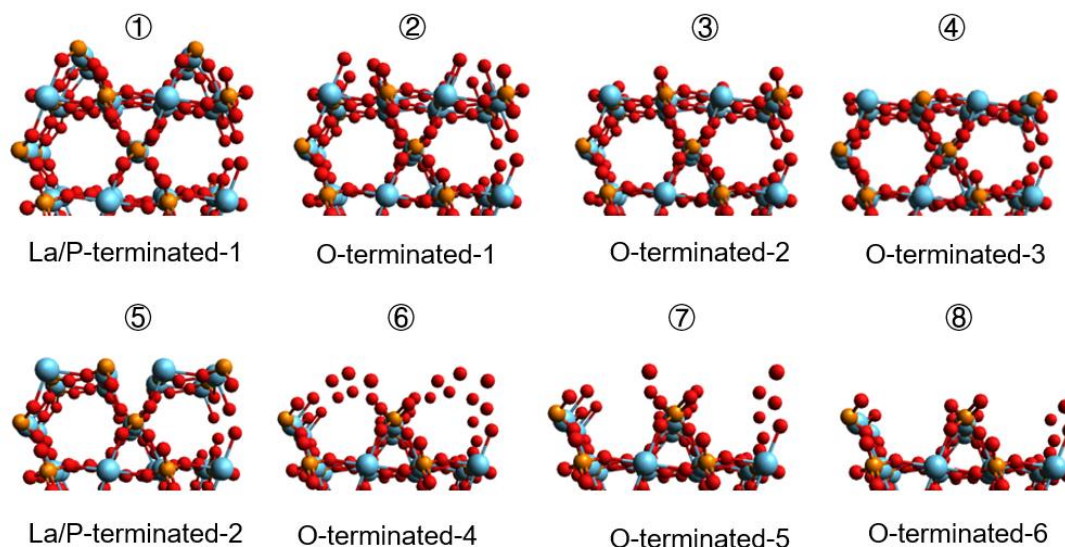
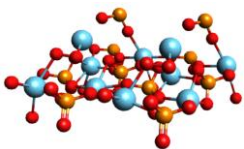
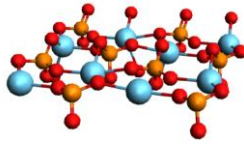
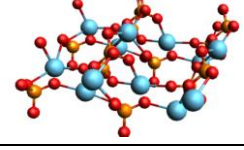


Figure A 4.3.2 Different terminations of Lateral(010)&(100) surface

Table A 4.3.2 Surface energy of all the symmetric Lateral(001)&(100) surface with P elements excessed

Surface	Original surface	Surface energy/(eV/Å ²)
	La/P-terminated-1	0.104
	O-terminated-3	0.033
	O-terminated-6	0.030

The measures are taken from the symmetric surfaces obtained from the Original slab in the second column to the stoichiometry surface.

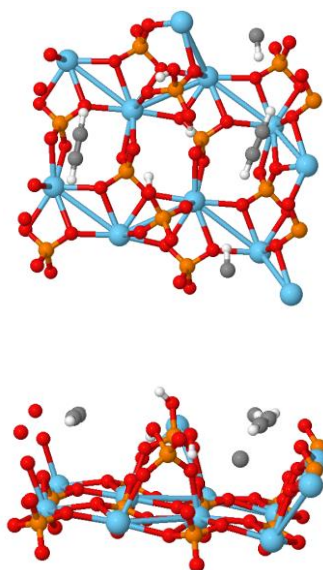


Figure A 4.3.3 The most stable structure of $3\text{C}_2\text{H}_2@\text{surface}$

Chapter 5 Conclusion

In the three-year study, we mainly focused on the biomass reactions on heterogeneous catalysts using computational methods. The surface determination and the reactivity study have been done based on the experimental characterization and reactivity results, which in return the experimental phenomenon was also been better explained from the atomic point of view.

In the computational chemistry, the modeling of heterogeneous catalysis using an atomic description faces the following challenges: (i) the determination of the environment, either the solution environment or the gas phase condition; (ii) describing the interface between the catalytic surface and the environment, which reflects most the adsorption and the desorption processes, and is especially not easy in a solution; (iii) the determination of the catalytic surface especially the structure of the active sites, which is particularly true when the catalyst is known to be an amorphous phase; (iv) the reactivity study on the catalytic surface.

In the first part, we have built a basic model to unravel the role of basic environment in ethanol oxidation and validated the model in a more complicated alcohol AEO on alloy. We have shown that the basic environment can be well described by introducing charges into the catalytic surface, and the role of base is to polarize the surface which modifies the relative stabilities of intermediates adsorbed on the surface. A model combined the micro-solvation and implicit-solvation was used to deal with the interface between

reactants and solid surfaces. Here a micro-solvation model is necessary to be used to better describes the H-bond breaking and generation of the reactants during the adsorption and desorption process, also, a good thermodynamic consistency with experimental data can be obtained compared to the case not using micro-solvation. Then a reactivity study was done on the surface and the transition states were confirmed to unravel the reaction mechanism and view the catalytic issue from the kinetic point of view.

We have two specific examples in the first part. In ethanol oxidation, using the basic model, we know that the basic environment favors the O₂ activation (on Au) and desorption process (both on Au and Pt, especially on Pt). The modeling also reproduced the experimental observations: (i) the O₂ activation is normally considered to be the rate determining step on Au¹²⁰, (ii) the poisoning problem is much more sever on Pt²⁷⁵, (iii) the basic environment improves the activity of the Au and Pt catalysts. Hence, our basic model is validated and provides a general method of modeling the basic environment. The polarization effect from the basic environment can also be substituted by some other methods to avoid the using of base such as alloying³⁶, using electron abundant promoter¹⁶⁹ and a sufficiently high conduction band¹⁷⁰.

In the AEO oxidation, our basic model is used to figure out the alloy effect in the AuCu alloy when the reactions are performed in high pH conditions. The bimetallic model with a small ratio of Cu atoms on the surface has been built based on the fine experimental characterization. It was found that the pure Cu catalysts lacked the ability of breaking α -C-H bond, while the pure Au catalysts came across the difficulty in the adsorption and the activation of H₂O₂ process. Our study shows that the alloy with isolated Cu atoms on the Au abundant surface improves both of the situations we mentioned before and shows a high activity in the AEO oxidation to AECA. It is worth noting that the aggregated Cu atoms should always be avoided here, which explains the advantage of low ratio of Cu in the AuCu bimetallic catalyst. Also, the reactions in neutral

were computed and no reactivity was found in any surface, which shows importance of base in the AEO oxidation. The role of Cu in AuCu alloy raises the importance of the isolated second metal in the alcohol oxidation, which can provide some ideas and simplify the modeling of alloy in the other bimetallic alloys such as AuPt, in which the catalyst is also found to be quite active with small amount of Pt introduced^{34,36}.

Besides the alcohol oxidation, the alcohol dehydration reaction is also key in biomass valorization. Thus, another key point, the dehydration reaction is introduced in the second part, where two different phosphates have been built as the catalysts for the dehydration reactions. The metal phosphate surfaces are much more complicated not only because of its more complex crystal structure compared to metal catalysts, but also comes from its high dependent structure to the environment. Normally an ab initio thermodynamic calculation is needed to confirm the surface structure and molecular coverage. Also, the complexity lies in the possibility of an amorphous surface, in our study, a simplified crystal surface was modeled to represent the amorphous surface and a validation from IR spectrum was simulated in return to confirm the rationality of the simplification.

A calcium phosphate catalyst has been modeled which has been found to be active in the LA dehydration reaction into product AA. A simplified crystal surface under reaction condition instead of an accurate amorphous surface has been confirmed through ab initio thermodynamic and was validated through the following IR spectroscopy modeling. The acido-basic sites, which have a ratio close to 1, were also determined by adsorbing NH₃ and CO₂ molecules. Through the TPD modeling, the similarity of the NH₃ and CO₂-TPD curves was found to be the second layer desorption of NH₃ and the first layer desorption of CO₂. The confirmation of the catalytic surface here, especially the acido-basic sites, provides the foundation for the reactivity study. The consistency between the calculated frequency and the IR spectrum shows the rationality of modeling the amorphous surface using a crystal structure, which provided a simple way of

modeling amorphous surface.

We also investigated the Lanthanum phosphates as the catalysts for the dehydration reaction of 2,3-butanediol. The crystal structure optimization was based on the structure information from various characterization such as XRD, NMR and Raman spectrum. Both the surface structure of the Tip facet and the Lateral facet were determined according to the surface information from the experimental characterization. The characterization results from experimentalists have given us clear picture of the catalytic surface structure through providing the information of surface groups and stoichiometric situation. The effective information exchange between experimental side and theoretical side here gives a general procedure of modeling metal phosphates or metal oxide surfaces.

Our study has opened several perspectives and various possible future tracks to investigate similar systems. However, it still needed to be improved in the modeling of the interface especially between solution and solid catalytic surface, such as the adsorption and desorption process in solution using a more universal method. In fact, our group is developing a method combining DFT and molecular mechanics (MM) to deal with the metal/solvent interface, where the geometrical optimization of the adsorbates is done in the DFT level and the solvent molecules up on the surfaces are handled using MM. In the modeling of metal phosphate, we can conclude a general procedure in the determination of the phosphate surfaces and other metal salt phases. Although the simplified modeling of amorphous surface can already represent many properties of the surface structure, a more accurate amorphous phase modeling is still needed. In fact, a combination of MD and DFT has already been applied in some researches^{240,276}, in which an MD is first used to select the low-energy candidates for the subsequent DFT refinement. The reactivity study will be done in the near future on the determined surfaces. After the reactivity study, a relationship between the acido-basic surface and the active sites can be drawn based on the mechanism, which can be used in design of new catalysts by confirming the catalytic surface first followed by the experimental synthesis.

Bibliography

- 1 James H. Clark, *Green Chem.*, 1999, 1–8.
- 2 https://www.eia.gov/energyexplained/?page=biomass_home.
- 3 A. Pandey, C. R. Soccol, P. Nigam and V. T. Soccol, *Bioresour. Technol.*, 2000, **74**, 69–80.
- 4 H. Fukuda, A. Kond and H. Noda, *J. Biosci. Bioeng.*, 2001, **92**, 405–416.
- 5 D. Li, W. Ni and Z. Hou, *Chinese J. Catal.*, 2017, **38**, 1784–1793.
- 6 T. Werpy and G. Petersen, *Top Value Added Chem. from Biomass*, 2004, 76.
- 7 J. J. Bozell and G. R. Petersen, *Green Chem.*, 2010, **12**, 539–554.
- 8 M. J. Climent, A. Corma and S. Iborra, *Green Chem.*, 2014, **16**, 516–547.
- 9 A. K. Chandel, S. S. da Silva, W. Carvalho and O. V Singh, *J. Chem. Technol. Biotechnol.*, 2012, 87, 11–20.
- 10 M. S. Ide, D. D. Falcone and R. J. Davis, *J. Catal.*, 2014, **311**, 295–305.
- 11 S. Chibani, C. Michel, F. Delbecq, C. Pinel and M. Besson, *Catal. Sci. Technol.*, 2013, **3**, 339–350.
- 12 D. Tongsakul, S. Nishimura and K. Ebitani, *J. Phys. Chem. C*, 2014, **118**, 11723–11730.
- 13 S. Carrettin, P. McMorn, P. Johnston, K. Griffin, C. J. Kiely and G. J. Hutchings, *Phys. Chem. Chem. Phys.*, 2003, **5**, 1329–1336.
- 14 T. Mallat and A. Baiker, *Catal. Today*, 1994, **19**, 247–284.
- 15 T. Gao, T. Gao, W. Fang and Q. Cao, *Mol. Catal.*, 2017, **439**, 171–179.

- 16 A. Villa, N. Dimitratos, C. E. Chan-Thaw, C. Hammond, L. Prati and G. J. Hutchings, *Acc. Chem. Res.*, 2015, **48**, 1403–1412.
- 17 M. Alhumaimess, Z. Lin, W. Weng, N. Dimitratos, N. F. Dummer, S. H. Taylor, J. K. Bartley, C. J. Kiely and G. J. Hutchings, *ChemSusChem*, 2012, **5**, 125–131.
- 18 J. Sha, E. J. Zheng, W. J. Zhou, A. Liebens and M. Pera-Titus, *J. Catal.*, 2016, **337**, 199–207.
- 19 E. M. de Moura, M. A. S. Garcia, R. V Gonçalves, P. K. Kiyohara, R. F. Jardim and L. M. Rossi, *RSC Adv.*, 2015, **5**, 15035–15041.
- 20 K. Patrícia R. Castro, M. Aurélio S. Garcia, W. C. de Abreu, S. Anderson A. de Sousa, C. Verônica R. de Moura, J. Cláudio S. Costa and E. M. de Moura, *Catalysts*, 2018, **8**, 83.
- 21 C. Shang and Z. P. Liu, *J. Am. Chem. Soc.*, 2011, **133**, 9938–9947.
- 22 N. Bogdanchikova, I. Tuzovskaya, L. Prati, A. Villa, A. Pestryakov and M. Farias, *Curr. Org. Synth.*, 2017, **14**, 377–382.
- 23 A. Villa, S. Campisi, K. M. H. Mohammed, N. Dimitratos, F. Vindigni, M. Manzoli, W. Jones, M. Bowker, G. J. Hutchings and L. Prati, *Catal. Sci. Technol.*, 2015, **5**, 1126–1132.
- 24 C. P. Ferraz, M. A. S. Garcia, É. Teixeira-Neto and L. M. Rossi, *RSC Adv.*, 2016, **6**, 25279–25285.
- 25 S. Carretin, P. McMorn, P. Johnston, K. Griffin, C. J. Kiely, G. A. Attard and G. J. Hutchings, *Top. Catal.*, 2004, **27**, 131–136.
- 26 T. Pasini, M. Piccinini, M. Blosi, R. Bonelli, S. Albonetti, N. Dimitratos, J. A. Lopez-Sanchez, M. Sankar, Q. He, C. J. Kiely, G. J. Hutchings and F. Cavani, *Green Chem.*, 2011, **13**, 2091.
- 27 D. I. Enache, D. Barker, J. K. Edwards, S. H. Taylor, D. W. Knight, A. F. Carley and G. J. Hutchings, *Catal. Today*, 2007, **122**, 407–411.
- 28 N. Dimitratos, A. Villa, D. Wang, F. Porta, D. Su and L. Prati, *J. Catal.*, 2006, **244**, 113–121.

- 29 I. Gandarias, P. J. Miedziak, E. Nowicka, M. Douthwaite, D. J. Morgan, G. J. Hutchings and S. H. Taylor, *ChemSusChem*, 2015, **8**, 473–480.
- 30 M. Khawaji and D. Chadwick, *ChemCatChem*, 2017, **9**, 4353–4363.
- 31 P. Miedziak, M. Sankar, N. Dimitratos, J. A. Lopez-Sanchez, A. F. Carley, D. W. Knight, S. H. Taylor, C. J. Kiely and G. J. Hutchings, in *Catalysis Today*, Elsevier B.V., 2011, vol. 164, pp. 315–319.
- 32 N. Dimitratos, J. A. Lopez-Sanchez, J. M. Anthonykuty, G. Brett, A. F. Carley, R. C. Tiruvalam, A. A. Herzing, C. J. Kiely, D. W. Knight and G. J. Hutchings, *Phys. Chem. Chem. Phys.*, 2009, **11**, 4952.
- 33 S. Marx, A. Baiker, *J. Phys. Chem. C*, 2009, **113**, 6191–6201.
- 34 K. Heidkamp, M. Aytimir, K. Vorlop and U. Prüße, *Catal. Sci. Technol.*, 2013, **3**, 2984.
- 35 Y. Shen, Y. Li and H. Liu, *J. Energy Chem.*, 2015, **24**, 669–673.
- 36 A. Villa, A. Jouve, F. Sanchez Trujillo, D. Motta, L. Prati and N. Dimitratos, *Catalysts*, 2018, **8**, 54.
- 37 I. Sobczak and Ł. Wolski, *Catal. Today*, 2015, **254**, 72–82.
- 38 T. Pasini, M. Piccinini, M. Blosi, R. Bonelli, S. Albonetti, N. Dimitratos, J. A. Lopez-Sanchez, M. Sankar, Q. He, C. J. Kiely, G. J. Hutchings and F. Cavani, *Green Chem.*, 2011, **13**, 2091–2099.
- 39 S. Albonetti, T. Pasini, A. Lolli, M. Blosi, M. Piccinini, N. Dimitratos, J. A. Lopez-Sanchez, D. J. Morgan, A. F. Carley, G. J. Hutchings and F. Cavani, *Catal. Today*, 2012, **195**, 120–126.
- 40 W. Li, A. Wang, X. Liu and T. Zhang, *Appl. Catal. A Gen.*, 2012, **433–434**, 146–151.
- 41 C. Zhang, T. Wang, X. Liu and Y. Ding, *J. Mol. Catal. A Chem.*, 2016, **424**, 91–97.
- 42 D. Liang, J. Gao, J. Wang, P. Chen, Y. Wei and Z. Hou, *Catal. Commun.*, 2011, **12**, 1059–1062.

- 43 J. Kärger and S. Vasenkov, *Microporous Mesoporous Mater.*, 2005, **85**, 195–206.
- 44 T. Mallat, A. Baiker and L. Botz, *Appl. Catal. A Gen.*, 1992, **86**, 147–163.
- 45 N. López, N. Almora-Barrios, G. Carchini, P. Błoński, L. Bellarosa, R. García-Muelas, G. Novell-Leruth and M. García-Mota, *Catal. Sci. Technol.*, 2012, **2**, 2405–2417.
- 46 M. Besson, P. Gallezot and C. Pinel, *Chem. Rev.*, 2014, 114, 1827–1870.
- 47 S. R. Collinson and W. Thielemans, *Coord. Chem. Rev.*, 2010, **254**, 1854–1870.
- 48 B. M. E. Russbuedt and W. F. Hoelderich, *J. Catal.*, 2010, **271**, 290–304.
- 49 D. Tsukamoto, S. Sakami, M. Ito, K. Yamada and T. Yonehara, *Chem. Lett.*, 2016, 831–833.
- 50 E. Blanco, P. Delichere, J. M. M. Millet and S. Loridant, *Catal. Today*, 2014, **226**, 185–191.
- 51 H. Xu, Z. Miao, H. Zhao, J. Yang, J. Zhao, H. Song, N. Liang and L. Chou, *Fuel*, 2015, **145**, 234–240.
- 52 A. Dosen and R. F. Giese, *Am. Mineral.*, 2011, **96**, 368–373.
- 53 P. Sudarsanam, E. Peeters, E. V Makshina, V. I. Parvulescu and B. F. Sels, *Chem. Soc. Rev.*, 2019, DOI:10.1039/C8CS00452H.
- 54 Y. Zhang, J. Wang, J. Ren, X. Liu, X. Li, Y. Xia, G. Lu and Y. Wang, *Catal. Sci. Technol.*, 2012, **2**, 2485–2491.
- 55 K. Reuter and M. Scheffler, *Phys. Rev. B*, 2001, **65**, 035406.
- 56 M. Piumetti and N. Lygeros, *Chim. Oggi/Chemistry Today*, 2013, **31**, 48–52.
- 57 X. Yang, X. Wang, C. Liang, W. Su, C. Wang, Z. Feng, C. Li and J. Qiu, *Catal. Commun.*, 2008, **9**, 2278–2281.
- 58 S. M. Tembe, G. Patrick and M. S. Scurrrell, *Gold Bull.*, 2009, **42**, 321–327.
- 59 D. Muçoz-santiburcio, M. F. Camellone and D. Marx, 2018, 3327–3331.
- 60 G. Dodekatos, L. Abis, S. J. Freakley, H. Tüysüz and G. J. Hutchings, *ChemCatChem*, 2018, **10**, 1351–1359.
- 61 K. Yamaguchi and N. Mizuno, *Chem. - A Eur. J.*, 2003, **9**, 4353–4361.

- 62 G. M. Mullen, E. J. Evans Jr., I. Sabzevari, B. E. Long, K. Alhazmi, B. D. Chandler and C. B. Mullins, *ACS Catal.*, 2017, **7**, 1216–1226.
- 63 H. J. Freund, *Top. Catal.*, 2008, **48**, 137–144.
- 64 S. Diallo-garcia, M. Ben Osman, S. Casale, C. Thomas, J. Kubo and G. Costentin, *J. Phys. Chem. C*, 2014, **118**, 12744–12757.
- 65 M. Digne, P. Sautet, P. Raybaud, P. Euzen and H. Toulhoat, *J. Catal.*, 2004, **226**, 54–68.
- 66 L. H. Thomas, *Math. Proc. Cambridge Philos. Soc.*, 1927, **23**, 542.
- 67 E. X. Superzeure and E. X. Superieure, *Phys. Rev.*, , DOI:10.1103/PhysRev.136.B864.
- 68 W. Kohn and L. J. Sham, *Phys. Rev.*, 140. 4A, A1133
- 69 J. P. Perdew, K. Burke and M. Ernzerhof, *Phys. Rev. Lett.*, 1996, **78**, 1396–1396.
- 70 B. Hammer and J. K. Norskov, *Adv. Catal.*, 2000, **45**, 71–129.
- 71 J. P. Perdew and Y. Wang, *Sustain. Impact Assess. L. Use Chang.*, 1992, **45**, 13244–13249.
- 72 A. D. Becke, *J. Chem. Phys.*, 1993, **98**, 5648–5652.
- 73 J. Klimeš, D. R. Bowler and A. Michaelides, *J. Phys. Condens. Matter*, 2009, **22**, 2, 022201
- 74 Y. Zhang and W. Yang, *Phys. Rev. Lett.*, 1998, **80**, 890.
- 75 S. Grimme, *J. Comput. Chem.*, 2006, **27**, 1787–1799.
- 76 S. Grimme, J. Antony, S. Ehrlich and H. Krieg, *J. Chem. Phys.*, 2010, **132**, 154104
- 77 S. N. Steinmann and C. Corminboeuf, *J. Chem. Phys.*, 2011, **134**, 10–15.
- 78 S. Gautier, S. N. Steinmann, C. Michel, P. Fleurat-Lessard and P. Sautet, *Phys. Chem. Chem. Phys.*, 2015, **17**, 28921–28930.
- 79 E. Mete, M. Yortanli and M. F. Danişman, *Phys. Chem. Chem. Phys.*, 2017, **19**, 13756–13766.
- 80 Q. Guo and F. Li, *Phys. Chem. Chem. Phys.*, 2014, **16**, 19074–19090.
- 81 D. G. Kresse, Joubert, *Phys. Rev. B - Condens. Matter Mater. Phys.*, 1999, **59**,

- 1758–1775.
- 82 D. A. McQuarrie and J. D. Simon, Eds., *Physical Chemistry: A Molecular Approach*, Sausalito, Calif. : University Science Books, 1997.
- 83 H.-X. Zhou and M. K. Gilson, *Chem. Rev.*, 2009, **109**, 4092–4107.
- 84 D. H. Wertz, *J. Am. Chem. Soc.*, 1980, **102**, 5316–5322.
- 85 P. Wang, S. N. Steinmann, G. Fu, C. Michel and P. Sautet, *ACS Catal.*, 2017, **7**, 1955–1959.
- 86 S. N. Steinmann, C. Michel, R. Schwiedernoch and P. Sautet, *Phys. Chem. Chem. Phys.*, 2015, **17**, 13949–13963.
- 87 D. D. Wagman, J. D. Cox and V. A. Medvedev, *Key Values for Thermodynamics*, Hemisphere Publishing Corp., New York, 1984.
- 88 Q. Meng, Y. Shen, J. Xu and J. Gong, *Chinese J. Catal.*, 2012, **33**, 407–415.
- 89 Q. Meng, Y. Shen, J. Xu, X. Ma and J. Gong, *Surf. Sci.*, 2012, **606**, 1608–1617.
- 90 J. Ho and M. L. Coote, *Theor. Chem. Acc.*, 2009, **125**, 3–21.
- 91 B. Thapa and H. B. Schlegel, *J. Phys. Chem. A*, 2017, **121**, 4698–4706.
- 92 C. C. Chambers, G. D. Hawkins, C. J. Cramer and D. G. Truhlar, *J. Phys. Chem.*, 1996, **100**, 16385–16398.
- 93 V. S. Bryantsev, M. S. Diallo and W. A. Goddard, *J. Phys. Chem. B*, 2008, **112**, 9709–9719.
- 94 C. P. Kelly, C. J. Cramer and D. G. Truhlar, *J. Phys. Chem. B*, 2007, **111**, 408–422.
- 95 C. P. Kelly, C. J. Cramer and D. G. Truhlar, *J. Phys. Chem. B*, 2006, **110**, 16066–16081.
- 96 J. R. Pliego and J. M. Riveros, *J. Phys. Chem. A*, 2001, **105**, 7241–7247.
- 97 M. V Fedotova and S. E. Kruchinin, *J. Mol. Liq.*, 2011, **164**, 201–206.
- 98 C. G. Zhan and D. A. Dixon, *J. Phys. Chem. A*, 2002, **106**, 9737–9744.
- 99 H.-J. Bittrich, *Zeitschrift für Phys. Chemie*, 2011, **176**, 130–130.
- 100 J. R. Pliego and J. M. Riveros, *Chem. Phys. Lett.*, 2000, **332**, 597–602.

- 101 C. Hammaecher and J. F. Paul, *J. Catal.*, 2013, **300**, 174–182.
- 102 F. S. Souza, M. J. S. Matos, B. R. L. Galvão, A. F. C. Arapiraca, S. N. da Silva and I. P. Pinheiro, *Chem. Phys. Lett.*, 2019, **714**, 143–148.
- 103 C. J. Pursell, H. Hartshorn, T. Ward, B. D. Chandler and F. Boccuzzi, *J. Phys. Chem. C*, 2011, **115**, 23880–23892.
- 104 K. Li, Y. Zheng, X. Liang, L. Li, L. Liu and X. Chen, *J. Mol. Model.*, 2018, **24**, 41–44.
- 105 S. Monti, A. C. T. Van Duin, S. Y. Kim and V. Barone, *J. Phys. Chem. C*, 2012, **116**, 5141–5150.
- 106 B. N. Zope, D. D. Hibbitts, M. Neurock and R. J. Davis, *Science.*, 2010, **330**, 74–78.
- 107 H.-V. Tran, H. A. Doan, B. D. Chandler and L. C. Grabow, *Curr. Opin. Chem. Eng.*, 2016, **13**, 100–108.
- 108 C.-R. Chang, X.-F. Yang, B. Long and J. Li, *ACS Catal.*, 2013, **3**, 1693–1699.
- 109 A. A. Koverga, S. Frank and M. T. M. Koper, *Electrochim. Acta*, 2013, **101**, 244–253.
- 110 J. Li, W. Liu, X. Wu and X. Gao, *Biomaterials*, 2015, **48**, 37–44.
- 111 D. D. Hibbitts and M. Neurock, *J. Catal.*, 2013, **299**, 261–271.
- 112 K. Reuter, in *Springer Series in Chemical Physics*, Springer US, 2017, vol. 114, pp. 541–563.
- 113 D. R. Stull and H. Prophet, Eds., *JANAF Thermochemical Tables*, .
- 114 C. Bianchi, F. Porta, L. Prati and M. Rossi, *Top. Catal.*, 2000, **13**, 231–236.
- 115 M. Besson and P. Gallezot, *Catal. Today*, 2000, **57**, 127–141.
- 116 D. I. Enache, J. K. Edwards, P. Landon, B. Solsona-espriu, A. F. Carley, A. A. Herzing, M. Watanabe, C. J. Kiely, D. W. Knight and G. J. Hutchings, *Science*, 2006, **311**, 362–366.
- 117 C. Della Pina, E. Falletta and M. Rossi, *J. Catal.*, 2008, **260**, 384–386.
- 118 I. Kaskow, P. Decyk and I. Sobczak, *Appl. Surf. Sci.*, 2018, **444**, 197–207.

- 119 M. Hayashi, K. Yamada, S. Z. Nakayama, H. Hayashi and S. Yamazaki, *Green Chem.*, 2000, **2**, 257–260.
- 120 G. M. Mullen, J. Gong, T. Yan, M. Pan and C. B. Mullins, *Top. Catal.*, 2013, **56**, 1499–1511.
- 121 C. Chang, B. Long, X. Yang and J. Li, *J. Phys. Chem. C*, 2015, **119**, 16072–16081.
- 122 C. R. Chang, Z. Q. Huang and J. Li, *Nano Res.*, 2015, **8**, 3737–3748.
- 123 J. Saavedra, H. A. Doan, C. J. Pursell, L. C. Grabow and B. D. Chandler, *Science (80-.)*, 2014, **345**, 1599–1602.
- 124 T. Fujitani, I. Nakamura and M. Haruta, *Catal. Letters*, 2014, **144**, 1475–1486.
- 125 X. Shen, W. Liu, X. Gao, Z. Lu, X. Wu and X. Gao, *J. Am. Chem. Soc.*, 2015, **137**, 15882–15891.
- 126 C.-R. Chang, Z.-Q. Huang and J. Li, *WILEY Interdiscip. Rev. Mol. Sci.*, 2016, **6**, 679–693.
- 127 J. Liu, X. Cao and P. Hu, *Phys. Chem. Chem. Phys.*, 2014, **16**, 4176.
- 128 D. Muñoz-Santiburcio, M. Farnesi Camellone and D. Marx, *Angew. Chemie - Int. Ed.*, 2018, **57**, 3327–3331.
- 129 M. Okumura, Y. Kitagawa, M. Haruta and K. Yamaguchi, *Chem. Phys. Lett.*, 2001, **346**, 163–168.
- 130 S. K. Iyemperumal and N. A. Deskins, *CHEMPHYSCHEM*, 2017, **18**, 2171–2190.
- 131 Y. Gao and X. C. Zeng, *ACS Catal.*, 2012, **2**, 2614–2621.
- 132 W. C. Ketchie, M. Murayama and R. J. Davis, *Top. Catal.*, 2007, **44**, 307–317.
- 133 S. Biella, L. Prati and M. Rossi, *J. Mol. Catal. A Chem.*, 2003, **197**, 207–212.
- 134 A. Abad, A. Corma and H. García, *Chem. - A Eur. J.*, 2008, **14**, 212–222.
- 135 M. Conte, H. Miyamura and V. Chechik, *JACS*, 2009, 7189–7196.
- 136 A. Lackmann, C. Mahr, M. Schowalter, L. Fitzek, J. Weissmueller, A. Rosenauer and A. Wittstock, *J. Catal.*, 2017, **353**, 99–106.
- 137 Y. Sun, X. Li, J. Wang, W. Ning, J. Fu, X. Lu and Z. Hou, *Appl. Catal. B Environ.*, 2017, **218**, 538–544.

- 138 T. Mallat, T. Mallat, A. Baiker and A. Baiker, *Chem. Rev.*, 2004, **104**, 3037–3058.
- 139 V. R. Gangwal, J. Van Der Schaaf, B. F. M. Kuster and J. C. Schouten, *J. Catal.*, 2005, **229**, 389–403.
- 140 J. Xie, P. Duan, N. Kaylor, K. Yin, B. Huang, K. Schmidt-Rohr and R. J. Davis, *ACS Catal.*, 2017, **7**, 6745–6756.
- 141 M. Haruta, T. Kobayashi, H. Sano and N. Yamada, *Chem. Lett.*, 1987, **16**, 405–408.
- 142 P. A. Sermon, P. B. Wells, D. A. Buchanan, G. Webb and G. C. Bond, *J. Chem. Soc. Chem. Commun.*, 1973, 444–445.
- 143 C. Bond and B. Wells, *J. Chem. Soc. Faraday Trans. 1*, 1977, **1**, 385–394.
- 144 M. Haruta, N. Yamada, T. Kobayashi and S. Iijima, *J. Catal.*, 1989, **115**, 301–309.
- 145 L. Prati and M. Rossi, *J. Catal.*, 1998, **176**, 552–560.
- 146 M. R. S. Biella, G.L. Castiglioni, C Fumagalli, L. Prati, *Catal. Today*, 2002, **72**, 43–49.
- 147 S. E. Davis, M. S. Ide and R. J. Davis, *Green Chem.*, 2013, **15**, 17–45.
- 148 D. Shi, J. Liu and S. Ji, *Ind. Eng. Chem. Res.*, 2017, **56**, 11028–11033.
- 149 P. Liu and J. K. Nørskov, *Phys. Chem. Chem. Phys.*, 2001, **3**, 3814–3818.
- 150 D. Yuan, X. Gong and R. Wu, *J. Chem. Phys.*, 2008, **128**, 064706.
- 151 F. J. Morales-Leal, J. Rivera De la Rosa, C. J. Lucio-Ortiz, D. Bustos Martínez, D. A. De Haro Del Rio, M. A. Garza-Navarro, D. X. Martínez-Vargas and C. D. Garcia, *Appl. Catal. A Gen.*, 2018, **562**, 184–197.
- 152 J. N. Chheda, G. W. Huber and J. A. Dumesic, *Angew. Chemie - Int. Ed.*, 2007, **46**, 7164–7183.
- 153 R. Anderson, K. Griffin, P. Johnston and P. L. Alsters, *Adv. Synth. Catal.*, 2003, **345**, 517–523.
- 154 S. Chibani, C. Michel, C. Pinel and V. A. Online, *Catal. Sci. Technol.*, 2013, **3**, 339–350.
- 155 H.-V. Tran, H. A. Doan, B. D. Chandler and L. C. Grabow, *Curr. Opin. Chem.*

- Eng.*, 2016, **13**, 100–108.
- 156 G. Kresse and J. Furthmüller, *Phys. Rev. B - Condens. Matter Mater. Phys.*, 1996, **54**, 11169–11186.
- 157 G. Kresse and J. Furthmüller, *Comput. Mater. Sci.*, 1996, **6**, 15–50.
- 158 G. Kresse and J. Hafner, *Phys. Rev. B*, 1993, **47**, 558–561.
- 159 D. R. Lide, *Handb. Chem. Phys.*, 2003, **53**, 2616.
- 160 K. Letchworth-Weaver and T. A. Arias, *Phys. Rev. B - Condens. Matter Mater. Phys.*, 2012, **86**, 1–16.
- 161 D. Gunceler, K. Letchworth-Weaver, R. Sundararaman, K. A. Schwarz and T. A. Arias, *Model. Simul. Mater. Sci. Eng.*, 2013, **21**, 074005.
- 162 K. Mathew, R. Sundararaman, K. Letchworth-Weaver, T. A. Arias and R. G. Hennig, *J. Chem. Phys.*, 2014, **140**, 084106
- 163 G. Henkelman, B. P. Uberuaga and H. Jónsson, *J. Chem. Phys.*, 2000, **113**, 9901–9904.
- 164 S. Kozuch and S. Shaik, *Acc. Chem. Res.*, 2011, **44**, 101–110.
- 165 K. Mathew and R. G. Hennig, 2016, 1–6. arXiv:1601.03346.
- 166 S. Karanjit, K. Bobuatong, R. Fukuda, M. Ehara and H. Sakurai, *Int. J. Quantum Chem.*, 2013, **113**, 428–436.
- 167 M. Sankar, N. Dimitratos, P. J. Miedziak, P. P. Wells, C. J. Kiely and G. J. Hutchings, *Chem. Soc. Rev.*, 2012, **41**, 8099.
- 168 W. Hu, D. Li, Y. Yang, T. Li, H. Chen and P. Liu, *J. Catal.*, 2018, **357**, 108–117.
- 169 Y. Song, X. Chu, Y. Lin and X. Yang, *Journal of Chemistry*. 2012.
- 170 S. I. Naya, M. Teranishi, R. Aoki and H. Tada, *J. Phys. Chem. C*, 2016, **120**, 12440–12445.
- 171 N. K. Gupta, S. Nishimura, A. Takagaki and K. Ebitani, *Green Chem.*, 2011, **13**, 824.
- 172 B. N. Zope, D. D. Hibbitts, M. Neurock and R. J. Davis, *Science*, 2010, **330**, 74–78.

- 173 M. S. Ide and R. J. Davis, *Acc. Chem. Res.*, 2014, **47**, 825–833.
- 174 W. W. Schmidt, D. R. Durante, R. Gingell and J. W. Harbell, *JAOCS, J. Am. Oil Chem. Soc.*, 1997, **74**, 25–31.
- 175 R. von Wandruszka, in *Nonionic Surfactants: Organic Chemistry, Surfactant Science Series*, Marcel Dekker, 1998, vol. 72, pp. 7398–7398.
- 176 K. L. Smith and J. Wiley, US5162579.
- 177 S. Zlatanov, K. Laskaridis and A. Sagredos, *Grasas y Aceites*, 2009, **60**, 360–366.
- 178 D. Yuan, X. Gong and R. Wu, *Phys. Rev. B - Condens. Matter Mater. Phys.*, 2007, **75**, 3–6.
- 179 D. Wang, A. Villa, F. Porta, L. Prati and D. Su, *J. Phys. Chem. C*, 2008, **112**, 8617–8622.
- 180 A. M. Ruppert, M. Jędrzejczyk, N. Potrzebowska, K. Kaźmierczak, M. Brzezińska, O. Sneká-Płatek, P. Sautet, N. Keller, C. Michel and J. Grams, *Catal. Sci. Technol.*, 2018, **8**, 4318–4331.
- 181 C. L. Bracey, P. R. Ellis and G. J. Hutchings, *Chem. Soc. Rev.*, 2009, **38**, 2231–2243.
- 182 A. Sandoval, C. Louis and R. Zanella, *Appl. Catal. B Environ.*, 2013, **141**, 363–377.
- 183 L. Ma, M. Melander, T. Weckman, K. Laasonen and J. Akola, *J. Phys. Chem. C*, 2016, **120**, 26747–26758.
- 184 K. Koizumi, K. Nobusada and M. Boero, *J. Phys. Chem. C*, 2015, **119**, 15421–15427.
- 185 L. Zhang, H. Y. Kim and G. Henkelman, *J. Phys. Chem. Lett.*, 2013, **4**, 2943–2947.
- 186 T. V. W. Janssens, B. S. Clausen, B. Hvolbaek, H. Falsig, C. H. Christensen, T. Bligaard and J. K. Nørskov, *Top. Catal.*, 2007, **44**, 15–26.
- 187 Z. J. Zuo, L. Wang, P. De Han and W. Huang, *Int. J. Hydrogen Energy*, 2014, **39**, 1664–1679.
- 188 Q. Liu, Y. Ning, W. Huang, Q. Fu, F. Yang and X. Bao, *J. Phys. Chem. C*, 2018,

- 122**, 8364–8372.
- 189 S. V. Dorozhkin and M. Epple, *Angew. Chemie - Int. Ed.*, 2002, **41**, 3130–3146.
- 190 M. Epple, *Acta Biomater.*, 2018, **77**, 1–14.
- 191 R. Lin and Y. Ding, *Materials (Basel)*, 2013, **6**, 217–243.
- 192 A. Clearfield and D. S. Thakur, *Appl. Catal.*, 1986, **26**, 1–26.
- 193 D. C. Rambaldi, A. Zattoni, S. Casolari, P. Reschiglian, D. Roessner and C. Johann, in *Clinical Chemistry*, 2007, **53**, 2026–2029.
- 194 T. T. N. Nguyen, V. Ruaux, L. Massin, C. Lorentz, P. Afanasiev, F. Maugé, V. Bellière-Baca, P. Rey and J. M. M. Millet, *Appl. Catal. B Environ.*, 2015, **166–167**, 432–444.
- 195 K. Ramesh, J. Zheng, E. G. Y. Ling, Y. F. Han and A. Borgna, *J. Phys. Chem. C*, 2009, **113**, 16530–16537.
- 196 Z. Guo, D. S. Theng, K. Y. Tang, L. Zhang, L. Huang, A. Borgna and C. Wang, *Phys. Chem. Chem. Phys.*, 2016, **18**, 23746–23754.
- 197 B. Pan, S. Luo, W. Su and X. Wang, *Appl. Catal. B, Environ.*, 2015, **168–169**, 458–464.
- 198 M. Anbia, M. K. Rofouei and S. W. Husain, *Chinese J. Chem.*, 2006, **24**, 1026–1030.
- 199 D. Morgan, A. Van der Ven and G. Ceder, *Electrochem. Solid-State Lett.*, 2004, **7**, A30.
- 200 K. Zaghbi, A. Mauger, J. B. Goodenough, F. Gendron and C. M. Julien, *Chem. Mater.*, 2007, **19**, 3740–3747.
- 201 Y. Choi, D. S. Park, H. J. Yun, J. Baek, D. Yun and J. Yi, *ChemSusChem*, 2012, **5**, 2460–2468.
- 202 C. K. Jyothi, K. B. Jaimy, S. Ghosh, S. Sankar, V. S. Smitha and K. G. K. Warriar, *J. Solid State Chem.*, 2011, **184**, 1867–1874.
- 203 Y. Li and C. Zhao, *Chem. Mater.*, 2016, **28**, 5659–5666.
- 204 A. Dutta, A. K. Patra, S. Dutta, B. Saha and A. Bhaumik, *J. Mater. Chem.*, 2012,

- 22, 14094–14100.
- 205 G. C. Behera and K. M. Parida, *Catal. Sci. Technol.*, 2013, **3**, 3278–3285.
- 206 F. S. Asghari and H. Yoshida, *Carbohydr. Res.*, 2006, **341**, 2379–2387.
- 207 S. Xu, D. Pan, W. Li, P. Shen, Y. Wu, X. Song, Y. Zhu, N. Xu, L. Gao and G. Xiao, *Fuel Process. Technol.*, 2018, **181**, 199–206.
- 208 P. Carniti, A. Gervasini, S. Biella and A. Auroux, *Catal. Today*, 2006, **118**, 373–378.
- 209 V. V. Ordonsky, V. L. Sushkevich, J. C. Schouten, J. Van Der Schaaf and T. A. Nijhuis, *J. Catal.*, 2013, **300**, 37–46.
- 210 I. Jiménez-Morales, A. Teckchandani-Ortiz, J. Santamaría-González, P. Maireles-Torres and A. Jiménez-López, *Appl. Catal. B Environ.*, 2014, **144**, 22–28.
- 211 F. Wang, J. L. Dubois and W. Ueda, *J. Catal.*, 2009, **268**, 260–267.
- 212 H. Gan, X. Zhao, B. Song, L. Guo, R. Zhang, C. Chen, J. Chen, W. Zhu and Z. Hou, *Chinese J. Catal.*, 2014, **35**, 1148–1156.
- 213 D. Stošić, S. Bennici, S. Sirotin, C. Calais, J. L. Couturier, J. L. Dubois, A. Travert and A. Auroux, *Appl. Catal. A Gen.*, 2012, **447–448**, 124–134.
- 214 M. Takeda, M. Ikeda, S. Satoh, H. Dansako, T. Wakita and N. Kato, *Acta Med. Okayama*, 2016, **70**, 111–118.
- 215 M. Gu, D. Yu, H. Zhang, P. Sun and H. Huang, *Catal. Letters*, 2009, **133**, 214–220.
- 216 O. A. Rusu, W. F. Hoelderich, H. Wyart and M. Ibert, *Appl. Catal. B Environ.*, 2015, **176–177**, 139–149.
- 217 G. W. Coulston, S. R. Bare, H. Kung, K. Birkeland, G. K. Bethke, R. Harlow, N. Herron and P. L. Lee, *Science*, 1997, **275**, 191–193.
- 218 F. Wang, Z. Yuan, B. Liu, S. Chen and Z. Zhang, *J. Ind. Eng. Chem.*, 2016, **38**, 181–185.
- 219 N. Guillou, Q. Gao, P. M. Forster, S. Park, J. Chang, M. Nogue and A. K. Cheetham, *Angew. Chemie - Int. Ed.*, 2001, **40**, 2831–2834.

- 220 Y. Takita, M. Ninomiya, H. Miyake, H. Wakamatsu, Y. Yoshinaga and T. Ishihara, *Phys. Chem. Chem. Phys.*, 1999, 4501–4504.
- 221 Q. Lu, Z. Zhang, X. Wang, H. Guo, M. Cui and Y. Yang, *Front. Chem.*, 2018, **6**, 1–10.
- 222 A. Aboulayt, T. Onfroy, A. Travert, G. Clet and F. Maugé, *Appl. Catal. A Gen.*, 2017, **530**, 193–202.
- 223 K. Tanabe, M. Misono, Y. Ono and H. Hattori, *New solid acids and bases, Studies in Surface Science and Catalysis, Vol 51*, Elsevier Science, 1989.
- 224 S. Diallo-Garcia, M. Ben Osman, J. M. Krafft, S. Boujday and C. Guylène, *Catal. Today*, 2014, **226**, 81–88.
- 225 W. A. Deer, R. A. Howie and J. Zussman, *An Introduction to the Rock-Forming Minerals*, Harlow, Essex, England: New York, NY: Longman Scientific & Technical, 2nd ed., 2013.
- 226 R. Astala and M. J. Stott, *Phys. Rev. B - Condens. Matter Mater. Phys.*, 2008, **78**, 1–11.
- 227 R. Yu and L. C. De Jonghe, *J. Phys. Chem. C*, 2007, **111**, 11003–11007.
- 228 X. Wang, L. Zhang, Z. Zhang and X. Wang, *Appl. Phys. A Mater. Sci. Process.*, 2016, **122**, 1–7.
- 229 L. Zhang, X. Wang, Z. Zhang and X. Wang, *Comput. Mater. Sci.*, 2017, **127**, 22–28.
- 230 J. Ruiz-Fuertes, A. Hirsch, A. Friedrich, B. Winkler, L. Bayarjargal, W. Morgenroth, L. Peters, G. Roth and V. Milman, *Phys. Rev. B*, 2016, **94**, 1–6.
- 231 M. R. Neupane, G. A. Garrett, S. Rudin and J. W. Andzelm, *J. Phys. Condens. Matter*, 2016, **28**, 205501
- 232 A. Hirsch, I. Azuri, L. Addadi, S. Weiner, K. Yang, S. Curtarolo and L. Kronik, *Chem. Mater.*, 2014, **26**, 2934–2942.
- 233 N. A. Curry and D. W. Jones, *J. Chem. Soc. A Inorganic, Phys. Theor. Chem.*, 1971, 3725–3729.

- 234 K. Matsunaga, *J. Am. Ceram. Soc.*, 2010, **93**, 1–14.
- 235 A. S. Posner, J. M. Stuymans and E. R. Lippincott, *Nature*, 1960, **4749**, 486–487.
- 236 P. T. Nguyen, A. W. Sleight, N. Roberts and W. W. Warren, *J. Solid State Chem.*, 1996, **122**, 259–265.
- 237 A. Haras, M. Witko, D. R. Salahub and H. A. Duarte, *Surf. Sci.*, 2003, **538**, 160–170.
- 238 Y. Yi, X. Zhao, Y. Teng, B. Bi, L. Wang, L. Wu and K. Zhang, *J. Nucl. Mater.*, 2016, **482**, 170–174.
- 239 C. S. Ewing, S. Bhavsar, G. Veser, J. J. McCarthy and J. K. Johnson, *Langmuir*, 2014, **30**, 5133–5141.
- 240 D. Mora-Fonz and A. L. Shluger, *Phys. Rev. B*, 2019, **99**, 014202.
- 241 D. Di Tommaso, R. I. Ainsworth, E. Tang and N. H. De Leeuw, *J. Mater. Chem. B*, 2013, **1**, 5054–5066.
- 242 P. Mäki-Arvela, I. L. Simakova, T. Salmi and D. Y. Murzin, *Chem. Rev.*, 2014, **114**, 1909–1971.
- 243 M. Schlaf and Z. C. Zhang, *chapter3*, springer, 2016.
- 244 D. Sun, Y. Yamada, S. Sato and W. Ueda, *Green Chem.*, 2017, **19**, 3186–3213.
- 245 A. Chierogato, M. D. Soriano, F. Basile, G. Liosi, S. Zamora, P. Concepción, F. Cavani and J. M. López Nieto, *Appl. Catal. B Environ.*, 2014, **150–151**, 37–46.
- 246 A. Chierogato, M. D. Soriano, E. García González, G. Puglia, F. Basile, P. Concepción, C. Bandinelli, J. M. López Nieto and F. Cavani, *ChemSusChem*, 2015, **8**, 398–406.
- 247 Y. Fan, C. Zhou and X. Zhu, *Catal. Rev. - Sci. Eng.*, 2009, **51**, 293–324.
- 248 M. A. Abdel-Rahman, Y. Tashiro and K. Sonomoto, *J. Biotechnol.*, 2010, **156**, 286–301.
- 249 M. A. Abdel-Rahman, Y. Tashiro and K. Sonomoto, *Biotechnol. Adv.*, 2013, **31**, 877–902.
- 250 F. Auneau, L. S. Arani, M. Besson, L. Djakovitch, C. Michel, F. Delbecq, P. Sautet

- and C. Pinel, *Top. Catal.*, 2012, **55**, 474–479.
- 251 <https://www.businesswire.com/news/home/20170621005594/en/Global-Lactic-Acid-Market-2017-2025---Growth>.
- 252 G. Ulian, G. Valdrè, M. Corno and P. Ugliengo, *Am. Mineral.*, 2013, **98**, 410–416.
- 253 T. J. Lin and C. C. Chiu, *Phys. Chem. Chem. Phys.*, 2017, **20**, 345–356.
- 254 I. E. Boldeskul, L. F. Sukhodub, A. N. Kalinkevich and V. D. Khavryutchenko, *Condens. Matter Phys.*, 2006, **9**, 669–679.
- 255 E. Blanco, P. Delichere, J. M. M. Millet and S. Loricant, *Catal. Today*, 2014, **226**, 185–191.
- 256 E. Blanco, C. Lorentz, P. Delichere, L. Burel, M. Vrinat, J. M. M. Millet and S. Loricant, *Appl. Catal. B Environ.*, 2016, **180**, 596–606.
- 257 P. F. Schofield, K. S. Knight, J. A. M. van der Houwen and E. Valsami-Jones, *Phys. Chem. Miner.*, 2004, **31**, 606–624.
- 258 S. Baroni, P. Giannozzi and A. Testa, *Phys. Rev. Lett.*, 1987, **58**, 1861–1864.
- 259 P. A. Redhead, *Vacuum*, 1962, **12**, 203–211.
- 260 K. Lertjiamratn, P. Praserttham, M. Arai and J. Panpranot, *Appl. Catal. A Gen.*, 2010, **378**, 119–123.
- 261 D. Song, *Ind. Eng. Chem. Res.*, 2017, **56**, 11013–11020.
- 262 D. Song, *Ind. Eng. Chem. Res.*, 2017, **56**, 11013–11020.
- 263 I. Bucsi, A. Molnar, M. Bartok and G. a. Olah, 1994, **50**, 8195–8202.
- 264 J. Lee, J. B. Grutzner, W. E. Walters and W. Nicholas Delgass, *Studies in Surface Science and Catalysis*, Elsevier, 2007, 2603–2608.
- 265 W. Zhang, D. Yu, X. Ji and H. Huang, *Green Chem.*, 2012, **14**, 3441–3450.
- 266 M. E. Winfield, *J. C. S. I. R.*, 1945, **18**, 412.
- 267 H. Duan, D. Sun, Y. Yamada and S. Sato, *Catal. Commun.*, 2014, **48**, 1–4.
- 268 W. Kim, W. Shin, K. J. Lee, Y. S. Cho, H. S. Kim and I. N. Filimonov, *Appl. Catal. A Gen.*, 2019, **570**, 148–163.
- 269 M. A. Nikitina and I. I. Ivanova, *ChemCatChem*, 2016, **8**, 1346–1353.

- 270 A. Romano and E. S. Şuhubi, *Int. J. Eng. Sci.*, 1989, **27**, 1135–1142.
- 271 T. T. N. Nguyen, V. Ruaux, F. Maugé, V. Bellière-Baca, P. Rey and J. M. M. Millet, *Appl. Catal. A Gen.*, 2015, **504**, 4–10.
- 272 W. Daniell, U. Schubert, R. Glöckler, A. Meyer, K. Noweck and H. Knözinger, 2000, **196**, 247–260.
- 273 S. Diallo-Garcia, M. Ben Osman, J. M. Krafft, S. Casale, C. Thomas, J. Kubo and G. Costentin, *J. Phys. Chem. C*, 2014, **118**, 12744–12757.
- 274 A. V. Ivanov, A. E. Koklin, E. B. Uvarova and L. M. Kustov, *Phys. Chem. Chem. Phys.*, 2003, **5**, 4718.
- 275 T. Mallat and A. Baiker, *Chem. Rev.*, 2004, **104**, 3037–3058.
- 276 W. Li, Y. Ando, E. Minamitani and S. Watanabe, *J. Chem. Phys.*, 2017, **147**, 214106.